SPECTRAL MULTIPLEXING INFORMATION PROCESSING FOR QUANTUM NETWORKS

by

Navin Bhartoor Lingaraju

A Dissertation

Submitted to the Faculty of Purdue University

In Partial Fulfillment of the Requirements for the degree of

Doctor of Philosophy

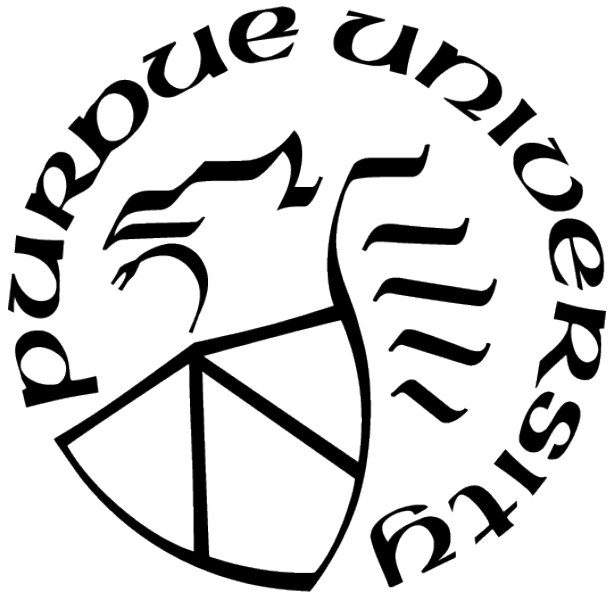

School of Electrical and Computer Engineering

West Lafayette, Indiana

May 2021

THE PURDUE UNIVERSITY GRADUATE SCHOOL
STATEMENT OF COMMITTEE APPROVAL

Dr. Andrew M. Weiner, Chair

School of Electrical and Computer Engineering

Dr. Sunil Bhave

School of Electrical and Computer Engineering

Dr. Zubin Jacob

School of Electrical and Computer Engineering

Dr. Minghao Qi

School of Electrical and Computer Engineering

Approved by:

Dr. Dimitrios Peroulis

For Laura, My Wife

Love is the voice under all silences,
the hope which has no opposite in fear;
the strength so strong mere force is feebleness:
the truth more first than sun, more last than star.
- E.E. Cummings

ACKNOWLEDGMENTS

When I began this journey, initially at the University of Maryland, I never could have imagined the path I would take to get here. It has been both unbelievably challenging and immensely rewarding. First and foremost, I would like to thank my advisor, Andrew Weiner, for his ever insightful feedback on technical matters, as well as providing opportunities for professional growth and development. When I joined his group, the Ultrafast Optics and Optical Communications Laboratory, I had a general sense for what my graduate work might involve but could not have imagined that it would span the gamut from fundamental science, to device development, to network-level demonstrations. It is a testament to his ability to identify new lines of research and shepherd their development that I had such a wide range of experiences. This has been instrumental not only to my growth as a scientist, but also to my ability to translate new ideas into successful proposals and demonstrations. It never ceases to amaze me when he finds the odd inconsistency in my work or reasoning that would have escaped most other observers. This attention to technical and narrative detail made me not only a better scientist, but a better writer and a better speaker. Above all, I am especially grateful for the supportive and collaborative research environment he has fostered. It has been a joy to share my graduate experience with talented colleagues who genuinely enjoy each other's company.

I am fortunate to have had two other mentors during my time at Purdue. Daniel Leaird, our group's senior scientist and lab manager, in addition to offering valuable technical guidance, is a veritable encyclopedia of practical advice that has been critical to making swift research progress. I am grateful for his always being generous with his time. Joseph Lukens is perhaps most responsible for the development of photonic quantum information in the spectral domain, the primary focus of my graduate research. His willingness to entertain even the most basic questions, serve as a sounding board on a range of adjacent and high-level topics, and help me flesh out my own ideas has been invaluable to my professional development.

I would also like to thank my colleagues for their help on this journey. Oscar Sandoval, my first partner on any project at Purdue, was always willing to lend a hand or answer

a question. Keith McKinzie was a great resource during my initial foray into photonic integrated circuits (PICs). He was always ready with an important reference or a practical perspective. I will fondly remember brainstorming new ideas with Hsuan-Hao (Peach) Lu and Poolad Imany, the two colleagues I worked most closely with toward the latter part of my time at Purdue. Their willingness to engage seemingly outlandish ideas and work through the finer details on concepts that survived contact with reality was crucial to my expanding my technical imagination and follow through. I am also grateful to Luke Cohen, my partner in simulation and tapeout, for helping us make great progress in PIC design. There are many other colleagues whose advice and time I am grateful for – Mohammed Al alshyakh, Ogaga Odele, Jose Jaramillo-Villegas, Nathan O'Malley, Suparna Seshadri, Alex Moore, and Cong Wang. Perhaps my only regret from graduate school is that the pandemic limited my working with the newer members of our group.

One of the bigger surprises in my graduate career was the extent to which I was able to engage with collaborators. I am grateful for the chance to work with Misha Brodsky, Daniel Jones, Steven Estrella, and Daniel Renner. The collaboration that perhaps had a transformative impact on my career was the one with Rochester Institute of Technology and Air Force Research Laboratory (Rome, NY). I cannot thank Matthew van Niekerk enough for working with us over the last year. His help and hard work was instrumental to revamping our approach to photonic integrated design and layout and we simply do not make the progress we did without him. I am also immensely grateful to Stefan Preble and Michael Fanto for giving us the opportunity to move our concepts onto chip-scale platforms and for retaining faith in me after a design error short-circuited our ambitions on an initial fabrication run. Failure was an incredible motivator, and I am excited to see the impact our latest work will have.

On the personal front, I want to thank my parents, Chitra and Raju, for nurturing my curiosity from a young age and supporting my aspirations to this day. Accomplishing what I have would not have been possible without my brother Kiran, who made the time to visit my parents when needed. I also appreciate his and my parents' understanding of my long absences from home and I hope that more frequent visits will be possible in the near future.

I also want to thank my parents-in-law, Susan and Alan Maul, for their unbelievable support over the last four years. I do not know how my wife and I could have weathered a challenging childbirth, a car accident, and a global pandemic without their time and support. It has also been an incredible joy to watch our son, West, grow up in close contact with his grandparents, who he adores beyond words. Our house reverberates with shouts of "Grandma and Grandpa are here!" every time they drive up for a visit.

I owe the greatest debt of gratitude to my wife, Laura. She is the rock that has kept me anchored through this long and winding journey. For better or worse, I have been a graduate student in some form for nearly all of our married life. While it has been hard for me, I know it has been harder for her. From putting up with my two jobs and multi-state commutes in the DC area, to nursing me back from Achilles tendon reconstruction, to managing our household and assuming most of the responsibility raising our wonderful son West, she has been there and kept our family on track. I cannot thank her enough and pray I have similar strength to support her career and aspirations. I look forward to our next steps as a family and I am excited to be a bigger part in her and our son's life as our new journey begins.

Navin B. Lingaraju

West Lafayette, Indiana
April 2021

TABLE OF CONTENTS

LIST OF FIGURES

LIST OF SYMBOLS

τ	relative time, or delay between events
Ω	angular frequency
ω	angular frequency
δ	modulation depth
J_n	n^{th} order Bessel function
H	horizontal axis
V	vertical axis
D	diagonal axis
A	antidiagonal axis
BW_{RF}	radiofrequency bandwidth
$\mathcal{F}$	transformation fidelity
$\mathcal{P}$	success probability of operation or gate
V	voltage in volts
V_π	half-wave voltage
α	attenuation
Δf_{input}	bandwidth of optical input
Δf_{filter}	bandwidth of spectral filter
σ	conductivity

ABBREVIATIONS

QKD	quantum key distribution
DoF	degree of freedom
dB	decibels
km	kilometers
OAM	orbital angular momentum
OEO	optical-electrical-optical
ORNL	Oak Ridge National Laboratory
EOM	electro-optic phase modulator
QFP	quantum frequency processor
BFC	biphoton frequency comb
CMOS	complementary metal-oxide-semiconductor
SPDC	spontaneous parametric down conversion
PPLN	periodically-poled lithium niobate
FSR	free spectral range
TIA	time interval analyzer
RF	radio frequency
CW	continuous-wave
HOM	Hong–Ou–Mandel
SNSPD	superconducting nanowire single-photon detector
FWHM	full width at half-maximum
JSI	joint spectral intensity
MUB	mutually unbiased basis
DFT	discrete Fourier transform
PDPM	polarization diversity phase modulator
PBS	polarizing beam splitter
PZT	piezoelectric transducer
PM	polarization-maintaining
PIC	photonic integrated circuit

SOH	silicon-organic hybrid
POH	plasmonic-organic hybrid
OEO	organic electro-optic
EO	electro-optic
BOX	buried oxide
AIM	American Institute of Manufacturing
A*STAR	Agency for Science, Technology and Research
BSA	Bell state analyzer
DWDM	dense wavelength-division multiplexing
CAR	coincidence-to-accidental ratio
WSS	wavelength-selective switch
FPC	fiber-based polarization controller
HWP	half-wave plate
QWP	quarter-wave plate
TIA	time interval analyzer
APD	avalanche photodiode

ABSTRACT

Modern fiber-optic networks leverage massive parallelization of communications channels in the spectral domain, as well as low-noise recovery of optical signals, to achieve high rates of information transfer. However, quantum information imposes additional constraints on optical transport networks – the no-cloning theorem forbids use of signal regeneration and many network protocols are premised on operations like Bell state measurements that prize spectral indistinguishability. Consequently, a key challenge for quantum networks is identifying a path to high-rate and high-fidelity quantum state transport.

To bridge this gap between the capabilities of classical and quantum networks, we developed techniques that harness spectral multiplexing of quantum channels, as well as that support frequency encoding. In relation to the former, we demonstrated reconfigurable connectivity over arbitrary subgraphs in a multi-user quantum network. In particular, through flexible provisioning of the pair source bandwidth, we adjusted the rate at which entanglement was distributed over any user-to-user link. To facilitate networking protocols compatible with both spectral multiplexing and frequency encoding, we synthesized a Bell state analyzer based on mixing outcomes that populate different spectral modes, in contrast to conventional approaches that are based on mixing outcomes that populate different spatial paths. This advance breaks the tradeoff between the fidelity of remote entanglement and the spectral distinguishability of photons participating in a joint measurement.

Finally, we take steps toward field deployment by developing photonic integrated circuits to migrate the aforementioned functionality to a chip-scale platform while also achieving the low loss transmission and high-fidelity operation needed for practical quantum networks.

1. INTRODUCTION

Recent advances in quantum computing have, deservedly, captured the imagination of the scientific community and the broader public [1], [2]. However, quantum technologies have the potential to not only unleash a revolution in how we process information, but also enable communications security [3] and measurement precision [4] beyond what is capable with classical counterparts. Unlocking the full promise of these technologies requires mediating both communication and entanglement between distant parties. In the case of communication and sensing, the need for networking is readily apparent as physical separation between parties, or quantum states, is fundamental to the application at hand. The value of cryptographic protocols like quantum key distribution (**QKD**) derives from the fact that users separated by great distances share correlated outcomes for measurements with individually random results, which is exploited to generate secure cryptographic keys [3]. Similarly, consider the case of clock synchronization. Classical methods of synchronizing spatially separated clocks require transmission of light (or matter) between these clocks and are, therefore, sensitive to disturbances in the intervening medium. Quantum clock synchronization bypasses this by relying on prior shared entanglement between two locations [5], [6].

The need for networking is perhaps not readily apparent in the case of quantum computing. However, as matter-based qubit systems increase in size, counteracting decoherence becomes challenging, thereby placing limits on how large standalone systems can be. For example, superconducting qubit-based systems operate at millikelvin temperatures and require sophisticated dilution refrigerators to maintain operating conditions. Scaling these systems up from tens of qubits to thousands or millions of qubits will place commensurate demands on the cooling power of a single dilution refrigerator [7], [8]. In addition, one needs to consider challenges associated with delivering thousands to millions of control signals in a constrained environment. In ion trap-based systems, the challenge is more fundamental as noise increases with the number of ions in a single chain [9]. For these reasons, researchers view modular architectures, connected by a quantum network, as the most promising path to large-scale quantum computing [10]. The situation is not unlike cloud and high-performance

computing where the linking of distributed computing resources has led to breathtaking advances in fields like data science and artificial intelligence.

1.1 Photonic Quantum Networks

While quantum states are extremely fragile, photons experience virtually no decoherence and are the only realistic choice to carry quantum information over long distances. In quantum optical communication, information is encoded in one or more attributes, or degrees of freedom (**DoFs**), of photons. This includes polarization state, time bin, spatial mode, orbital angular momentum, and frequency bin, among others. Most early (and foundational) experiments in quantum networking relied on encoding and entanglement in polarization state [11] as it is one of the most straightforward DoFs to work with in academic research settings. For example, one can implement arbitrary qubit rotations with a combination of quarter-wave and half-wave plates, which are inexpensive and introduce minimal optical loss. Demonstrations span the networking gamut, from quantum key distribution [12] and quantum dense coding [13], to state teleportation [14] and entanglement swapping [15].

In just the last few years there has been tremendous progress in facilitating entanglement and communication between end nodes using satellite-based and terrestrial free space links [16], [17]. Photon loss from free space propagation scales quadratically, which over long distances represents a dramatic improvement over the exponential scaling of loss in optical fiber. Without a doubt, global-scale quantum networks will rely, at least in part, on some form of free space communication. However, for dense and short-reach communication, like local area and metropolitan area networks, free space optical channels are an unrealistic choice given the need for line-of-sight links. This, coupled with very low loss in standard optical fiber (0.2 dB/km), make optical fiber-based communication an important modality for links shorter than 100 km.

Unfortunately, not all photonic DoFs are compatible with standard (single mode) optical fiber. Orbital angular momentum- (**OAM**) and path-based encoding are not supported, while polarization state- and spatial mode-based encodings are not stable over standard fiber [18]. This leaves the time-energy (time-frequency) DoF as possibly the best candidate

for quantum optical communication over fiber. While classical information is encoded in the amplitude and/or phase of an optical signal [19], frequency plays a critical role in classical networking – it is used to delineate communications channels, making it possible to utilize the tremendous bandwidth of optical filter to transmit multiple channels in parallel and support terabit data rates over a single optical fiber [20]. In addition, frequency is naturally stable over fiber and permits straightforward measurement with high-efficiency filters and detectors.

These advantages – parallelization of communications channels and stability over optical fiber – can potentially be leveraged to support the needs of quantum networks. Furthermore, unlike polarization, frequency supports multilevel quantum information, i.e., d-level systems with $d > 2$ [21], opening the door to quantum information encoded in higher dimensions. This is in some ways analogous to multilevel encoding formats like pulse amplitude modulation and quadrature amplitude modulation in classical communication.

1.2 Classical vs. Quantum Networks

Modern fiber-optic networks overcome the exponential scaling of loss in optical fiber through use of regenerative amplifiers and optical-electrical-optical (**OEO**) conversion [19]. Unsurprisingly, commercial telecommunications equipment is engineered (perhaps even over-engineered) for long-term reliability to the detriment of considerations like optical loss.

Quantum state transport imposes additional constraints on fiber-optic networks. Most notably, the no-cloning theorem forbids the creation of a copy of an arbitrary quantum state without introducing unacceptable errors [22]. Consequently, amplification and OEO conversion cannot be used to extend the reach of quantum links or to manage spectral bandwidth at the network edge. These limitations can, in principle, be overcome with quantum repeaters [23].

The basic concept behind a quantum repeater is that one can partition an arbitrarily long link into a series of smaller links. Entanglement, or quantum information, can be swapped over each smaller link with the caveat that swapping operations are only performed *after* it is determined that photons have successfully traversed the full extent each and every

smaller link. This necessities the development of efficient quantum memories [24] that can store photons at each intermediate node on the network. The communications rate and, therefore, the requirements on memory time can be further improved through multiplexing in the spatial [25], temporal [24], and spectral [26] domain.

1.3 Quantum Information in the Frequency Domain

As communications experiments move from benchtop arrangements to field demonstrations over deployed fiber, it becomes apparent that protocols based on encoding and entanglement in polarization state are limited by channel impairments like polarization mode dispersion and polarization dependent loss [27]. This has motivated a shift to other degrees of freedom, like time bin, which has achieved greater stability than is otherwise possible with polarization-based protocols [18]. In addition, OAM- and spatial mode-based encodings have been harnessed for long distance communication over free space [28].

The tremendous success of wavelength-division multiplexing in modern telecommunications leads to the expectation that commensurate gains can be achieved in at least some aspects of quantum communication and networking. Furthermore, energy, i.e., frequency, is commonly used as the encoding variable for superconducting qubit [7] and ion trap [29] quantum systems. However, frequency has traditionally been a challenging degree of freedom to manipulate as frequency mixing operations require either high-speed electro-optic modulators [30] or strong pump fields [31], neither which compares with wave retarders (used to manipulate polarization state) in terms of cost or ease of use.

1.4 Spectral Transformations and the Quantum Frequency Processor

Motivated by the potential of frequency to boost the performance quantum networks, a team at Oak Ridge National Laboratory (**ORNL**) developed an entirely new approach to quantum information processing based on frequency bins in 2017 [32]. By cascading electro-optic phase modulators (**EOMs**) and Fourier-transform pulse shapers [33], [34], a concatenation referred to as a quantum frequency processor (**QFP**), any frequency bin quantum

operation can be realized in a theoretically scalable fashion. This was confirmed by subsequent demonstration of a universal gate set with the QFP [30], [35], [36].

	photonic DoF	Path	OAM	Time-bin	Frequency-bin
Generation	Method	*D* nonlinear structures	1 nonlinear structure	Pulsed pump, 1 nonlinear structure	1 nonlinear structure
	Max. # of modes	16 **[37]**	100 **[40]**	32 **[43]**	~ 1000 (PPLN) **[47]** ~ 40 (MRR) **[48]**
	Max. Entanglement	14 (certified) **[37]**	100 (certified) **[40]**	5 (certified) **[44]** 4 (full QST) **[45]**	4 (full QST) **[49]**
Manipulation	Basic Units	Beam splitters, phase shifters	SLM, phase-plates	Unbalanced interferometers, active switching	EOM, pulse shaper **[32]**
	Scalability	$\mathcal{O}(D^2)$ **[38]**	$\mathcal{O}(1)$ - $\mathcal{O}(D)$ **[41]***	$\mathcal{O}(D^2)$	$\mathcal{O}$ (D) units, or $\mathcal{O}(1)$ units with $\mathcal{O}(D)$ RF tones **[32,50]**
	Max. dimension	4 (Arbitrary) **[38]**	5 (DFT, cyclic) **[41]**	3 (cyclic) **[43]**	3 (DFT) **[30]**
Fiber Transmission	Network compatibility	Multicore fiber	Few-mode fiber	SMF	SMF
	Longest distance	30 cm **[39]**	1 km **[42]**	> 100 km **[46]**	> 40 km **[49]**
	Source of errors	Phase stability between cores	Intermodal crosstalk	X	X

Figure 1.1. A comparison of quantum information in different photonic degrees freedom – spatial path (Refs. [37]–[39]), OAM (Refs. [40]–[42]), time bin (Refs. [43]–[46]), and frequency bin (Refs. [32], [35], [47]–[50]).

(*) - Specific set of gates in small dimensions ($D < 5$)
Classical and weak-coherent examples are excluded from this figure.

The QFP paradigm for discrete variable frequency encoding offers three compelling advantages. The first is that it admits massive parallelization of quantum operations in a single spatial mode. Secondly, this architecture relies on high-speed EOMs and, therefore, has the potential to permit fast reconfiguration of quantum gates. Lastly, it supports high-dimensional ($d > 2$) quantum operations [30]. This opens the door to high-dimensional encodings that are compatible with multiplexing in the spectral domain, stable over standard fiber, and able to leverage deployed fiber-optic infrastructure. A comparison of different

photonic degrees of freedom in terms of generation, manipulation, and fiber transmission is presented in **Fig. 1.1**

1.5 Outline

Our achievements at Purdue University complement the above body of work by developing tools and techniques to support networking protocols based on frequency-multiplexed or frequency-encoded quantum information. The rest of this dissertation is organized along three tracks — (i) entanglement characterization, (ii) component and subsystem development, and (iii) entanglement distribution and generation.

In chapter 2, we examine whether Hong–Ou–Mandel interference, a ubiquitous tool in quantum optics, can be used as a probe of high-dimensional frequency-bin entanglement. Later in the chapter we explore the phenomenon of quantum walks by observing how frequency modes "walk" under the influence of electro-optic phase modulation. A key outcome of this work is the recognition that a distribution in the relative arrival of photons in an entangled pair is mapped to a distribution in two-photon energies after the quantum walk, thus offering a possible route to probing fine features in the temporal correlation of frequency-entangled photons. We conclude this chapter by certifying three-dimensional frequency-bin entanglement based on measurements in the computational and Fourier bases.

On the device front (chapter 3), we explore two routes to expanding the tools available to manipulate frequency-encoded quantum information. The first is implementation of a polarization diversity scheme to perform polarization-insensitive (electro-optic) phase modulation. This allows us to implement frequency-mixing operations that also preserve entanglement in polarization state. On a parallel track, we leverage recent developments in integrated photonics and materials science to model and design an integrated quantum frequency processor that not only improves on the performance of discrete components with respect to optical loss, but also with respect to the complexity, i.e., dimensionality, of quantum gates one can implement.

Finally, in chapter 4, we build on previous work in entanglement distribution by using a wavelength-selective switch to manage the rate at which entanglement is shared across

a multi-user network. In addition, we demonstrate the ability to enable not just a fully and simultaneously connected network, but also any arbitrary subgraph and do so while equalizing the coincidence rate across all two-party links. To support functionality at the next protocol level, we synthesize a Bell state analyzer that is based on mixing modes that populate different frequencies rather than mixing modes that populate different spatial paths. Such frequency mixing-based Bell state analyzers have the potential to support heterogeneous nodes and dense spectral multiplexing on quantum networks without imposing additional limits on entanglement fidelity or the entanglement generation rate.

This is followed by brief comments in chapter 5 on the outlook for frequency-multiplexed and frequency-encoded quantum information in the realm of quantum communication and networking.

2. ENTANGLEMENT CHARACTERIZATION

Two-photon quantum frequency combs, or biphoton frequency combs (**BFCs**) for short, are characterized by entanglement over discrete, energy-matched ($\omega_{\text{signal}} + \omega_{\text{idler}} = \omega_{\text{pump}}$) pairs of frequency modes or bins [48], [49], [51], [52]. The frequencies of the two photons are correlated such that the biphoton must be described by a coherent superposition of two-photon basis states that cannot be factored as a product of individual photon wavefunctions. If these two photons are distinguished on the basis of frequency, the high and low frequency photons are referred to as "signal" and "idler" (nomenclature is a historical artifact), respectively. Such a state can be described by the general expression:

$$|\Psi\rangle_{\text{BFC}} = \sum_{p=1}^{N} \alpha_p \, |p, -p\rangle_{SI} \tag{2.1}$$

Here S and I denote the signal and idler photon, respectively, and α_p represents the complex amplitude of the p^{th} pair of frequency bins, where bins with indices $\pm p$ are frequency-entangled. This form of entanglement is often referred to as frequency-bin entanglement [53]

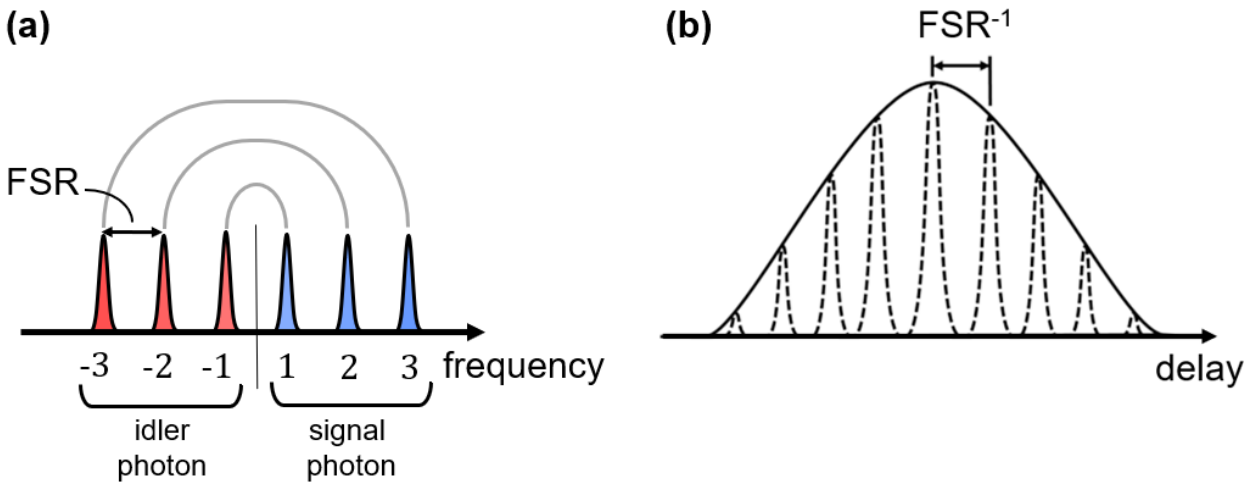

Figure 2.1. (a) Illustration of a biphoton frequency comb where the signal photon and the idler photon are each in a superposition of three discrete frequency modes or bins. The free spectral range (FSR) of the comb is the separation between frequency bins in each photon. (b) Correlations in the relative arrival between the signal and idler, which is often referred to as the joint temporal correlation or the time correlation function.

and an example of such a two-photon state is shown in **Fig. 2.1(a)**. In analogy to classical frequency combs [54], the joint spectrum of these states features discrete modes, or bins, equidistant from one another in the spectral domain. The comb-like nature of the biphoton spectrum is well-suited to quantum information processing [32] and recent work with this platform includes the realization of high-fidelity discrete Fourier transform gates [30], parallel qubit rotations using a quantum frequency processor (**QFP**) [35], a coincidence-basis controlled–NOT gate [36], and single-photon two-qudit gates [43], [55]. This progress hints at the potential for BFCs to play are role in the development of practical quantum networking protocols. An important step to advancing this platform is the development of robust methods to certify frequency-bin entanglement.

Although such states have been generated directly in CMOS-compatible optical microresonators [48], [49], in the demonstrations described here states are prepared by carving a continuous spontaneous parametric down-conversion spectrum (**SPDC**) [52]. An advantage to this approach, aside from simplified state preparation, is that the choice of BFC parameters, such as the linewidth of individual frequency bins and the free spectral range (**FSR**) of the state, is mostly flexible subject to some equipment constraints. BFCs are characterized not only by spectral correlations between photons in a pair, but also by correlations in their arrival (at a detector, for example) relative to one another [56]. An example of such temporal correlations is shown in **Fig. 2.1(b)**. Here the x–axis represents the delay between the arrival time of one photon with respect to its entangled counterpart. If $|\,|\Psi(\tau)\rangle\,|^2$ describes this joint temporal correlation, it is related to the joint spectral amplitude ($|\Psi(\Omega)\rangle$) through a Fourier transform.

$$|\Psi(\tau)\rangle = \int d\Omega\, |\Psi(\Omega)\rangle\, \mathrm{e}^{-\mathrm{i}\Omega\tau} \tag{2.2}$$

In other words, different frequency components (Ω) contributing to the BFC interfere coherently. Therefore, the joint temporal correlation, or time correlation function, is an effect that reflects broadband phase coherence. Consequently, the most straightforward way to certify high-dimensional frequency bin entanglement is through a direct measurement of the relative timing between signal and idler photons [57]. However, the timing resolution

(jitter) of commercially available single-photon detectors ($\sim 50 - 80$ ps) is inadequate to resolve fine features in the time correlation function when the separation between frequency bins is on the order of a few GHz or more. These measurements become even more challenging as the degree of multilevel entanglement increases because the finest features in the time correlation function have a duration set by the total biphoton bandwidth.

2.1 Certifying frequency bin entanglement in a two-dimensional BFC

To overcome this limitation, techniques have been developed to project the two-photon state onto different bases in a manner analogous to those used to characterize high-dimensional time-bin entanglement [58]. In the spectral domain such operations require frequency mixing, which has been implemented, albeit probabilistically, using electro-optic phase modulators (**EOMs**) [48], [49], [52]. In this section we present an overview of one such measurement with a two-dimensional BFC.

2.1.1 State preparation

Broadband, co-polarized time-energy entangled photons are generated by SPDC in a periodically-poled lithium niobate (**PPLN**) waveguide engineered for type-0 phase matching [**Fig. 2.2**]. By suitably programming the amplitude and phase response of the pulse shaper, one projects the biphoton onto a state of the form $|\Psi\rangle_{\text{BFC}} \propto e^{i\phi_1} |1,-1\rangle_{SI} + |3,-3\rangle_{SI}$ [52]. Here –3, –1, 1, and 3 are numerical indices that denote the four discrete frequency bins populated by this state. The separation between bins 1(–1) and 3 (–3) is set to 36 GHz and ϕ_1, which is the *joint* phase between two-photon basis states $|1,-1\rangle_{SI}$ and $|3,-3\rangle_{SI}$, is set by the pulse shaper.

2.1.2 Projection in the frequency domain

To certify frequency-bin entanglement for the BFC shown in **Fig. 2.2**, one needs to establish that the biphoton is in a *coherent* superposition of two-photon basis states $|1,-1\rangle_{SI}$ and $|3,-3\rangle_{SI}$, i.e., that there is a stable phase relationship between them. This can be accomplished by projecting equal contributions of $|1,-1\rangle_{SI}$ and $|3,-3\rangle_{SI}$ into an indistin-

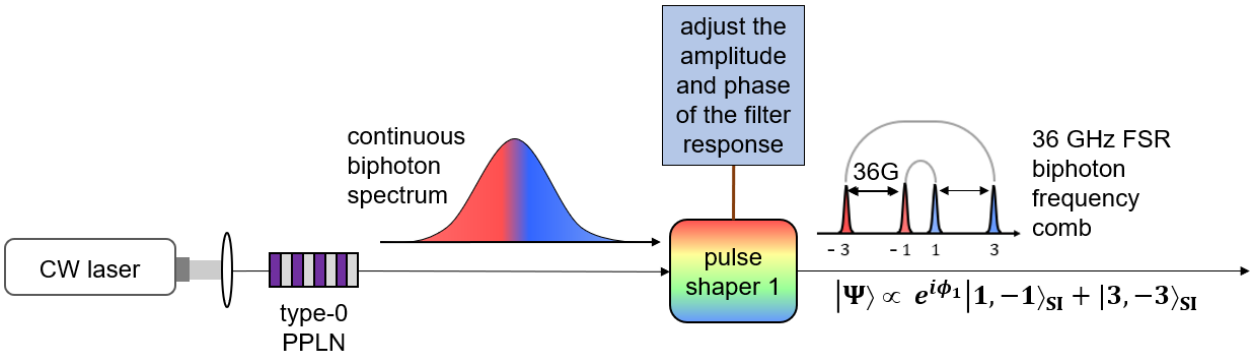

Figure 2.2. Setup for preparing a two-dimensional biphoton frequency comb by carving a continuous biphoton spectrum using a pulse shaper. CW laser, continuous-wave laser; type-0 PPLN, periodically-poled lithium niobate waveguide engineered for type-0 phase matching; FSR, free spectral range.

guishable superposition through frequency mixing. By driving an EOM with a sinusoidal RF tone equal to one-half the frequency bin separation (18 GHz), equal contributions of bins 1 and 3 (-1 and -3) of the signal (idler) are probabilistically scattered into frequency bin 2 (-2) [**Fig. 2.3**]. If the biphoton is in a coherent superposition of basis states $|1,-1\rangle_{SI}$ and $|3,-3\rangle_{SI}$, the probability amplitude of the indistinguishable superposition, i.e., basis state $|2,-2\rangle_{SI}$ will be proportional to $|e^{i\phi_1}+1|^2$. Consequently, by varying the joint phase on $|1,-1\rangle_{SI}$ (ϕ_1) one can vary the probability of detecting coincident photon events between frequency bins ± 2.

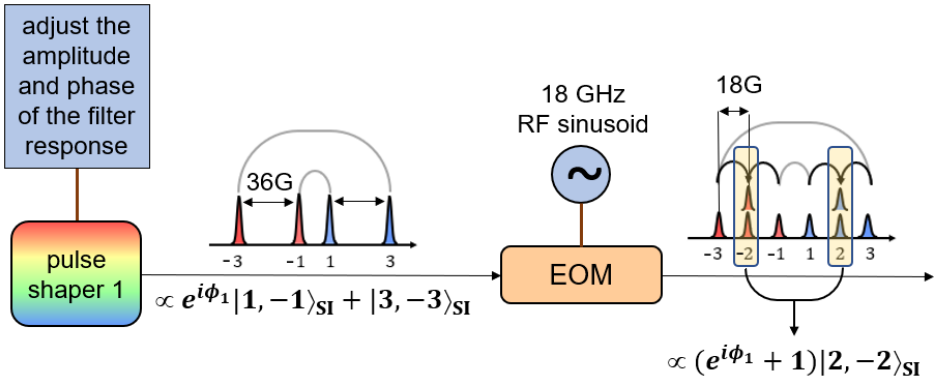

Figure 2.3. Use of an electro-optic phase modulator to project adjacent frequency bins (1 and 3; –3 and –1) into indistinguishable superpositions (bins 2 and –2, respectively). EOM, electro-optic phase modulator.

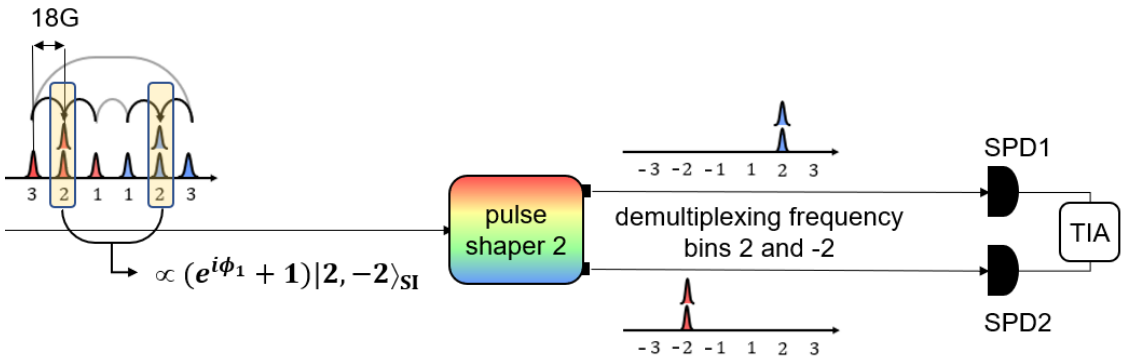

Figure 2.4. Spectral filtering is used to detect coincidences between frequency bins 2 and -2, thereby postselecting for two-photon events corresponding to $|2, -2\rangle_{\mathrm{SI}}$. SPD, single-photon detector; TIA, time interval analyzer.

2.1.3 Spectral filtering and coincidence detection

In order to postselect for $|2, -2\rangle_{SI}$ through coincidence detection, a second pulse shaper (or wavelength-selective switch) ("pulse shaper 2" in **Fig. 2.4**) is used to pass frequency bins 2 and -2 to two different output ports and, eventually, on to different single-photon detectors (**SPDs**). A time interval analyzer (**TIA**) records the delay between single-photon events. By programming the first pulse shaper ("pulse shaper 1" in **Fig. 2.3**) to linearly sweep joint phase ϕ_1 on $|1, -1\rangle_{SI}$, one generates a sinusoidal variation in the probability of detecting $|2, -2\rangle_{\mathrm{SI}}$ at the output [**Fig. 2.5**]. If the interferometric visibility of such a two-photon interference trace exceeds the classical threshold of $\frac{1}{\sqrt{2}}$ needed to violate a Bell inequality (under the assumption of a symmetric or white noise model), one can certify two-dimensional frequency bin entanglement in the BFC [48], [58], [59].

2.1.4 Extension to higher dimensions

The probabilistic nature of the frequency mixing operations described above, coupled with the need for high-speed radiofrequency (**RF**) electronics, makes this method of certifying frequency-bin entanglement challenging. While, in principle, deterministic frequency-mixing operations can be achieved with an alternating series of EOMs and Fourier transform pulse shapers [32], it comes at the cost of increased system loss due to the introduction of ad-

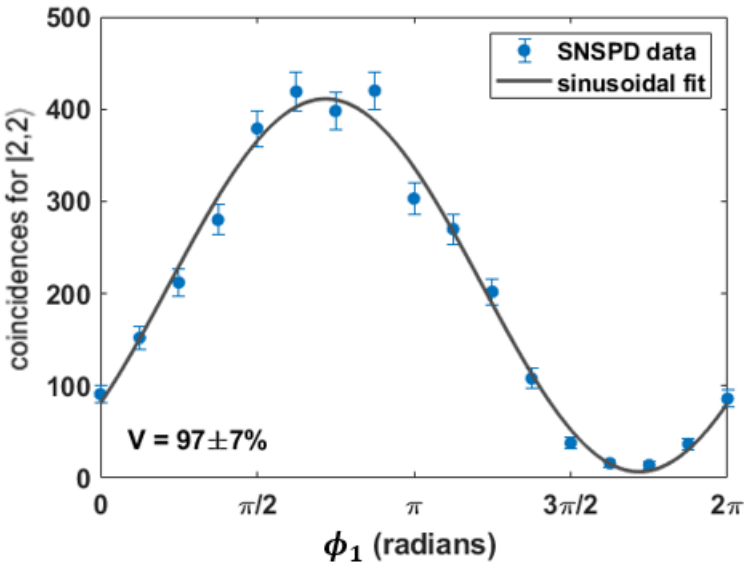

Figure 2.5. Coincidences between frequency bins 2 and -2 as a function of the joint phase on $|1,-1\rangle_{SI}$. The interferometric visibility (V) of $[97\pm7]\%$ exceeds the threshold needed to violate a Bell inequality by close to four standard deviations.

ditional components. These limitations become very apparent in the case of high-dimensional frequency-bin entanglement, which requires one to project d frequency bins into an indistinguishable superposition in order to certify d-level entanglement [49], [52]. The measurement process quickly becomes time consuming and a strain on resources. To date, projective measurements in the frequency domain have been used to certify entanglement only as high as four dimensions [49].

This motivates the need for an alternative method to certify high-dimensional frequency-bin entanglement. It was recently suggested that Hong–Ou–Mandel (**HOM**) interference, which can be sensitive to delays on the order of femtoseconds, can be used to probe features in the joint temporal correlation of a BFC and, therefore, detect the presence of high-dimensional frequency-bin entanglement [60]. Indeed, one of the interesting features of BFCs, noted in early experiments, is their production of HOM "revivals"; i.e., the initial coincidence dip at zero delay reappears (as dips or peaks) at multiples of half the inverse FSR [61]. As each dip has a duration set by the total biphoton bandwidth, HOM revivals are

certainly a broadband effect and could appear, initially, to be an effect exploiting broadband phase coherence as well.

2.2 Hong–Ou–Mandel interference and spectral phase

The state prepared in the previous example does not lead to interference in an HOM interferometer with slow (integrating) detectors because the signal and idler share no common frequencies [63]. If instead of generating (co-polarized) time-energy entangled photons by type-0 SPDC, one instead relies on type-II phase matching and spectrally degenerate down-conversion, one can prepare a BFC where spectrally indistinguishable photons are separated on basis of polarization state with close to unity efficiency [**Fig. 2.6(b)**] [60]. This state can be described by:

$$|\Psi\rangle_{\mathrm{BFC}} = \sum_{p=-N,\, p\neq 0}^{N} \alpha_p \, |p, -p\rangle_{AB} \tag{2.3}$$

Subscripts A and B signify the two paths populated by the vertically- (signal) and horizontally-polarized (idler) photons after they are separated by a polarizing beam splitter with output paths A and B. Another critical distinction is that for the BFC described in equation 2.3 [**Fig. 2.6(b)**] each photon populates $2N$ bins (from $-N$ to N, excepting 0). This is unlike the co-polarized BFC in equation 2.1 [**Fig. 2.6(a)**] where the signal (idler) populates only the upper (lower) half of the spectrum, i.e., N bins.

Although the two photons in **Fig. 2.6(b)** are spectrally indistinguishable, none of the individual two-photon basis states $|-p, p\rangle_{\mathrm{AB}}$, on their own, gives rise to HOM interference with slow detectors because photons A and B populate different frequency bins. However, one can define a so-called *comb line pair*:

$$|\psi\rangle_p = \alpha_p \, |p, -p\rangle_{AB} + \alpha_{-p} \, |-p, p\rangle_{AB} \tag{2.4}$$

↑The results of this section have been published in [62]

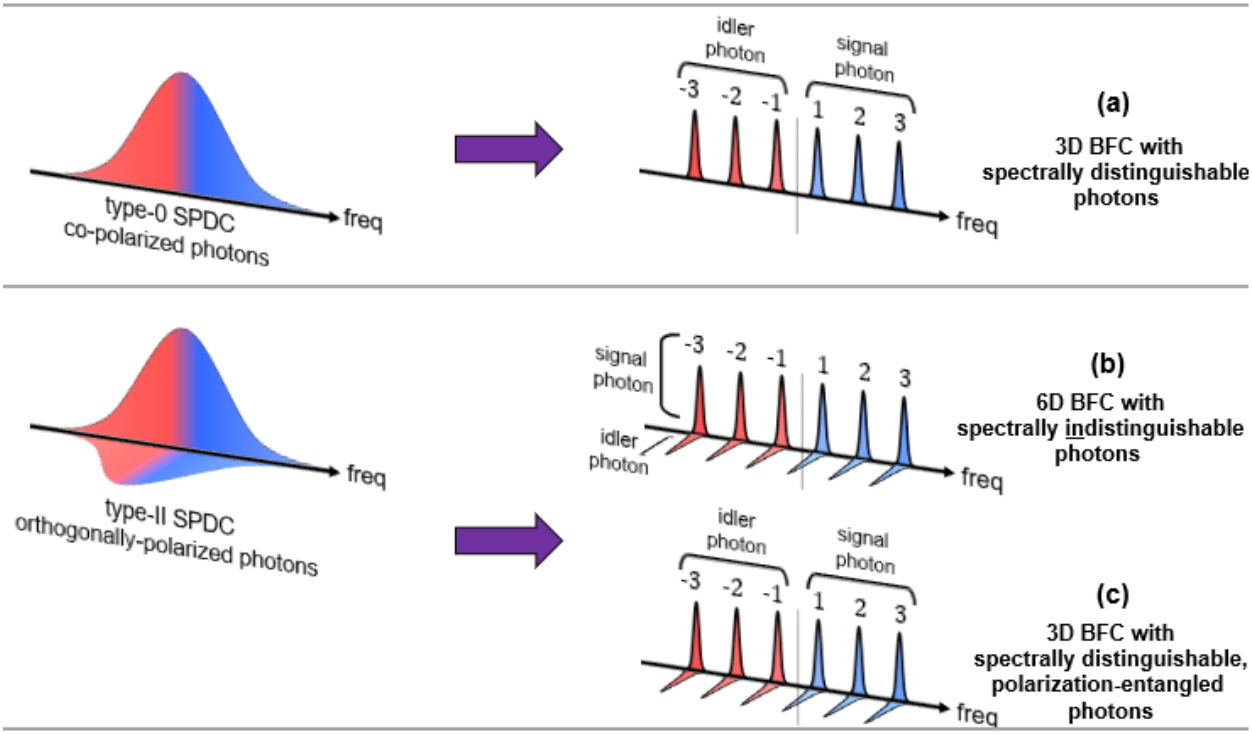

Figure 2.6. (a) By carving a continuous type-0 down conversion spectrum using a 6-bin filter, one can prepare a 3D BFC where signal and idler are distinguished on the basis of frequency. (b) The same 6-bin filter applied to a type-II down conversion spectrum results in a 6D BFC with spectrally indistinguishable photons when those photons are separated on the basis of polarization state. (c) If photons are instead distinguished on the basis of frequency, one can prepare a 3D BFC also entangled in polarization state.

Here both photons populate the same two frequency bins, $-p$ and p in superposition, and produce a nontrivial HOM interferogram. The BFC in equation 2.3 can now be rewritten as a sum of such comb line pairs:

$$|\Psi\rangle_{\mathrm{BFC}} = \sum_{p\,=\,1}^{N} \mathrm{e}^{\mathrm{i}\beta_p}\,|\psi\rangle_p \tag{2.5}$$

Here β_p is the joint phase on p^{th} *comb line pair*. If HOM interference is able to probe the fast substructure in the time correlation function [**Fig. 2.1(b)**] and, therefore, high-dimensional entanglement, it must be sensitive to changes in β_p since temporal correlations between photons in a BFC are an effect of broadband phase coherence [56].

2.2.1 Hong–Ou–Mandel Interferometer

We designed a HOM interferometer [**Fig.** 2.7] that allows one to manipulate β_p, the joint phase on individual comb line pairs. Time-energy entangled photon pairs are generated by colinear, type-II SPDC in a fiber-coupled, PPLN ridge waveguide. The PPLN (temperature = 54.1°C) is pumped with continuous-wave (**CW**) laser light at a wavelength of ∼779.4 nm, chosen to ensure that time-energy entangled photons generated by the down-conversion process are spectrally degenerate. Owing to the type-II process, down-converted photons are separated deterministically with a 1×2 fiber-based polarizing beam splitter (**PBS**).

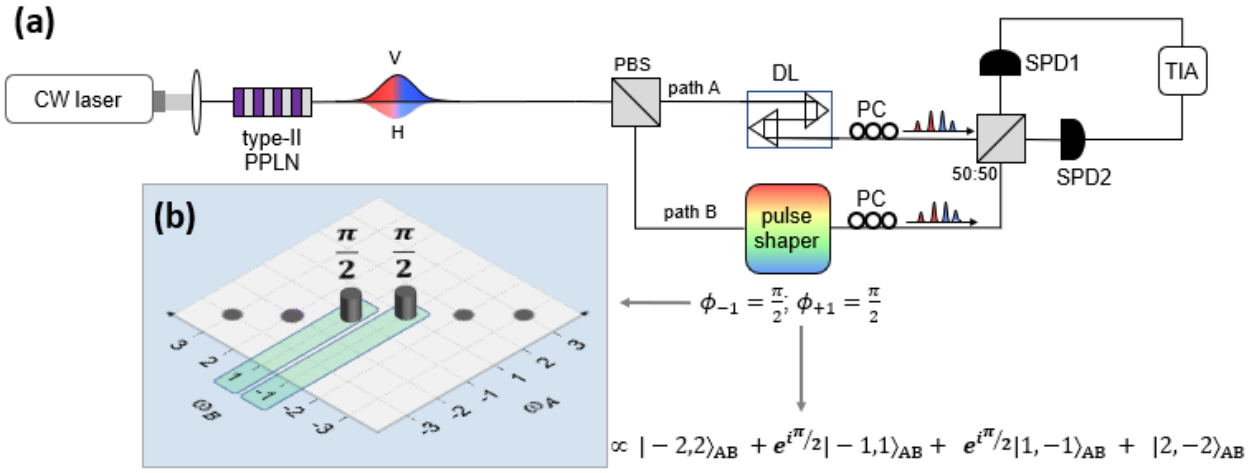

Figure 2.7. (a) Experimental arrangement (see text for details). PPLN, periodically-poled lithium niobate waveguide; PBS, fiber-based polarizing beam splitter; PC, polarization controller; 50 : 50, 2×2 fiber-based 50 : 50 beam splitter; SPD, single-photon detector; TIA, time interval analyzer. (b) Joint phase accumulated by the BFC when a phase of $\pi/2$ is applied to both frequency bins -1 and 1 in photon B

One arm of the HOM interferometer (path A) includes two optical delay lines – a 330 ps manually-actuated delay line and a 167 ps motorized delay line. The former is used for coarse matching of the delay between paths A and B, while the latter for scanning the path length difference in two-photon interference experiments. The other arm (path B) includes a Fourier-transform pulse shaper, which carves BFCs from the continuous down conversion spectrum, as well as applies the desired phase to individual frequency bins. An important point to note here is that with the pulse shaper in path B alone, it acts on just one of the

photons. However, this is sufficient to generate comb-like correlations in the joint spectrum since coincidence measurements postselect energy-matched frequencies of the photon in path A. Longpass filters, in conjunction with a pair of collimators (not shown), are used in both arms of the HOM interferometer to reject residual pump light.

Downstream of the delay lines and pulse shaper, photons A and B are mixed at a fiber-based 50 : 50 beam splitter. Interference between two-photon probability amplitudes is observed by monitoring two-photon events between the output ports of the HOM interferometer using superconducting nanowire single-photon detectors (**SNSPDs**) and a TIA.

Our experiments are based on a simple but illustrative system – a four-bin BFC. Note that unlike co-polarized BFCs, each photon populates the same four frequency bins, leading to four-dimensional single-photon subspaces and not two as was the case in **Fig. 2.2**. Our four-bin BFC is simply then a coherent superposition of two comb lines pairs (see equation 2.5) – $|\psi\rangle_1$ and $|\psi\rangle_2$. Each frequency bin has a Gaussian profile with an intensity full width at half-maximum (**FWHM**) of 17 GHz; the FSR was chosen to be 90 GHz. This effective fill factor ($17/90 \sim 0.2$) offers an acceptable trade-off between the overall count rate and the number of revivals in the HOM interference trace.

2.2.2 Sensitivity of HOM interference to changes in spectral phase

To probe the sensitivity of HOM interference to spectral phase, we varied β_1, the joint phase on comb line pair $|\psi\rangle_1$, by applying the desired phase to both the -1 and 1 frequency bins of the photon in path B [**Fig. 2.7(b)**]. We recorded HOM interferograms for three cases: $\beta_1 \in \{0, \frac{\pi}{2}, \boldsymbol{\pi}\}$. An illustration of these operations, the ensuing modification of two-photon basis states, and the corresponding HOM interference traces are shown in **Fig. 2.8**. Coincidences are recorded over 1 second intervals and reported without background subtraction. The visibilities of these traces are lower than that of the unfiltered down-conversion spectrum ($[99.6 \pm 1.2]\%$, not shown) because we increased the pair production rate to counteract the significant reduction in counts associated with carving just four discrete bins from a 310 GHz-wide biphoton spectrum. Although there is some noticeable drift in the interfer-

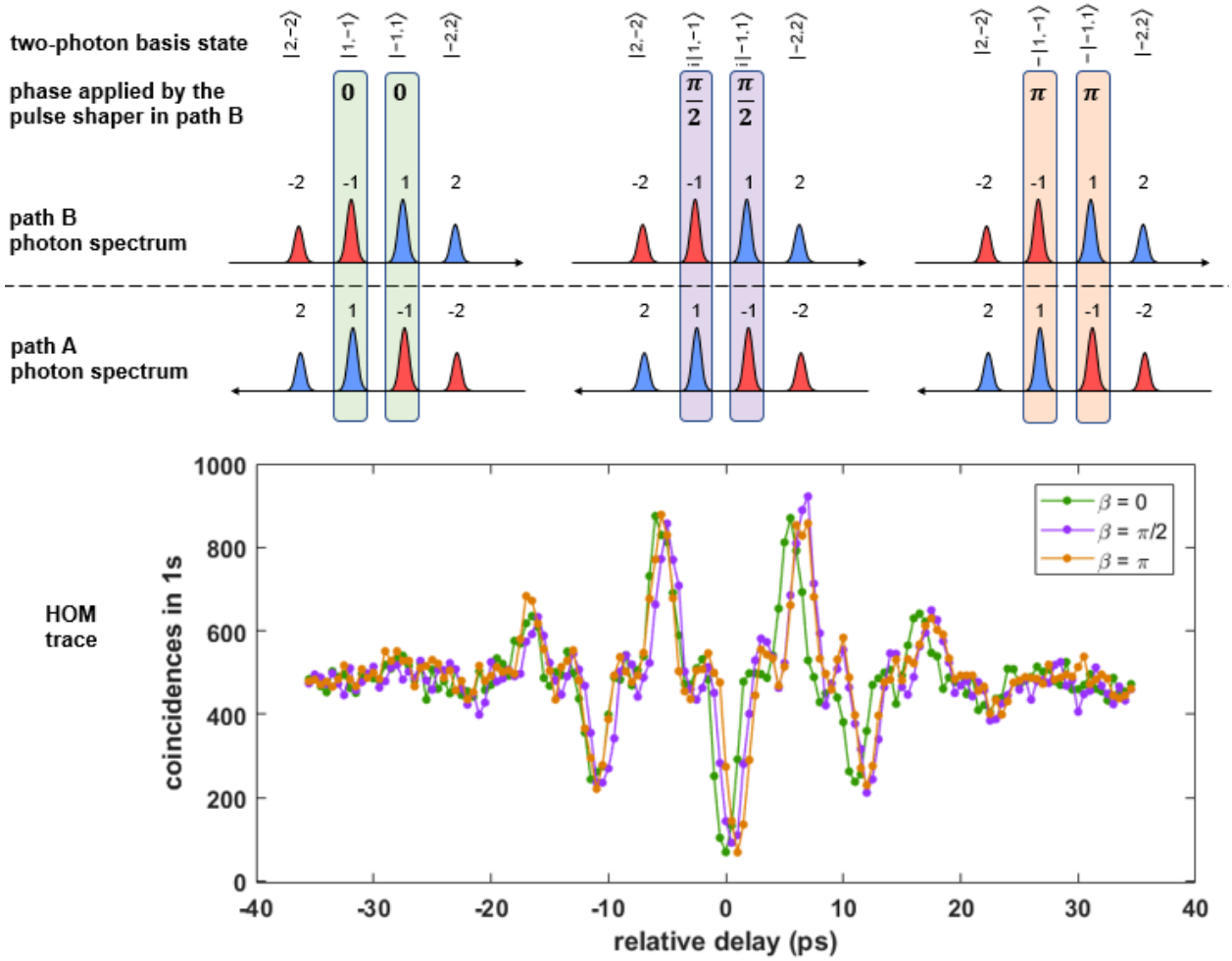

Figure 2.8. HOM interference traces for four-bin BFCs with different values of β_1 – the joint phase on comb line pair $|\psi\rangle_1$. In this and subsequent figures, the axes of photon spectra in paths$A$ and B are reversed with respect to one another. This has been done to visually align frequency bins that contribute to the same two-photon basis state. For clarity, high and low frequencies are colored blue and red, respectively, and are defined with respect to the center of the photon spectrum. To facilitate an easy comparison between overlaid HOM interference traces, experimental data (solid circles) for consecutive delay steps are connected by straight lines.

ometer that occurs during acquisition of the $\beta_1 = 0$ interference trace, there is no discernable difference in HOM interference with different values of β_1.

2.2.3 Distinguishing pure states from mixed states

Having shown that HOM interference is insensitive to the relative phase between comb line pairs in a coherent superposition state, we now examine whether the HOM interferometer

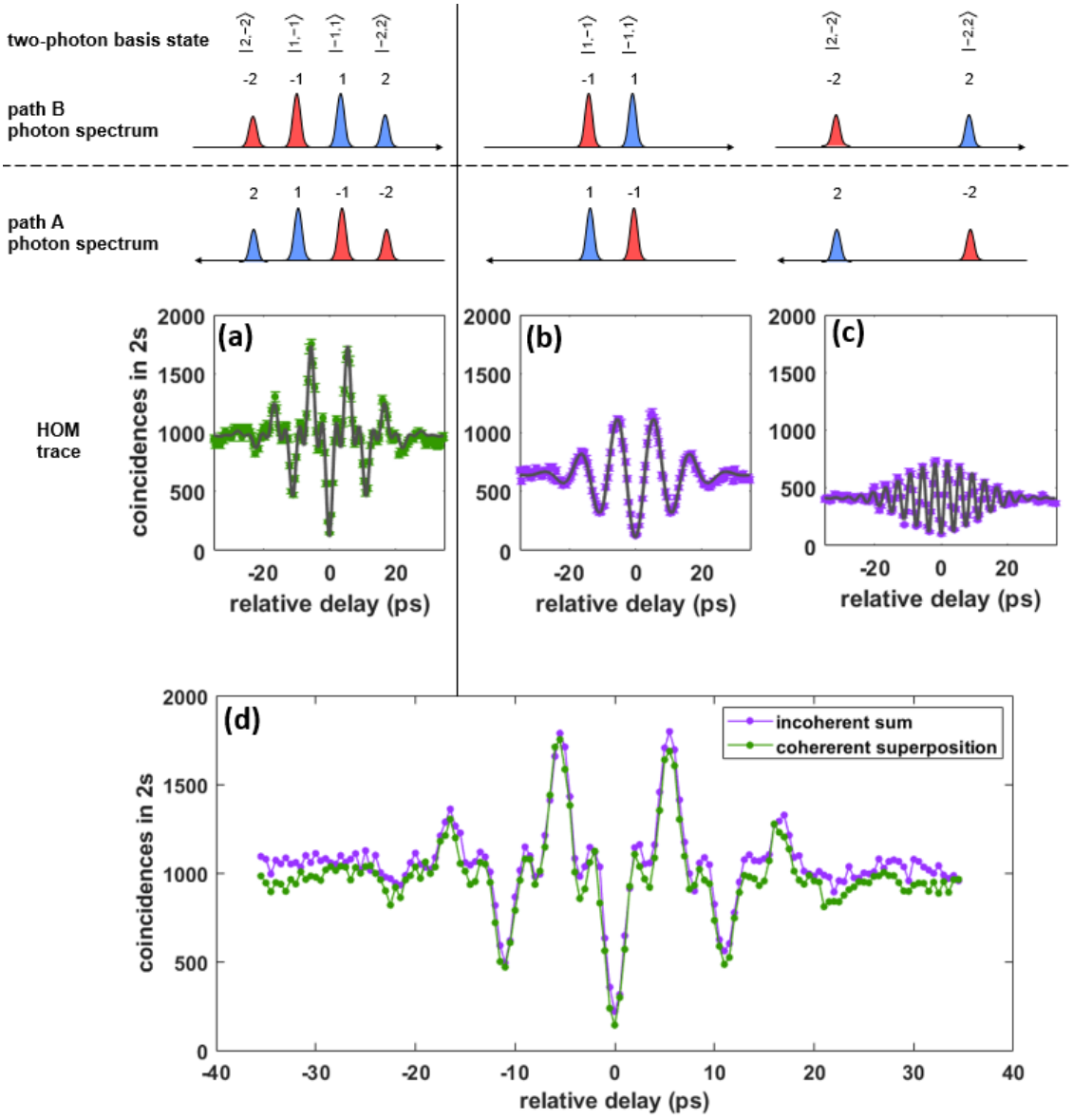

Figure 2.9. HOM interference traces for (a) a coherent superposition state – $|\Psi\rangle_{\mathrm{BFC}} = |\psi\rangle_1 + |\psi\rangle_2$, (b) comb line pair $|\psi\rangle_1$ only, and (c) comb line pair $|\psi\rangle_2$ only. (d) Comparison of HOM interference for a coherent superposition state [trace (a)] with that for a mixture of the corresponding comb line pairs [trace (b) + trace (c)].

can, in any way, distinguish between a coherent superposition state and the corresponding mixture. In other words, can one distinguish between high-dimensional and two-dimensional frequency-bin entanglement via an HOM measurement? For this comparison, we first record an HOM interferogram for the four-bin BFC –- a coherent superposition of two comb line pairs $|\psi\rangle_1$ and $|\psi\rangle_2$. In the case of the corresponding mixed state, there is no stable phase relationship between the constituent comb line pairs. In other words, the mixture is simply an incoherent sum of two pure states –- $|\psi\rangle_1$ and $|\psi\rangle_2$. Consequently, an HOM interference trace for the mixture can be constructed by recording interferograms for the two comb line pairs individually and adding the results together. This is the situation that would result from repeated random emission of either $|\psi\rangle_1$ or $|\psi\rangle_2$, but not both in superposition. The HOM traces for these two cases –- a coherent superposition of two comb line pairs and the corresponding mixture – are presented alongside one another in **Fig. 2.9(d)**. Both traces clearly track one another quite closely.

The results in **Figs. 2.8 and 2.9** confirm two key points: neither the specific phase between two comb line pairs in a superposition state, nor even the presence of inter-pair coherence more generally, has any bearing on the HOM interferogram. Therefore, HOM interference cannot be used to detect or certify high-dimensional frequency-bin entanglement in a BFC.

2.3 Quantum walks and high-dimensional entanglement

As noted in section 2.1.4, one can certify d-level entanglement by projecting d frequency bins into an indistinguishable superposition (in each of the signal and idler) followed by coincidence measurements to postselect for two-photon events corresponding to this indistinguishable superposition of d frequency bins. This method borrows heavily from techniques developed to characterize time-bin entanglement [58]. However, modern telecommunications infrastructure is based on selective processing and routing of information in the spectral domain and, consequently, there is a wider range of tools with which to manipulate frequency-encoded quantum information. Take the case of EOMs and chirped fiber Bragg gratings, for

†The results of this section have been published in [64]

example. The former acts as a tunable multiport frequency bin beam splitter and the latter introduces frequency bin-dependent time delays. There are simply no commercially available components to manipulate time bins in analogous ways. This naturally raises the question of whether a technique for entanglement certification unique to the needs and advantages of frequency can be devised.

Another drawback of the method outlined in section 2.1 is that it discards a large amount of information. This is because one only tabulates coincidences between two frequency bins when, in fact, we have complex multimode quantum interference spanning many frequency bins. Such parallelized (in the frequency domain) quantum interference bears strong resemblance to photonic quantum walks.

In general, all that is required to implement a photonic quantum walk is the presence of coupling between different modes in a given degree of freedom [65]–[68]. Such coupling, or mode scattering, is generated in EOMs driven with a single sinusoidal RF tone. The effect of this perturbation is that the wavefunction of a photon traversing the EOM picks up a factor of $e^{i\delta \cos \omega_m t}$. Here δ corresponds to the strength of the modulating RF field and ω_m denotes the frequency of RF modulation. Viewed from the perspective of the frequency domain, phase modulation scatters a single frequency bin into a comb-like spectrum with adjacent frequency bins separated by ω_m. The amplitude of a frequency bin a distance $n\omega_m$ away from the original bin is given by n^{th} order Bessel function $J_n(\delta)$. In analogy to quantum walks based on path encoding, the depth a frequency domain quantum walk can be incremented simply by cascading one EOM after another. However, a particular strength of the frequency domain approach is that a cascade of n identical EOMs is equivalent to increasing the strength of the modulating RF field in a *single* EOM by this factor of n. *In other words, the depth of the walk can be tuned over a continuous range by simply modifying the strength of the modulating RF field.*

Fig. 2.10(a) shows results for the (classical) evolution of single frequency mode through an EOM as a function of modulation depth (δ). As wave dynamics in the classical regime are equivalent to single-photon quantum walks, such measurements are sometimes referred to as coherent random walks [69]. This is because their evolution through the system is no different from that of a single photon occupying the same set of input frequency bins. As

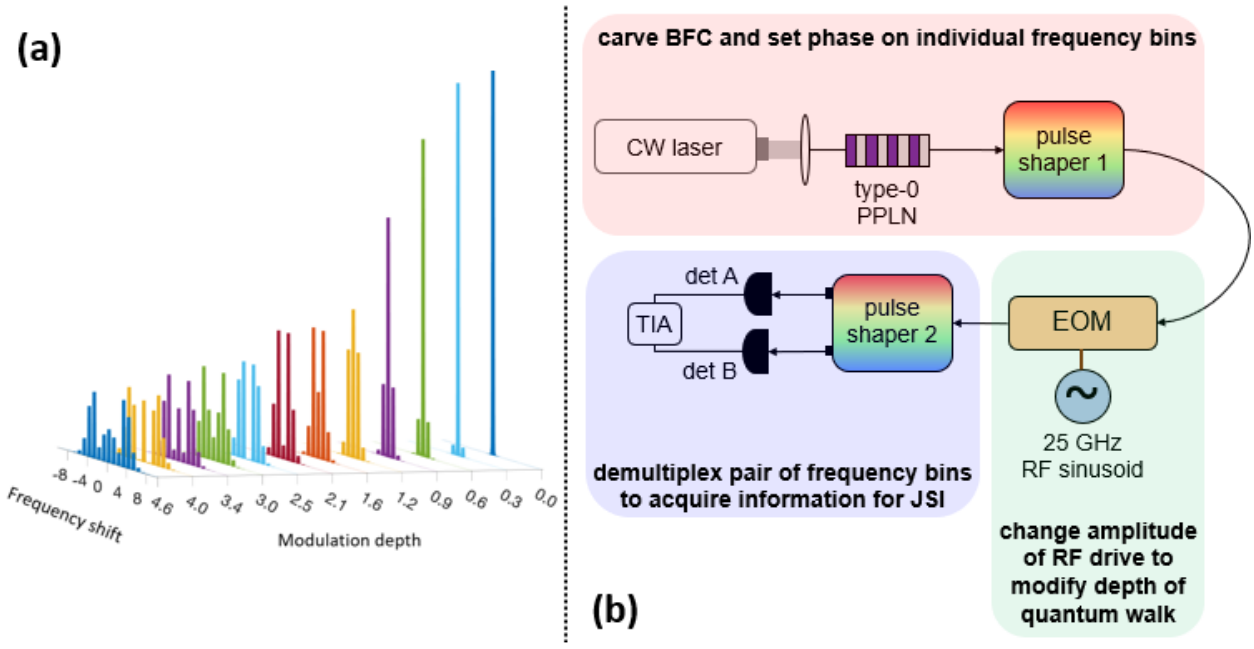

Figure 2.10. (a) Evolution of a single frequency mode through an EOM as a function of the RF modulation depth (b) Experimental setup to implement a photonic quantum walk in the frequency domain with BFCs. CW laser, continuous-wave laser; PPLN, periodically-poled lithium niobate; EOM, electro-optic phase modulator; RF, radio frequency; det, single-photon detector; TIA, time interval analyzer; JSI, joint spectral intensity.

the strength of the modulating field increases, the extent to which the input frequency bin scatters to outer frequency bins also increases. Quantum walks of entangled particles [65], particularly those featuring high-dimensional entanglement [67], exhibit a richer variety of behavior than is possible with just a single photon occupying a single frequency bin. To explore the effect of entanglement on quantum walks in the frequency domain, we study the evolution of BFCs under electro-optic modulation.

2.3.1 Multimode quantum interference in the spectral domain

Like the demonstration in section 2.1, BFCs are carved from a continuous biphoton spectrum generated by type-0 SPDC [**Fig. 2.10(b)**]. This is unlike the preceding study (section 2.2), where we relied on type-II phase matching. The linewidth of each frequency bin is 9 GHz FWHM. To ensure minimal crosstalk between adjacent frequency bins, the

FSR of the BFC is set to 25 GHz. Pulse shaper 1 [**Fig. 2.10(b)**] not only manipulates the amplitude of the biphoton spectrum, but also its phase prior to a quantum walk. In particular, the spectral phase can be set to vary continuously or make discrete jumps from one frequency bin to the next. Once the desired state has been prepared, it is sent to an EOM to mix frequency bins, which gives rise to a quantum walk in frequency (energy) space. The EOM is driven with a 25 GHz sinusoidal RF tone – identical to the FSR of the BFC – with the RF power tunable over a continuous range. Downstream of the modulator is pulse shaper 2 [see **Fig. 2.10(b)**], which selects a pair of output frequencies and routes each one to a different SNSPD. Two-photon events between different pairs of frequency bins are identified by correlations in their arrival time. This data is used to construct a measurement of the joint spectral intensity (**JSI**) of the BFC – a two-photon correlation map that captures the effect of a quantum walk. It is worth noting that this quantum walk uses the same sequence of elements used to certify frequency bin entanglement (section 2.1).

2.3.2 Enhanced ballistic energy transport

One hallmark of a correlated quantum walk is the rapid diffusion two-photon correlations away from the original map. We observe such transport in a BFC entangled across eight pairs of frequency bins and ideally in the form $\frac{1}{\sqrt{8}} \sum_{p=1}^{8} |p, -p\rangle_{SI}$. The joint spectral intensity of the initial state, i.e., in the absence of any modulating RF field, is completely anti-correlated in frequency [**Fig. 2.11(a)**]. Each pixel on the diagonal corresponds to the same two-photon energy, i.e., the sum of the two frequency bin indices at any pixel on this line is zero. Note that the sum of the frequency bin indices on any line parallel to the diagonal is a constant that simply corresponds to a different value for the total energy of the two-photon state. **Fig. 2.11(b)** shows the joint spectrum of this state *after* a quantum walk when the modulator is driven to a depth $\delta = 4.6$ radians. Experimental data clearly show diffusion, or transport, of two-photon correlations away from the original JSI. Transport perpendicular to the diagonal and towards the top right corner of the JSI corresponds to events where the overall energy of the biphoton increases, i.e., the modulator transfers energy to the two-photon state. The converse, when the biphoton gives up energy to the modulator, manifests

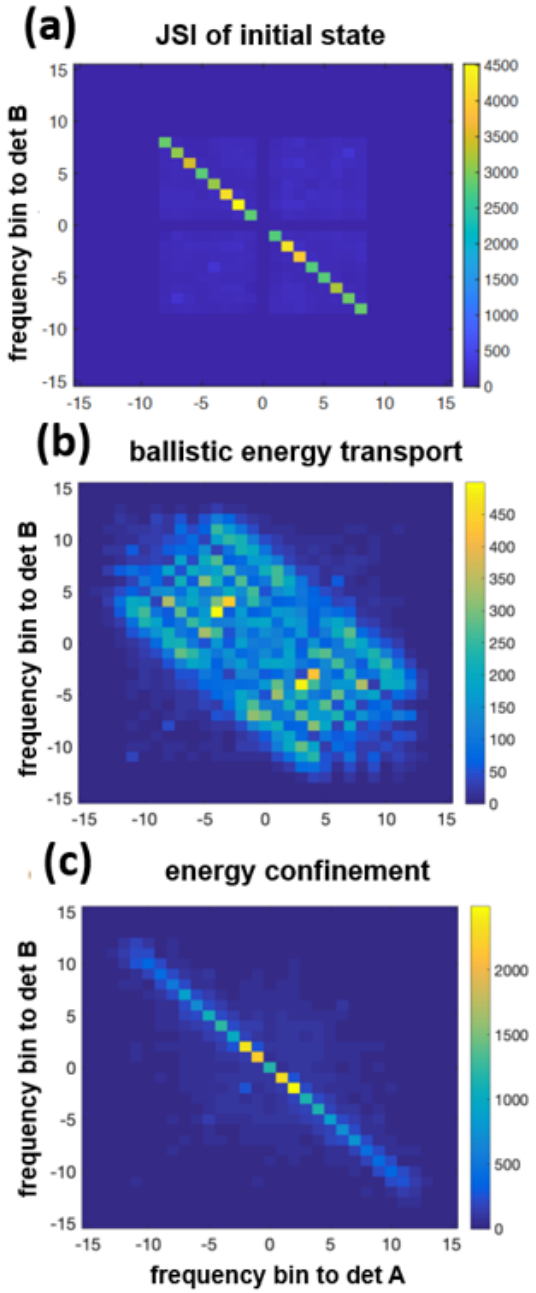

Figure 2.11. Joint spectral intensity constructed from coincidence measurements between different pairs of frequency bins across a 31×31 grid. (a) 8-bin BFC with no applied RF modulation, (b) 8-bin BFC and RF modulation index of 4.6 radians, but no applied spectral phase, and (c) 8-bin BFC and RF modulation index of 4.6 radians, as well as a π phase shift between adjacent comb line pairs $|p, -p\rangle_{SI}$

as transport to the lower left corner of the JSI. In other words, what we observe is two photons experiencing similar frequency shifts (at least in sign), which resembles, but is qualitatively different from, bosonic bunching (HOM interference) in the frequency domain [70].

To quantify this energy transfer, we tabulate the total number events along the diagonal and do the same for each line parallel to the diagonal. Each of these event totals corresponds to the probability of a biphoton exiting the system with the corresponding total energy.

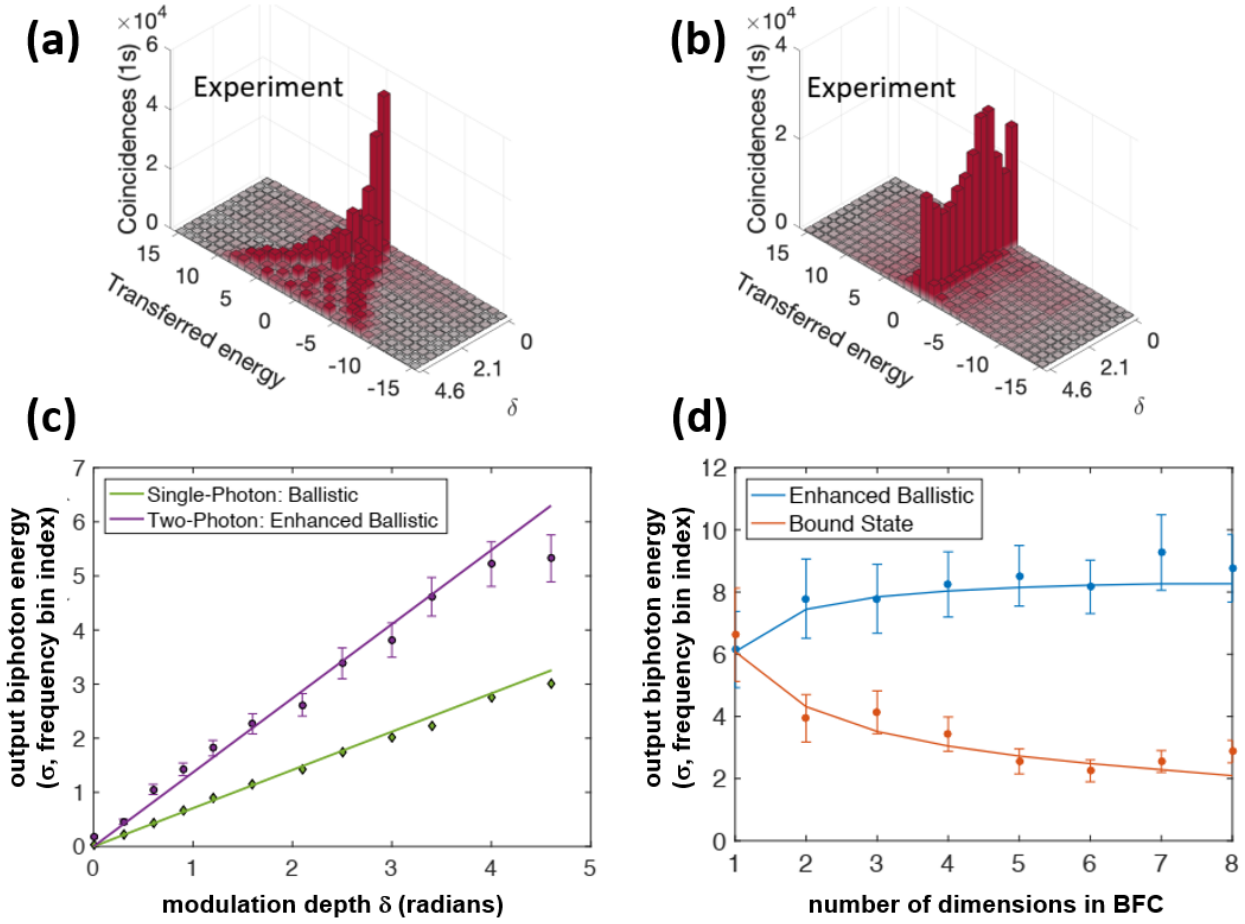

Figure 2.12. Distribution of biphoton energies at the output of the circuit, i.e., at the conclusion of a quantum walk, for states (a) $|\psi\rangle \propto \sum_{p=1}^{8} |p, -p\rangle_{SI}$ and (b) $|\psi\rangle \propto \sum_{p=1}^{8} e^{ip\pi} |p, -p\rangle_{SI}$. Energies reported in units of $h \times 25$ GHz. (c) Standard deviation (σ) of biphoton energies at the output of the circuit as a function of modulation index (walk depth) for the single-photon and two-photon cases. (d) Standard deviation (σ) of biphoton energies at the output of the circuit as function of the degree of multilevel entanglement for the case of enhanced ballistic transport and the so-called bound state, which is characterized by strong energy confinement.

Energy transfer between the EOM and the two-photon state, expressed in terms of the sum of (the changes in) frequency bin indices, is plotted in **Fig. 2.12(a)** as a function of modulation depth δ. The standard deviation of biphoton energies at the output, as in the single photon case, is linear with modulation depth δ [purple markers, **Fig. 2.12(c)**]. However, this linear scaling of energy transfer is approximately twice as fast in the case of entangled photons.

2.3.3 Strong energy confinement

The diffusion of two-photon correlations is dramatically altered if we modify the spectral phase of the BFC to create a state of the form $\frac{1}{\sqrt{8}} \sum_{p=1}^{8} e^{ip\pi} |p, -p\rangle_{SI}$, i.e., a state in which adjacent comb line pairs $|p, -p\rangle_{SI}$ have a π phase difference with respect to one another. This operation can be viewed as a linear spectral phase ramp, which is equivalent to delaying one photon with respect to its entangled counterpart by half the modulation period. As a result of this delay, photons in an entangled pair acquire equal but opposite frequency shifts. This is clearly illustrated by the JSI measurement after a quantum walk [**Fig. 2.11(c)**], which shows that frequency correlations remain largely confined to the diagonal. In other words, the energy of the two-photon state is largely unchanged. As the duration of the walk, i.e., modulation depth δ increases, frequency correlations merely propagate outward along the diagonal to include new combinations of high and low photon frequencies. However, this energy gain or loss is correlated within a photon pair. If the idler gains some energy, the signal loses that same amount of energy with the result that the total energy of the state is preserved [**Fig. 2.12(b)**].

2.3.4 Quantum walks and the joint temporal correlation

The evolution of the biphoton, as captured by two-photon correlation maps [**Fig. 2.11**], can also be understood from a time domain consideration of the quantum walk, which better illustrates how electro-optic phase modulation interacts with the signal–idler arrival time. In **Fig. 2.13**, the strength of the modulating RF waveform is shown (dark blue sinusoid) as a function of time. The signal photon, which can arrive at the modulator at any time

owing to the random nature of the SPDC process, is designated by a blue arrow capped by a blue sphere. In **Fig. 2.13**, we only show one possible arrival time. Here, for example, the signal reaches the modulator when the phase of the modulating RF waveform is $\frac{\pi}{6}$. While the idler photon also reaches the modulator at a random time, *this random time is highly correlated* with the arrival of the signal photon. This correlation is characterized by a range of possible values for the delay between signal and idler, which is given by the Fourier transform of the complex biphoton spectrum [56]. Consequently, for a narrowband biphoton with entanglement across a limited number of dimensions (see 8-dimensional BFC in **Fig. 2.13**), there is a wide range of possible values for the relative delay between signal and idler (orange train of sinc-squared functions capped by orange spheres). As the degree of multilevel entanglement increases and, therefore, the biphoton bandwidth, the distribution of possible signal-idler delays gets narrower (see 64-dimensional BFC in **Fig. 2.13**). The discretization of the biphoton spectrum in frequency space, owing to its comb-like structure, results in a distribution of relative arrival times that repeats at integer multiples of the inverse FSR of the BFC. Since the spacing between frequency bins matches that of the RF waveform, this repetition of the distribution in arrival times occurs at integer multiples modulation period. The net effect is that both photons "see" nearly the same phase modulation ramp ($\frac{d\phi}{dt}$), which means they experience correlated instantaneous frequency shifts (see correlated energy transfer in **Fig. 2.13**).

In the case of walks featuring energy confinement [**Fig. 2.11(c)**], the situation is slightly different. Here there is a $\boldsymbol{\pi}$ phase difference between adjacent comb line pairs, which corresponds to a linear spectral phase ramp or simply an additional time delay between signal and idler. This delay is exactly one-half the RF modulation period. In other words, the distribution in the relative arrival of signal and idler is centered at half-integer multiples of the modulation period. Here, unlike in the case of ballistic transport described in the previous paragraph, photons in an entangled pair experience anti-correlated instantaneous frequency shifts (anti-correlated energy transfer in **Fig. 2.13**), which manifests through confinement of two-photon correlations to the diagonal of a JSI measurement.

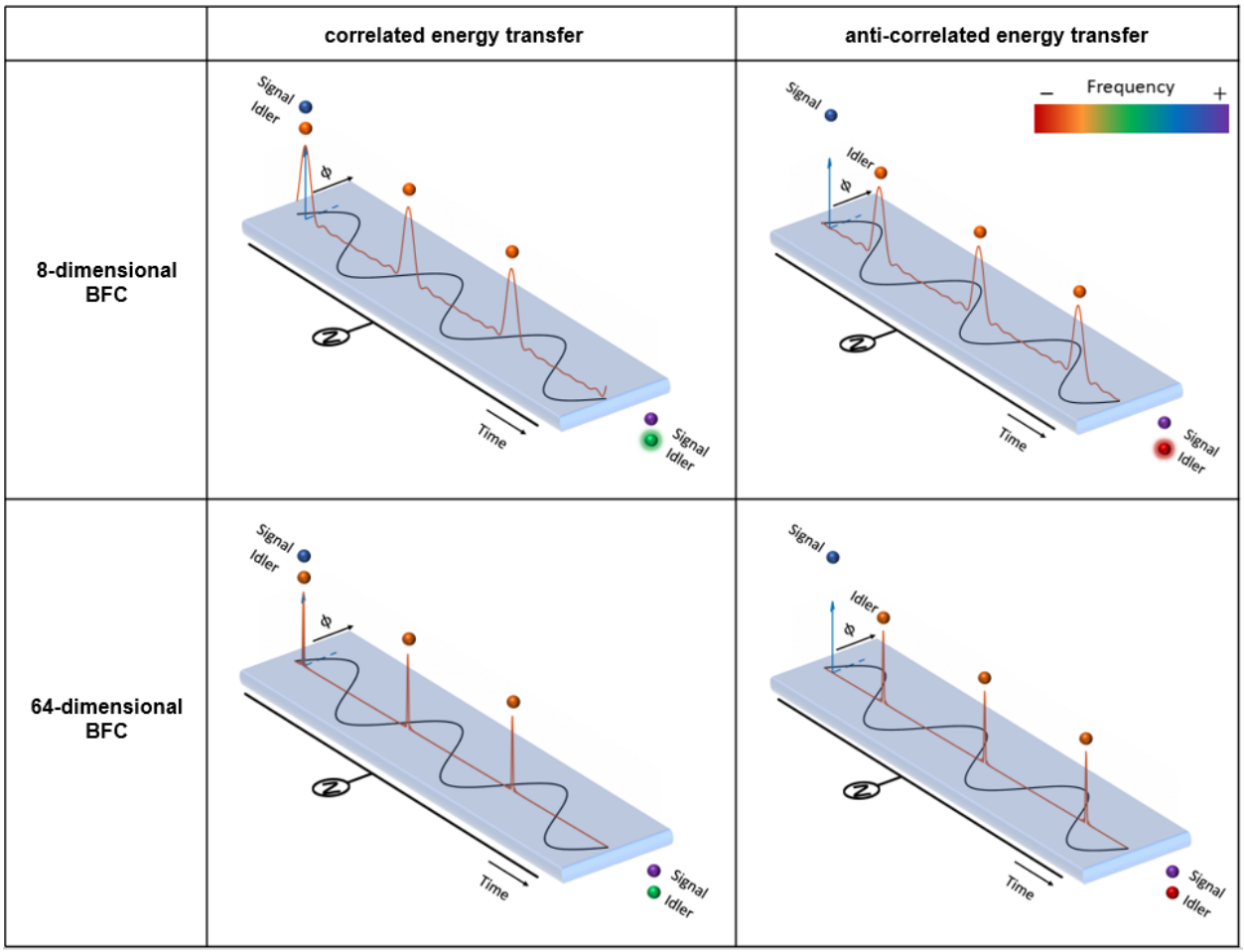

Figure 2.13. Time domain illustration of how energy transfer between the modulator and the BFC is affected by the relative timing between signal and idler. The two rows highlight how the process differs between an 8-dimensional BFC and a 64-dimensional BFC. The latter is characterized by a narrower spread in the mapping between energy transfer and relative arrival time. The two columns highlight the effect of different spectral phase patterns – one results in correlated signal-idler frequency shifts and the other in anti-correlated signal-idler frequency shifts.

2.3.5 Effect of high-dimensional entanglement

The critical role played by spectral phase hints at strong differences between quantum walks featuring coherent superpositions of multiple frequency bin pairs $\frac{1}{\sqrt{N}}\sum_{p=1}^{N}|p,-p\rangle_{SI}$ as compared to the corresponding mixed state $\rho=\frac{1}{N}\sum_{p=1}^{N}|p,-p\rangle_{SI}\langle p,-p|_{SI}$. While both states possess identical spectral correlations, i.e., JSIs, for the latter the relative phase be-

tween any two basis states ($|p,-p\rangle_{SI}$ and $|q,-q\rangle_{SI}$ for $p \neq q$) is completely random. To simulate the effect of this random phase, we constructed a JSI measurement of the mixed state by adding together JSI measurements from quantum walks with individual comb line pairs $|p,-p\rangle_{SI}$ for $p = 1, 2, ...8$. We find that one consequence of such incoherence is that two-photon correlations are smeared without any sharp or well-defined features (not shown).

This result, together with the quantum walks presented earlier, suggest that the total energy of the two-photon state after a quantum walk can serve as an indicium of the coherence between comb line pairs. One metric to quantify this is the standard deviation of biphoton energies measured at the output. This is presented in terms of the (change in) frequency bin index (single-photon case) and the sum of (the changes in) frequency bin indices (two-photon case), as a function of walk duration, in **Fig. 2.12(c)**. We clearly see enhanced energy transfer for the two-photon state. In the limit of infinite multilevel entanglement, energy transfer increases at twice the rate for two-photon correlations compared to single-photon quantum walks since both photons experience exactly the same frequency shift.

To elucidate the effect of high-dimensional entanglement, we present data for energy transfer in the cases of enhanced ballistic scattering [**Fig. 2.12(d)**, blue markers] and strong energy confinement [**Fig. 2.12(d)**, red markers]. These plots show how the standard deviation of biphoton energies at the output changes as the degree of multilevel entanglement increases for a fixed walk depth ($\delta = 6.1$ radians). The clear change in the distribution of biphoton energies as a function of entanglement dimensionality, especially in the case of strong energy confinement or a so-called bound state, points to how these results can potentially be used to certify and even quantify high-dimensional frequency-bin entanglement. Our results show that the width or timing uncertainty associated with the time correlation function is mapped to a corresponding spread in biphoton energies at the output of a quantum walk. While a rigorous proof is needed to establish the validity of this technique for entanglement certification and quantification, these walks clearly allow one to probe temporal features in the biphoton that cannot be resolved by direct measurements.

2.4 Discrete Fourier Transform Gate

A more direct route to characterizing entanglement is measuring correlations in each of two mutually unbiased bases (**MUBs**). The concept of mutually unbiased bases is perhaps easiest to convey by considering the case of polarization. If a photon prepared in the rectilinear (HV) basis is horizontally-polarized and subsequently measured in this basis, only one result is returned $-$ H. However, if this photon is measured in the diagonal basis (AD), all possible outcomes (A or D) are equally likely. In other words, each mode in one basis is mapped to all modes with equal probability in a mutually unbiased basis.

In the case of frequency-encoded quantum information, we take the basis of frequency modes ($|m\rangle$, where m denotes a mode centered at frequency ω_m) as the computational basis. The Fourier basis is mutually unbiased and can be defined relative to a computational basis where $m \in \{0, ..., d-1\}$: $|f_m\rangle = \frac{1}{\sqrt{d}} \sum_{n=0}^{d-1} \mathrm{e}^{-2\pi \mathrm{i} mn/d} |n\rangle$.

To put this in familiar context, consider the case of QKD. One can make measurements in the rectilinear basis (HV) by passing a state through a polarizing beam splitter. To make measurements in the DA basis, one can use a half-wave plate to rotate the state of polarization by 45° just prior to the polarizing beam splitter without making any further changes to the measurement apparatus. Similarly, to make a Fourier basis measurement in the frequency domain, one can apply a discrete Fourier transform (**DFT**) gate [30] followed by computational basis detection.

An important feature of measurements in MUBs is that the presence of strong correlations between two particles in both MUBs signifies the presence of entanglement in the system. In fact, this is the principle behind entanglement-based QKD. Only when Alice and Bob make measurements in the same basis are their individually random measurements highly correlated with one other. When Alice and Bob make measurements in different bases, their measurement outcomes are uncorrelated with one another and, consequently, these results are discarded. Baveresco *et al.* [72] recently established that measurements in two MUBs are sufficient to certify d-level entanglement. While the number of measurements required

↑The results of this section have been published in [71]

can depend on an astute guess for the state (a straightforward task with some knowledge of the source or the generation process), no further measurements in other bases are required.

Using a QFP, Lu *et al.* [30] recently synthesized a Hadamard gate (two-dimensional DFT) with just a single RF harmonic and a 3-dimensional DFT gate, or 3-DFT, with the addition of a second harmonic. In fact, the analysis summarized in **Fig. 3.9** shows that the number of harmonics needed to synthesize a d-DFT gate with high fidelity (> 0.999) and high success probability (> 0.95) is $d - 1$. However, the work by Lu *et al.* only considered weak coherent states and follow-on work [35] was limited to two-dimensional operations owing to incompatibility between the pulse shaper resolution (25 GHz) and the frequency of the highest synthesizable second RF harmonic (36 GHz).

2.4.1 High-Dimensional Entanglement Certification

We extend this work by pushing the limits of discrete components to construct a QFP driven with two RF harmonics (20 GHz and 40 GHz) that are multiples of pulse shaper resolution. Parallel 3-DFT gates operate on both halves of the three-dimensional frequency bin entangled state $\frac{1}{\sqrt{3}} \sum_{p=1}^{3} |p, -p\rangle_{\mathrm{SI}}$, which is prepared in a manner similar to that outlined in section 2.3. **Fig. 2.14** shows mode transformation spectra for the parallel 3-DFT operation.

Frequency correlation measurements in both the computational and Fourier bases (after parallel 3-DFT operations) are presented in **Fig. 2.15**. We prepare three of the Bell-type entangled qutrits ($\phi \in \{0, 2\pi/3, 4\pi/3\}$) as inputs to the QFP and observe strong correlations

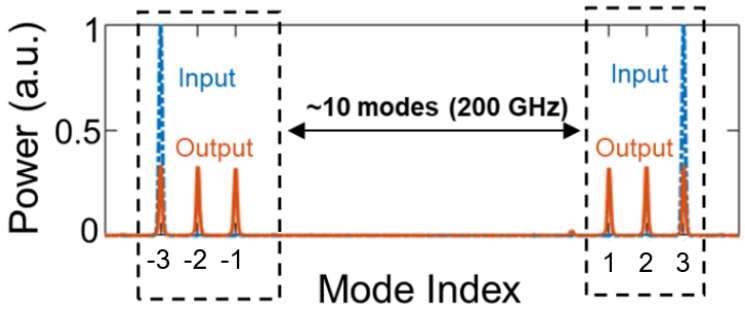

Figure 2.14. Mode transformation spectra from experiments with classical light. Two 3-DFT gates are separated by 200 GHz and operate on both halves of a three-dimensional frequency-bin-entangled state.

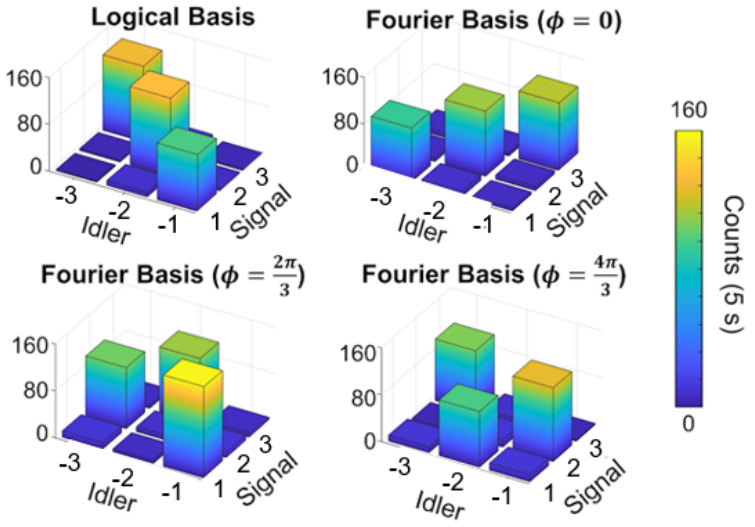

Figure 2.15. Measurements in the (a) computational (EOMs off) and (b) Fourier basis for a three-dimensional frequency-bin-entangled state. A pulse shaper used for state preparation produces biphoton states ideally of the form $|\psi\rangle \propto |3,-3\rangle_{SI} + e^{i\phi}|2,-2\rangle_{SI} + e^{2i\phi}|1,-1\rangle_{SI}$. Measurements in the Fourier basis correspond input states where $\phi \in \{0, 2\pi/3, 4\pi/3\}$

in both MUBs. The calculated mutual predictability [73] for all three states are 1.7696, 1.7714 and 1.7519, respectively. These values exceed the upper bound of $\frac{4}{3}$ for separable states in three-dimensional systems measured in two MUBs. One can also view these measurements as part of quantum state tomography and we utilize Bayesian machine learning methods [74] to calculate the mean and error bar of the state fidelity even though the number of measurements is tomographically incomplete. We infer state fidelities of 0.841 ± 0.019, 0.839 ± 0.017, and 0.825 ± 0.020, respectively, (as compared to the ideal high-dimensional Bell state) from these two measurements.

A point to note here is that state fidelity is not limited by gate performance. Instead, measurements suffered from intermodal crosstalk as the input state was prepared using a commercial Fourier transform pulse shaper with the mode separation (20 GHz) at the resolution limit of the pulse shaper ($\sim$ 20 GHz). In related work, which involved the synthesis of only two-dimensional gates, we find that use of a narrow linewidth etalon (FWHM $\sim$ 0.8 GHz) to carve the spectrum, instead of a Fourier transform pulse shaper, improves the discrimination accuracy of a Bell state analyzer from $> 92\%$ [75] to $> 98\%$ [76] despite the

need for a wider window for coincidence detection (128 ps vs. 1.5 ns). However, these results serve as validation that high-dimensional quantum gates can be leveraged in instances where there is a need for efficient entanglement certification and not full quantum state tomography.

3. MANIPULATING FREQUENCY-ENCODED QUANTUM INFORMATION

While developing tools and techniques to certify frequency-bin entanglement represents an important step, implementing even the most basic networking protocols requires more – elementary quantum gates. For example, in QKD users need to implement rotations between two mutually unbiased bases [3], while dense coding requires the ability to perform all Pauli gates [13], [77].

In the case of polarization-encoded photons, one can switch between the rectilinear (horizontal–vertical) and diagonal (diagonal–antidiagonal) bases using just a half-wave plate. In the frequency domain, the equivalent operation was until recently difficult to implement deterministically as it requires frequency bins be split, or scattered, between only two levels (in the case of qubits). This is in clear contrast to the comb-like spectrum generated by an EOM driven with single RF tone [**Fig. 2.10(a)**]. There is no standalone, commercially available component capable of implementing deterministic quantum frequency gates. This is one of the reasons why the frequency degree of freedom, despite all its advantages – stability in optical fiber, straightforward measurement with high-efficiency filters and detectors, and compatibility with wavelength-division multiplexing -– has received comparatively little attention until very recently [51].

QFP-based experiments, which are the subject of an ongoing collaboration between ORNL and Purdue University [30], [35], [36], have to date relied on discrete off-the-shelf telecommunications equipment. We complement this progress by exploring adjacent challenges –- the incorporation of frequency mixing techniques compatible with other degrees of freedom, like polarization state, and the migration of quantum functionality to an integrated photonic platform to lower optical losses, as well as expand the complexity of operations that can be realized with a QFP.

3.1 Frequency mode transformations with hyperentangled BFCs

Hyperentanglement, i.e., entanglement in more than one degree of freedom, can be a valuable resource for quantum communication and networking [80]. For example, it can be harnessed to implement high-capacity QKD, where nonclassical correlations are shared across multiple degrees of freedom and are used to generate a high-alphabet cryptographic key [81]. Hyperentanglement is also important in direct communication protocols, like dense coding, where entanglement in an ancillary degree of freedom can be used to distinguish between all four Bell states (in the encoding degree of freedom) with a single joint measurement using linear optics [13], [77].

Our investigation of hyperentanglement focuses on states entangled in frequency bin and polarization state. This interest in polarization is motivated by two factors. The first is that many, if not most, foundational experiments in quantum optics relied on polarization encodings [11]. Consequently, there exists both a well-established research community, as well as deployed infrastructure [82]–[87], that can be leveraged for communication and networking demonstrations. Secondly, polarization-entangled photon pairs are commonly generated by spontaneous nonlinear mixing processes such as parametric down conversion [88] and four-wave mixing [89]. These processes conserve energy and, consequently, photon pairs generated in this manner are also entangled in the time-frequency degree of freedom, thus making frequency encoding a natural choice to pair with encoding in polarization state.

A critical aspect to working with multiple degrees of freedom is ensuring that mode transformations in one degree of freedom do not degrade information or entanglement in another degree of freedom. For example, a combination of quarter- and half-wave plates can be used to implement arbitrary transformations of polarization state without affecting correlations in frequency. The same is not true of phase modulators, which are commonly used to implement frequency transformations. In the case of devices based on lithium niobate, the r_{33} electro-optic coefficient (aligned with [001]) is much stronger than those along other crystal directions [90]. Consequently, commercially available EOMs are designed to modulate the field along this direction, i.e., they act on only one component of the polarization state. To

↑The results of this section have been published in [78], [79]

overcome this limitation, we develop a polarization diversity scheme capable of implementing frequency mixing operations while preserving information and entanglement in polarization state.

3.1.1 Polarization diversity scheme for electro-optic phase modulation

Fig. 3.1(a) is an illustration of our polarization diversity scheme to achieve polarization-insensitive phase modulation. This polarization diversity phase modulator (**PDPM**) comprises two fiber-based polarizing beam splitters (**PBS**) and two EOMs. Light enters the PDPM through the PBS on the left and is split into two orthogonally-polarized compo-

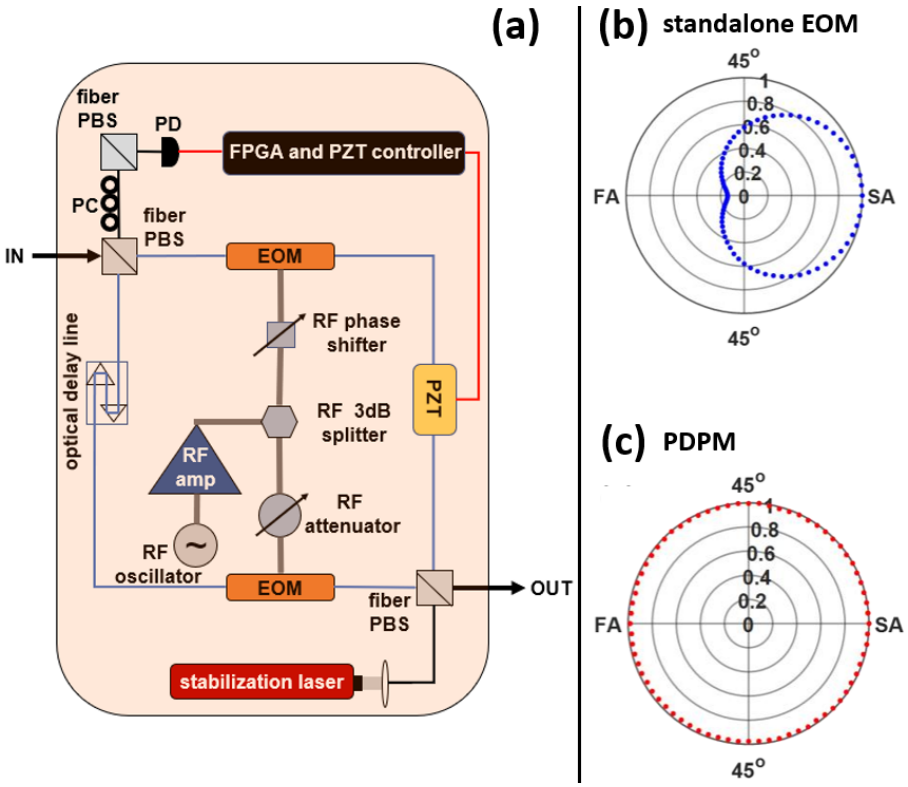

Figure 3.1. (a) Schematic of the polarization diversity phase modulator. PBS, polarizing beam splitter; RF, radio frequency; EOM, electro-optic phase modulator; PZT, piezoelectric phase shifter; FPGA, field-programmable gate array; CW laser, continuous-wave laser. Normalized optical power scattered into the +1 sideband, as a function of input polarization, for (b) a standalone EOM and (c) the PDPM. SA, slow axis of polarization-maintaining fiber; FA, fast axis of polarization-maintaining fiber.

nents that propagate along separate channels. Both channels of the device use polarization-maintaining (**PM**) fiber and light in each channel is modulated independently by one of two different EOMs. A second PBS recombines light from the two channels to return a phase modulated version of the arbitrarily polarized input signal. **Fig. 3.1(b) and (c)** show results from PDPM testing with classical light. The two plots show the amount of power scattered into the +1 sideband, as function of polarization state at the input, for both a standalone EOM and the PDPM.

In addition to polarization-insensitive phase modulation, compatibility with polarization entanglement requires a fixed phase relationship between the state of polarization entering the PDPM and the state of polarization exiting the PDPM. In other words, there needs to be a fixed path length difference between the arms of the device. In the absence of any active stabilization, we determined that the path length difference between the arms of the PDPM fluctuates over a 60 fs range. Consequently, the PDPM scrambles the polarization state of any photons, or photon pairs, that pass through it.

To minimize these fluctuations in the path length difference, a piezoelectric phase shifter (**PZT**) is included in one arm of the PDPM. Fluctuations in the path length difference were monitored by sending light from a CW laser through the PDPM in the backward direction. This light exits the input PBS through the top port [**Fig. 3.1(a)**] and is sampled by a polarizer oriented at 45° and sent to a photodiode. Based on the photodiode current, a field-programmable gate array controls the PZT to stabilize the path length difference between the arms of the PDPM.

3.1.2 PDPM characterization with quantum light

While the eventual goal is to implement frequency bin quantum gates that are insensitive to and do not (irreversibly) modify the input polarization state, elements capable of such frequency transformations, like QFPs [30] and coupled-cavity electro-optic modulators [91], are relatively recent developments. Therefore, we use measurements of two-dimensional frequency-bin entanglement (section 2.1) as a proxy for how more advanced elements might function when incorporated in a polarization diversity scheme. Our experimental setup is

illustrated in **Fig. 3.2**. Time-energy entangled photons are generated by SPDC in a PPLN ridge waveguide engineered for type-II phase matching. The crystal is pumped by a CW laser ($\lambda \sim 780$ nm). In order to generate photon pairs also entangled in polarization state, we tune the pump wavelength and the PPLN temperature to ensure (spectrally) degenerate down-conversion [92]. Temporal walk off between horizontally- and vertically-polarized components of the biphoton, which occurs both in the PPLN waveguide and the PM fiber-based output coupler, is compensated for with a 90° splice of PM fiber (to flip photons on the slow axis to the fast axis and vice versa) followed by a prescribed length of PM fiber (~ 63 cm, found by

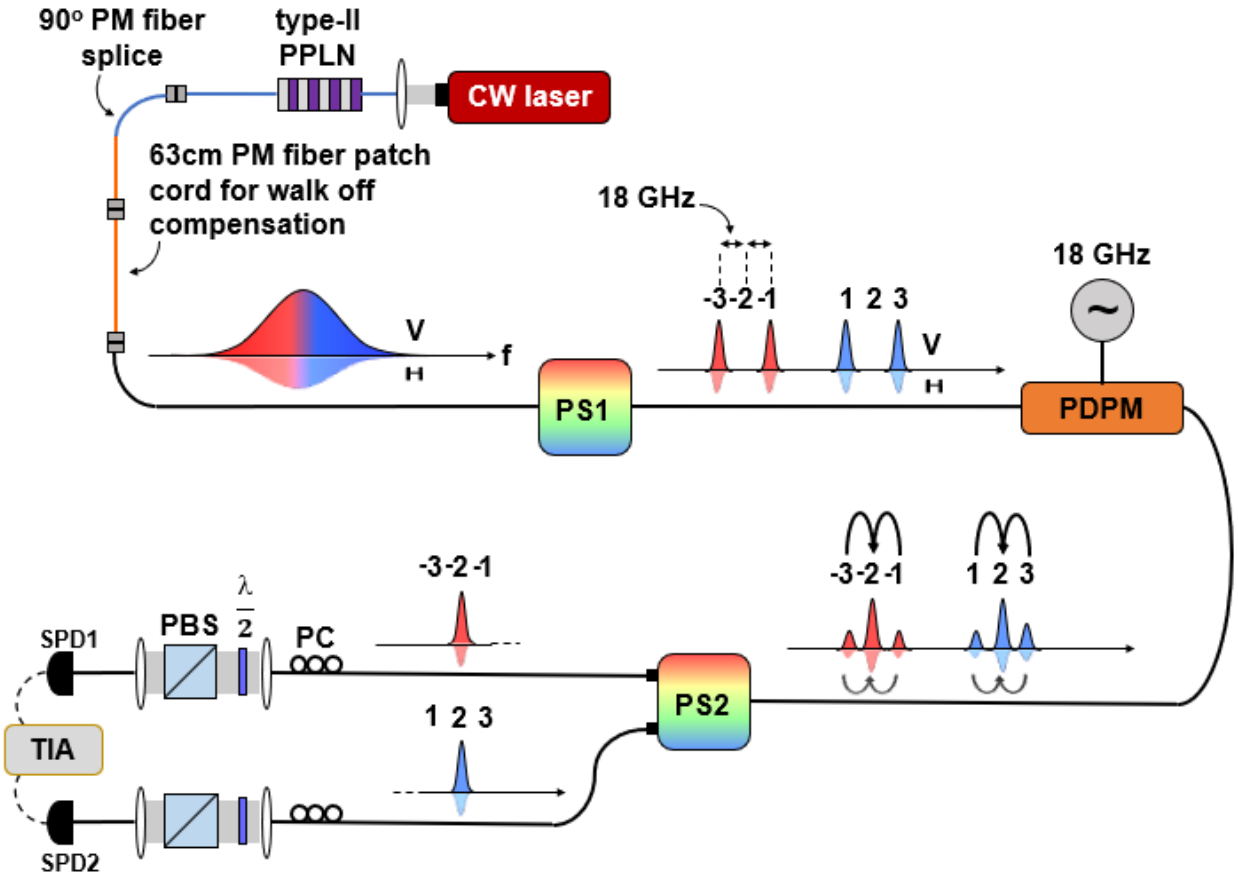

Figure 3.2. Experiment for generating and measuring frequency-bin entanglement in hyperentangled BFCs. CW laser, continuous-wave pump laser; PPLN, periodically-poled lithium niobate waveguide; PS, pulse shaper; PDPM, polarization diversity phase modulator; PC, polarization controller; $\lambda/2$, half-wave plate; PBS, polarizing beam splitter; SPD, single-photon detector; TIA, time interval analyzer.

the cutback method to optimize polarization entanglement). As a result, any two energy-matched frequency bins (-1 and 1 or -3 and 3) are also entangled in polarization state [**Fig. 2.6(c)**] and ideally in the form $|\Psi\rangle_{\text{spin}} \propto |HV\rangle_{SI} + e^{i\phi} |VH\rangle_{SI}$.

We use pulse shaper PS1 [**Fig. 3.2**] to project the biphoton onto state $|\Psi\rangle \propto \left(e^{i\phi_1} |1,-1\rangle_{SI} + |3,-3\rangle_{SI}\right) \otimes |\Psi\rangle_{spin}$ by passing bins -3, -1, 1, and 3 such that bins -1 and 1, as well as bins -3 and 3, are frequency-entangled. The separation between frequency bins populated by the signal, i.e., bins 1 and 3, is 36 GHz and likewise for frequency bins populated by idler. All frequency bins were programmed to have a 3 dB bandwidth of 12 GHz. To characterize frequency-bin entanglement for this state, we project comb line pairs $|1,-1\rangle_{SI}$ and $|3,-3\rangle_{SI}$, albeit probabilistically, into an indistinguishable superposition, i.e., onto state $|2,-2\rangle_{SI}$. The PDPM, whose arms are matched both in terms of optical path length and RF drive, performs this operation in a polarization-insensitive manner. By sweeping the joint phase on $|1,-1\rangle_{SI}$, we map the linear spectral phase ramp to a sinusoidal variation in the overall amplitude of superposition state $|2,-2\rangle_{SI}$ and, therefore, in the probability of detecting coincidences between the corresponding frequency bins.

3.1.3 Preservation of correlations in polarization state

To assess whether the PDPM can implement frequency-mixing operations while preserving correlations in polarization state, we equip the output ports of pulse shaper PS2 [**Fig. 3.2**] with polarization analysis modules (half-wave plate + polarizer). Two-photon interference traces to characterize frequency-bin entanglement were recorded for four signal–idler polarization settings – VH, HH, AD, and DD (H = horizontal, V = vertical, D = diagonal, A = antidiagonal). Polarization entanglement ensures strong correlations for certain polarization settings (VH and AD) and no correlations for others (HH and DD). The visibility of the interferograms in **Fig.3.3(a) and (c)** exceeds the classical threshold of $\frac{1}{\sqrt{2}}$ needed to violate a Bell inequality under the assumption of symmetric noise model [58], [59], thereby confirming frequency-bin entanglement in the biphoton state. Since we are only able to generate high-visibility and high-amplitude quantum interference in the frequency domain only for specific polarization settings, this strongly suggests that polarization en-

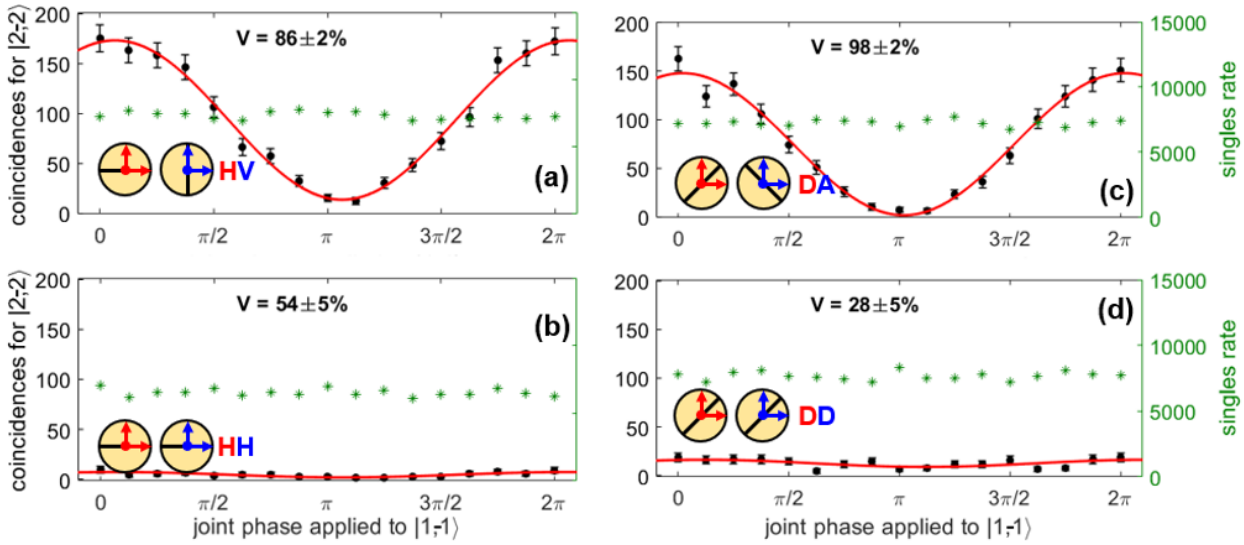

Figure 3.3. Two-photon interference traces showing the coincidence rate for superposition state $|2,-2\rangle_{\mathrm{SI}}$ as a function of the joint phase applied to $|1,-1\rangle_{\mathrm{SI}}$. Coincidences are acquired over 150 s and presented without background subtraction. Interferograms are shown for four signal–idler (blue–red) polarization settings – (a) vertical–horizontal; (b) horizontal–horizontal; (c) antidiagonal–diagonal; and (d) diagonal–diagonal. Insets show the relative orientation between each photon and polarizers in their respective polarization analysis modules.

tanglement is preserved after frequency-mixing by the PDPM. A natural next step is to use the PDPM to implement probabilistic qubit rotations in a dense coding scheme where hyperentanglement-assisted Bell state analysis [77] is used to discriminate all four frequency bin Bell states.

3.2 Integrated Quantum Frequency Processor

As noted earlier, one challenge of working with frequency-encoded quantum information is that there exists no standalone (and commercially available) component to implement *deterministic* logic gates with frequency qubits or qudits. EOMs (standalone or PDPM), when driven with a single RF tone, scatter an input frequency bin into a comb-like spectrum instead of into only two or d frequency bins, as required for deterministic qubit or qudit operations, respectively.

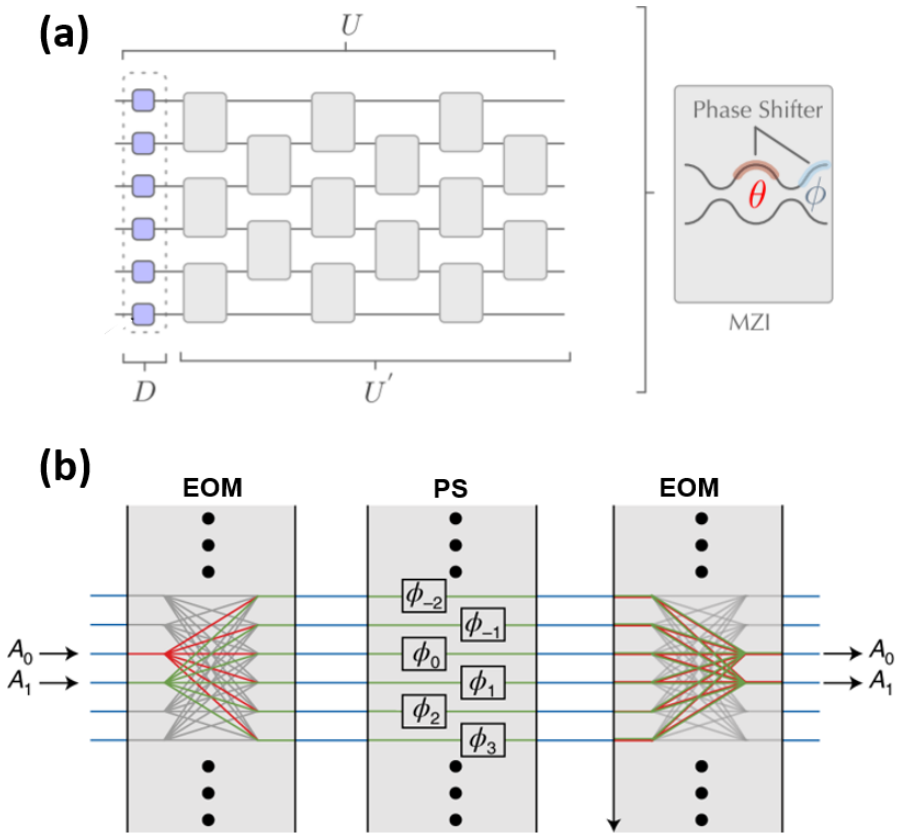

Figure 3.4. (a) Programmable unitary network (U) where interference between waveguide paths is mediated by Mach-Zehnder interferometers and phase shifters. Source: Ref. [93]. (b) Quantum frequency processor depicting multimode interference in the spectral domain. EOM, electro-optic phase modulator; PS, pulse shaper. Source: Ref. [51]

The QFP paradigm [32] overcomes this limitation by harnessing multimode interference in the spectral domain to realize deterministic frequency mode transformations and, therefore, deterministic logic gates for frequency-encoded quantum information. It is instructive to consider the analogous implementation based on coupled waveguide arrays [**Fig. 3.4(a)**]. In so-called path-encoded schemes, N input waveguides, or paths, are coupled to one another through a network of 2×2 tunable beam splitters (Mach-Zehnder interferomters, to be precise) and phase shifters. With $\frac{N(N-1)}{2}$ unit cells, where each cell comprises a 2×2 tunable beam splitter and a phase shifer, these systems can implement arbitrary transformations between N input paths and N output paths.

In the spectral domain, EOMs and Fourier transform pulse shapers take the place of 2×2 tunable beam splitters and phase shifters, respectively. Consequently, with a concatenation of EOMs and pulse shapers, one can realize any arbitrary frequency mode transformation in a theoretically scalable fashion. However, there is a critical difference between path–based programmable unitaries [**Fig. 3.4(a)**] and the QFP protocol. Unlike 2×2 beam splitters and phase shifters, EOMs and pulse shapers operate on a multitude of modes simultaneously and not just on one or two at a time [**Fig. 3.4(b)**]. Consequently, the number of resources required to implement N-dimensional operations scales, to first order, as $\mathcal{O}(N)$ instead of as $\mathcal{O}(N^2)$ [32]. It is worth noting that resources (free parameters, technically) refers not only to concatenations of EOMs and pulse shapers, but also to the number of RF harmonics used to drive the EOMs.

3.2.1 Background

The QFP paradigm for discrete variable frequency encoding offers three compelling advantages. The first is that it admits *massive parallelization of quantum operations in a single spatial mode* [30] [**Fig. 3.5**]. Secondly, this architecture relies on high-speed electro-optic modulation and, therefore, has the potential to permit *fast reconfiguration of quantum gates*. Lastly, the frequency degree of freedom supports multilevel quantum information (qudits), opening the door to *high-dimensional encodings* that are compatible with multiplexing in the spectral domain, stable over single mode fiber, and able to leverage deployed fiber-optic infrastructure.

Demonstrations to date [30], [35], [36] have relied on discrete components. While these components offer the reliability one comes to expect of commercially available telecommunications equipment, they introduce relatively high optical losses. Typical insertion losses for EOMs and Fourier transform pulse shapers are on the order of $3-4$ dB and $4-5$ dB, respectively. In other words, the insertion loss of a three-element QFP (EOM – pulse shaper – EOM) constructed from discrete components will be at least 10 dB. If this loss is experienced by both photons participating in a joint measurement, this results in at least a 20 dB drop in the two-photon event rate.

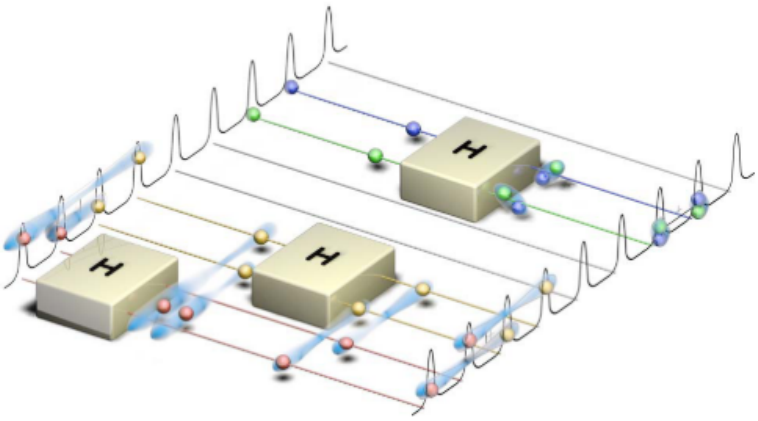

Figure 3.5. High-level illustration of parallel quantum operations implemented in single quantum frequency processor across many spectral channels. Source: Ref. [35]

Another limitation imposed by discrete components is that adjacent frequency modes need to be separated by at least 20 GHz – set by the resolution of commercial pulse shapers – in order to avoid intermodal crosstalk. Consequently, if one wants to efficiently mix even just adjacent modes, EOMs need to be driven with at least a 20 GHz RF tone. However, to connect more distant modes, a requirement to synthesize high-dimensional quantum gates with a QFP, one needs access to not just to a 20 GHz tone but also to higher RF harmonics. For example, to permit the full range of two-dimensional quantum operations with both high fidelity ($\mathcal{F} > 0.9999$) and high success probability ($\mathcal{P} > 0.95$) using just two EOMs and a pulse shaper, the RF drive needs to include at least two harmonics [35]. Similar behavior holds for higher dimensions as well. This interplay between the EOM bandwidth (BW_{RF}) and the separation between adjacent modes ($\Delta f_{\text{optical mode}}$) is a rough gauge of gate complexity supported by a QFP. To first order, the ratio $\frac{BW_{\mathrm{RF}}}{\Delta f_{\text{optical mode}}}$ corresponds to the highest dimensional gate set one can synthesize using a three-element QFP. Consequently, even with a generous RF bandwidth of 60 GHz, which is close to the upper limit of what one can do with commercially available components, one is limited to just 3-dimensional gates owing to the 20 GHz pulse shaper resolution.

For these reasons, realizing the full potential of quantum information processing in the frequency domain will require the migration of functionality to an integrated optical platform.

In addition to a reduction in optical loss, integrated photonics will enable more complex operations, either by increasing the number of RF harmonics accessible to the system or by permitting realization of QFPs that comprise concatenations of additional pulse shaper and modulator elements. Such a system would be well-suited to address the following near-term challenges in quantum information science:

1. High-dimensional encoding for information transport more robust to loss [94],
2. Photon-photon interconnects compatible with frequency mismatch [75], and
3. Agile any-to-any wavelength hopping for in-band quantum frequency conversion without pump fields [50].

3.2.2 Technical Approach

As was just noted, the complexity of QFP operations can be increased in one of two ways –- (a) increasing the number of elements (EOMs and pulse shapers) concatenated, and (b) increasing the number of RF harmonics (multiples of the fundamental mode spacing) accessible to the QFP. While there is potential to reduce on-chip losses sufficiently that a 5- or 7-element QFP can provide acceptable performance, this route also presents challenges from standpoint of electronic-photonic integration as one needs to deliver control signals to multiple spectral channels across multiple pulse shapers.

A more practical approach to increasing gate complexity in a QFP is by increasing the number of RF harmonics accessible to the system. This does not require adding more physical blocks or elements and is a scaling advantage unique to the QFP. While discrete components limit any QFP implementation to at least a 20 GHz separation between adjacent modes, one can leverage integrated photonics to increase the number of RF harmonics accessible to the system by decreasing this minimum separation between frequency modes [**Fig. 3.6**]. Spectral filters with sub-GHz linewidths and low drop port loss have recently been demonstrated using commercial foundries [95], suggesting that pulse shapers based on banks of add-drop filters [96], [97] can support channel separations on the order of $2-4$ GHz. This would, in principle, permit access to $6-12$ RF harmonics using commercially available arbitrary

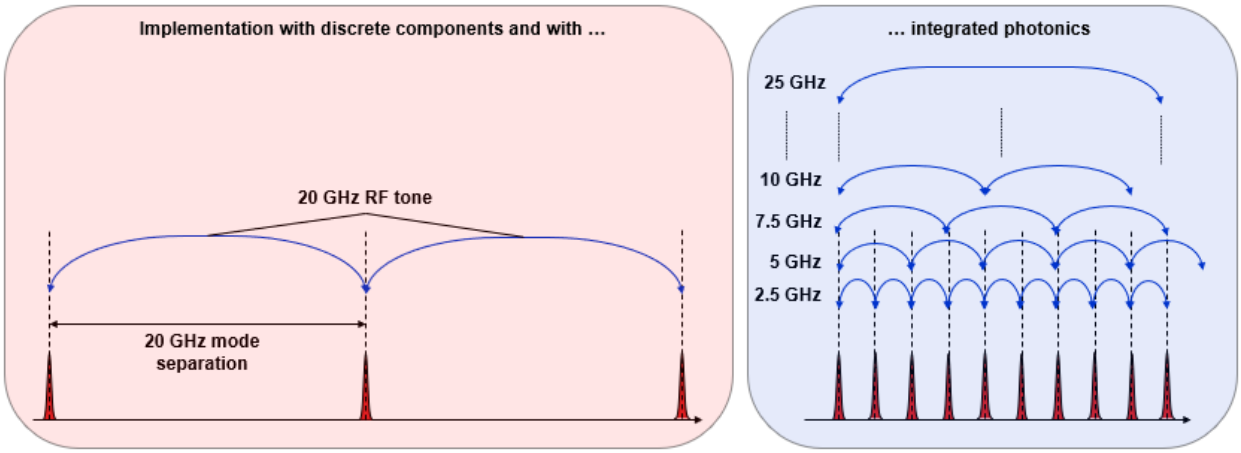

Figure 3.6. Limitations on frequency mode separation for a QFP implementated with discrete components (*left*) compared to one implemented in integrated photonics (*right*). The illustration highlights their impact on the number of RF tones accessible to a QFP.

waveform or bit sequence generators (25 GHz analog bandwidth). Consequently, rather than simply enhancing SWaP metrics, photonic integration will enable *fundamentally new quantum functionality*.

With regard to material platform, no one choice stands out above the rest. Low waveguiding loss is critical to realizing the narrow linewidth filters required of the pulse shaper, while the presence of a strong $\chi^{(2)}$ optical nonlinearity is critical to efficient modulation of the guided optical mode in EOMs. Narrow linewidth filtering, or the potential to support narrow linewidth filtering, has been demonstrated in silicon [95], silicon nitride [98], and thin-film lithium niobate [99]. Of these, only thin-film lithium niobate supports a $\chi^{(2)}$ nonlinearity, making it the only option to realize a monolithic QFP.

However, decades of semiconductor R&D investment has motivated efforts to either improve silicon modulators based on free carrier dispersion [100] or introduce an optical nonlinearity through hybrid geometries [101]–[103] or heterogeneous integration [104]. One approach in particular, which is based on incorporation of organic electro-optic material (**OEO**), shows particular promise for quantum applications [101], [105]. Although so-called silicon-organic hybrid (**SOH**) modulators have fallen out of favor for classical applications owing to photo-induced degradation of OEO material [106], this is not a concern at the

EOM device geometry / material platform	$\alpha V_\pi L$ (VdB)	α^* (dB)	L^* (mm)	High-volume foundry process?
Silicon (Si, plasma dispersion)	5.8	1.6	1.3	Yes
Si-LN hybrid	4	1.3	20.3	Yes
Si-graphene (Si-SLG)	62	18.8	0.8	Yes
Thin-film lithium niobate (TFLN)	0.5	0.17	7.3	No
Silicon-organic hybrid (SOH)	1.0	0.34	0.14	Yes

* - optical loss and device length for CMOS logic level (3.3V) to introduce a π phase shift

Figure 3.7. Comparison of modulators in references [102], [103], [105], [107].

single-photon level. In addition to allowing one to leverage the maturity of silicon photonics, SOH modulators support higher modulation efficiencies [101], [105] than thin-film lithium niobate (**TFLN**) as partly evidenced by their voltage-length products of $0.03 - 0.04$ V·cm – a value over 65× lower than even the best result with thin-film lithium niobate [107].

While this number is certainly impressive, a fair comparison should account for the fact that SOH modulators are based on a slot waveguide geometry, which maximizes field overlap (between the optical mode and the driving RF waveform) at the expense of optical loss. A good figure of merit against which to compare modulators with different geometries is the voltage-loss product ($\alpha V_\pi L$), a metric that is independent of device length and commonly expressed in units of V·dB. Quite simply, this number represents insertion loss of a device that is scaled to introduce a π phase shift at a bias of 1V, i.e., its half-wave voltage (V_π) is 1V. A summary of the best performing devices for the platforms cited above is presented in **Fig. 3.7**. In terms of the voltage-loss product, SOH and TFLN modulators stand apart. While TFLN modulators offer better performance in terms of optical loss, SOH modulators have significant advantages in terms of device footprint and foundry-scale production.

In sum, our design for an integrated quantum frequency processor will address the challenge of optical loss through the development of short ($\sim 100\mu$m-long) SOH modulators and limitations on gate complexity through the development of pulse shapers that can address individual channels separated by $2 - 4$ GHz.

3.2.3 System Design and Modeling

Pulse shaper

Fourier transform pulse shapers [33], [34] can be realized in integrated optical platforms through banks of add-drop filters [96], [97], [108]. In the most straightforward conception [**Fig. 3.8**], an individual channel in an integrated pulse shaper includes a microring filter to "download" a target frequency mode (λ_1) from an input bus waveguide that carries a broadband optical signal. This is followed by a (thermo-optic) phase shifting element to introduce the prescribed phase shift and a microring filter to "upload" the phase-shifted frequency mode (λ_1) onto an output bus waveguide. By building many such channels in parallel, each operating at a different center wavelengths ($\lambda_2, \lambda_3, \lambda_4 ... \lambda_N$), one can implement a Fourier transform pulse shaper in integrated photonics.

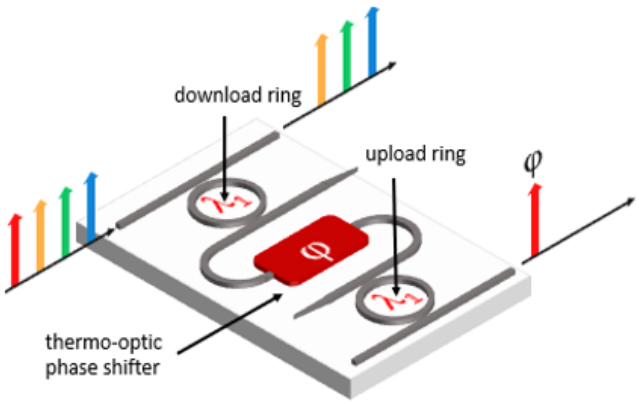

Figure 3.8. A single pulse shaper channel comprising a "download" filter to pick off a frequency mode at wavelength λ_1, a thermo-optic phase shifter to introduce the prescribed phase shift, and an "upload" filter to load the phase-shifted frequency mode onto a common output bus waveguide.

One limitation of filters based on a single optical microresonator (ring or racetrack geometry) is that their spectral response is characterized by a Lorentzian lineshape [109], [110] in contrast to the box-like filter response that one would prefer in an ideal system. Coupled microresonators can approximate this box-like response [108]–[110], but at the cost of added system complexity as each microresonator in a filter requires independent electrical drive (for wavelength trimming).

For the geometry in **Fig. 3.8**, each pulse shaper channel requires three independent drive lines – two for the microring filters and one for the phase shifting element. All the ground lines can be collected at a common plane, thus requiring 4 electrical lines per pulse shaper channel. If control electronics support addressing 96 channels, which represents an aggressive but reasonable target for integrated photonic microsystems, one is limited to control over 24 pulse shaper channels. Filters based on coupled microresonators, i.e., higher order filters, will require at least two additional lines for electrical drive per channel. In the case of second order filters (two coupled microresonators per filter), that would reduce the number of pulse shaper channels in the system to 16. That number in the case of third order filters is 12. Consequently, there is a tradeoff between achieving a box-like filter response and the number of pulse shaper channels one can address with a fixed number of electrical drive lines.

To gauge the impact of pulse shaper channel count on QFP gate performance, we run through a numerical optimization routine to identify the number of independent modes that need to be addressed to support a d-dimensional discrete Fourier transform (DFT) gate [32], [111] [**Fig. 3.9**]. Each d-dimensional DFT gate is presumed to have access to

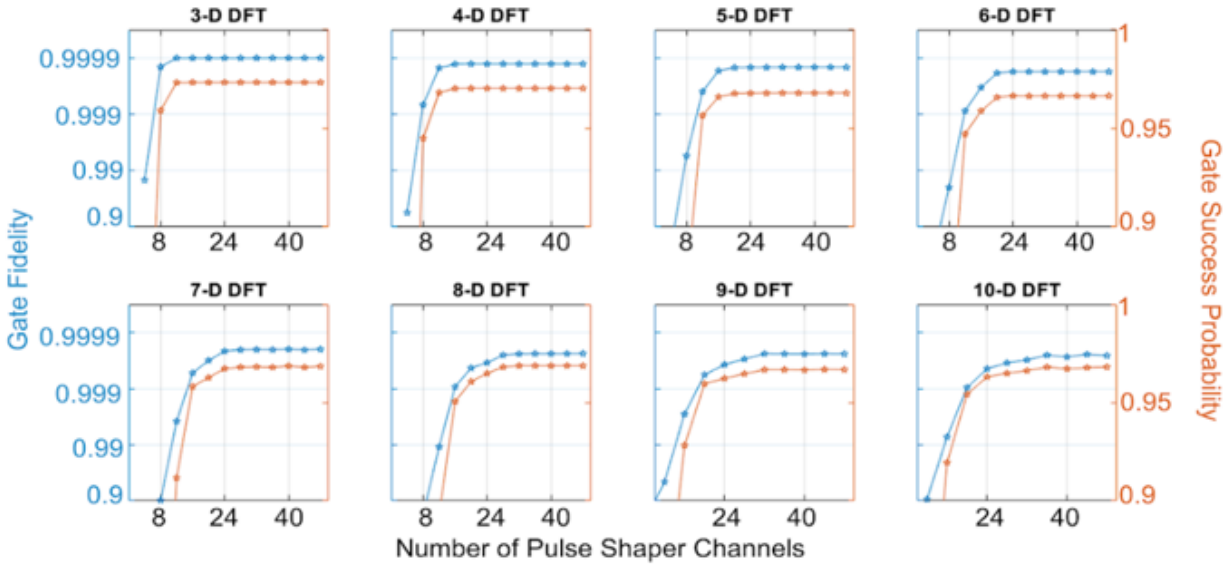

Figure 3.9. Numerical simulation of high-dimensional discrete Fourier transform (DFT) gates showing fidelity and success probability as a function of the number of addressed modes, i.e, the number of pulse shaper channels. For each d-dimensional DFT gate, the QFP can access $(d-1)$ RF harmonics.

$(d-1)$ RF harmonics. As noted earlier, with a target mode separation of $2-4$ GHz and an analog bandwidth of 25 GHz, an integrated QFP will have the 9+ RF harmonics needed to implement a 10-dimensional DFT gate. To realize this gate with both high fidelity ($\mathcal{F} > 0.999$) and high success probability ($\mathcal{P} > 0.95$), the pulse shaper in a three-element QFP will need to address 24 frequency modes. A 10-dimensional DFT gate represents a significant leap over anything achieved not only in frequency, but also in other degrees of freedom [**Fig. 1.1**]. The need for 24 addressable modes effectively determines the pulse shaper channel geometry for our three-element QFP – a thermo-optic phase shifter between two first order microresonator-based filters.

The Lorentzian lineshape of filters in the pulse shaper impose a penalty on QFP performance. Two effects are of particular concern – added optical loss from clipping of the input mode and crosstalk between adjacent channels. **Fig. 3.10(a)** shows the spectral re-

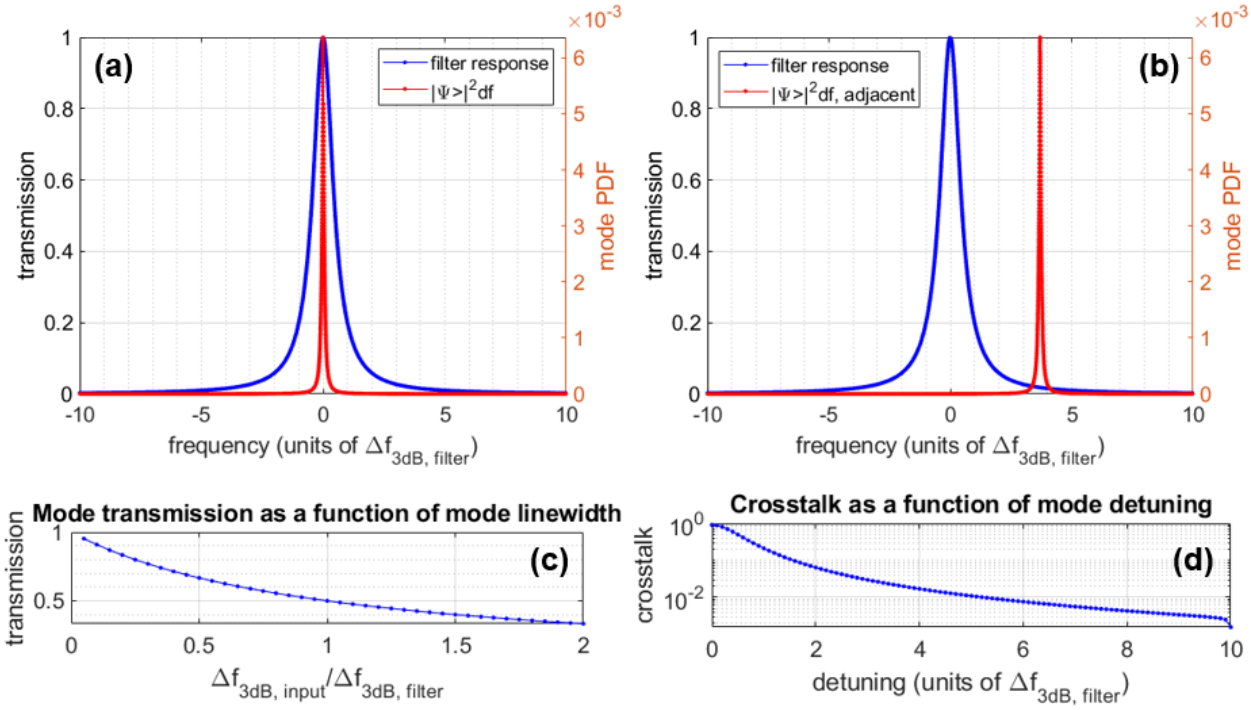

Figure 3.10. Plots show the overlap between the spectral response of a pulse shaping filter element (blue) and an input mode (red). (a), (c) consider the effect of filter lineshape on the transmission of a selected input mode. (b), (d) consider the effect of filter lineshape on crosstalk from an undesired/unselected mode.

sponse of a filter based on a single microresonator (blue) and the power spectral density of a hypothetical input mode (red), where $\Delta f_{\text{input}} = 0.1\Delta f_{\text{filter}}$. We assume that the input mode has a Lorentzian lineshape as well, a reasonable assumption given the use of optical microresonators to generate frequency bin-entangled photon pairs [48], [49]. For this ratio of mode linewidth (Δf_{input}) to filter bandwidth (Δf_{filter}), i.e., $\frac{\Delta f_{\text{input}}}{\Delta f_{\text{filter}}}$, 91% of the power in the input mode exits the drop port of the filter. This represents an *additional* 0.4 dB loss over any non-unity drop port transmission. **Fig. 3.10(c)** shows the effect of this additional loss as a function of $\frac{\Delta f_{\text{input}}}{\Delta f_{\text{filter}}}$. The narrower the linewidth of the optical mode relative to the filter, the greater the fraction of power passed by filter. From a practical standpoint, a ratio

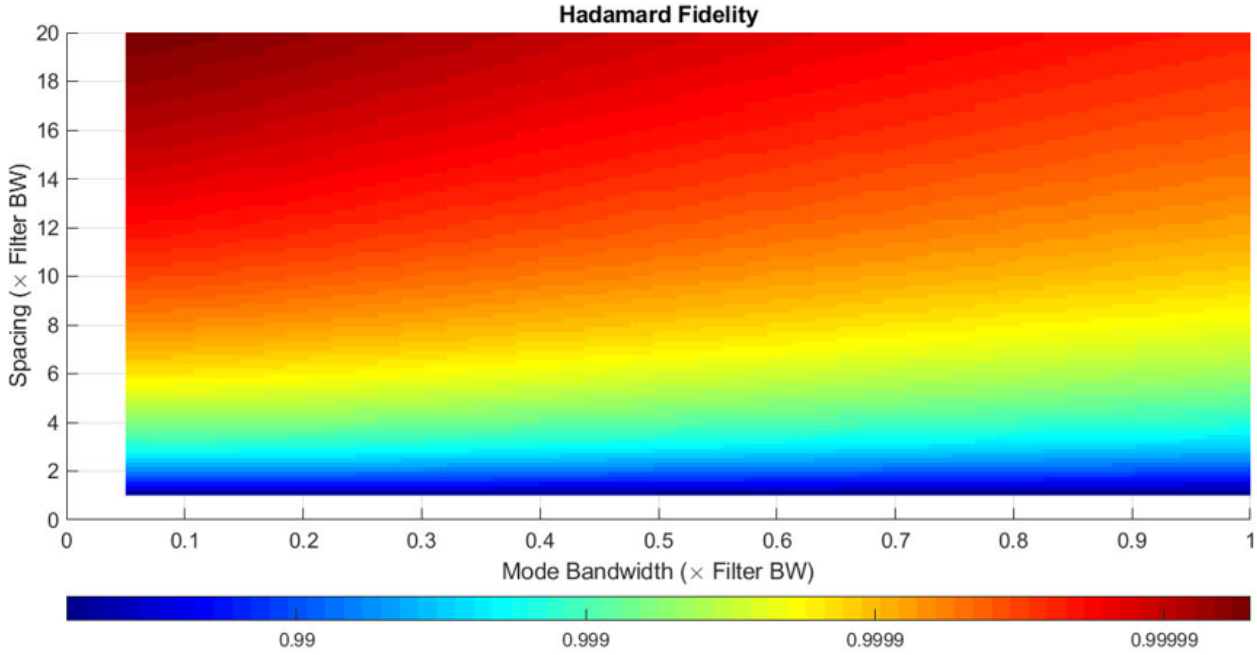

Figure 3.11. Heat map showing the transformation fidelity of a Hadamard gate implemented on a three-element quantum frequency processor. The quantum frequency processor comprises ideal modulators (index modulation linear with applied voltage) but includes a pulse shaper based on add-drop filtering with single microresonators. Transformation fidelity is plotted as a function of separation between adjacent frequency modes ("Spacing", y-axis) and the linewidth of frequency modes ("Mode Bandwidth", x-axis). Both the mode separation and mode linewidth are presented relative to the filter bandwidth ("Filter BW").

of 0.1 between the mode linewidth and filter bandwidth aligns with source (mode linewidth < 200 MHz) and device parameters (filter bandwidth $< 2 - 4$ GHz) under consideration.

An example of crosstalk from an undesired mode is plotted in **Fig 3.10(b)**. For a detuning of $3.7\Delta f_{\text{filter}}$ between the the filter and the input mode, 2% of the power from this undesired mode is captured by the drop port of the filter. **Fig. 3.10(d)** plots this crosstalk as a function of the detuning between the mode and the filter (under the assumption $\frac{\Delta f_{\text{input}}}{\Delta f_{\text{filter}}} = 0.1$). To limit power from adjacent modes to 2% or less, the separation between frequency modes needs to be greater than $3.7\Delta f_{\text{filter}}$. For crosstalk on the order of 1% and 0.5%, the separation between frequency modes needs to be at least $5.2\Delta f_{\text{filter}}$ and $7.4\Delta f_{\text{filter}}$, respectively. Conversely, one could view this criterion as setting an upper limit on filter bandwidth for a particular mode separation and specified level of crosstalk.

We quantify the effect of non-ideal filter response on system performance by modeling the transformation fidelity of a Hadamard gate implemented on a QFP featuring such a pulse shaper. Results from simulation are presented in **Fig. 3.11**. This model shows that transformation fidelity exceeds 0.999 when the separation between frequency modes is at least 4× the filter bandwidth assuming $\frac{\Delta f_{\text{input}}}{\Delta f_{\text{filter}}}$ value of 0.1.

Electro-Optic Modulator

The basic geometry of a silicon-organic hybrid (SOH) modulator is presented in **Fig. 3.12**. The slot waveguide is formed by two silicon rails ($w_{\text{rail}} \times h_{\text{rail}}$) that are separated by a narrow slot (w_{slot}). The slot, as well as the area surrounding silicon rails is filled with an organic electro-optic (OEO) material. The silicon rails are lightly doped and connected to metal transmission lines through doped silicon slabs ($w_{\text{slab}} \times h_{\text{slab}}$). As all elements - from the metal transmissions lines down to the lightly doped silicon rails - are conductive, most of the applied voltage drops across the OEO-filled slot (w_{slot}). Confinement of the optical mode in the slot results in strong overlap between the modulating radiofrequency field (E_{RF}) and the electric field of the guided optical mode (E_{OPT}).

The obvious drawback to bringing conductive material so close to the optical mode is that the geometry results in high optical loss *per unit length*. However, this optical loss is

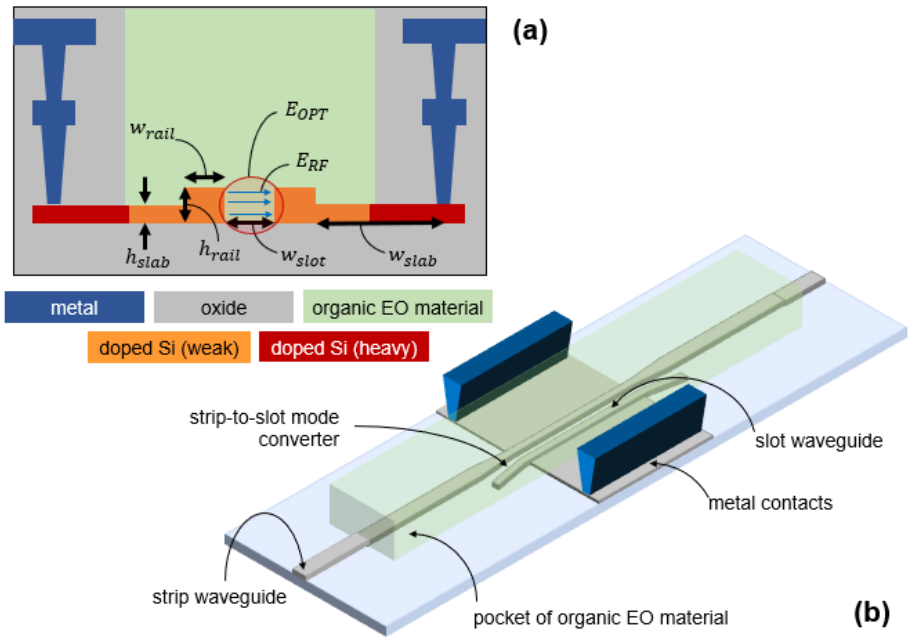

Figure 3.12. (a) Cross section of the slot waveguide in a silicon-organic hybrid modulator showing all relevant dimensions and layers. (b) Perspective view showing essential modulator components.

compensated for by two factors – (a) high overlap between the RF (E_{RF}) and optical fields (E_{OPT}), and (b) the ultra-high in-device electro-optic (EO) coefficient of state-of-the art OEO material [101].

Organic Electro-Optic (OEO) Material: High-performance OEO material used in plasmonic-organic hybrid [112], [113] (**POH**) and SOH modulators typically consists of chromophores with a large molecular hyperpolarizability that are functionalized with pendant groups and may also be blended with an inactive polymer matrix in order to form a solution-processible material [114]–[116]. Unlike crystalline EO materials such as lithium niobate, where a specific cut of the crystalline orientation is required to achieve alignment between RF and optical fields for maximum EO effect, OEO materials achieve molecular alignment through a one-time electric field poling process [101]. The chip is heated close to the glass transition temperature and a DC poling voltage is applied across the electrodes to align the dipolar chromophores. The acentric ordering is frozen by cooling the device to room temperature while maintaining the DC poling field.

The best performing, foundry-compatible SOH modulators have relied on the chromophore JRD1 [101], [105]. One reason for its high performance is that it can be used in high number densities without a polymer host and avoids centrosymmetric pairing of chromophores. As result of this high dipole density, bulk values for ($n^3 r_{33}$) in excess of 3850 pm/V have been measured [101].

Waveguide Geometry: **Fig. 3.12(b)** is a perspective illustration of the SOH modulator. A 480 nm-wide silicon strip waveguide transitions from an oxide-cladded region to a trench opened in the oxide cladding. The trench, or pocket, is filled with the chromophore JRD1. A strip-to-slot mode converter transitions the guided mode to the slot waveguide. Following propagation through the slot waveguide, a second mode converter transitions the mode back to a strip waveguide for routing across the rest of the chip. There is a discontinuity in the cladding index at the oxide-trench interface, which is a potential source of back reflections. However, mode overlap simulations indicate that such back reflections will be less than 1%.

A cross section of the slot waveguide is shown in **Fig. 3.12(a)**. Many of the parameters are fixed by the foundry –- slab height (h_{slab}), rail height (h_{rail}), and the metal electrode separation (set by the width of the trench containing OEO material). Of the parameters at our discretion, the slot width (w_{slot}) has been the subject of extensive work in both SOH [101], [105], [106], [117], [118] and POH, i.e., plasmonic-organic hybrid devices [116] with tradeoffs identified and in some cases well quantified [116]. These trade-offs are best understood by considering the general expression for the half-wave voltage (V_π) of an electro-optic phase modulator:

$$V_\pi L = \frac{\lambda d}{2\Gamma n^3 r_{33}} \tag{3.1}$$

In the case of a slot waveguide-based SOH modulator, d corresponds to the width of the slot (w_{slot}) and Γ to an integral that captures two critical effects – (a) the confinement of the optical mode in the slot and (b) the overlap between the electric fields of the optical mode (E_{OPT}) and the driving RF waveform (E_{RF}). n^3 and r_{33} refer to the refractive index

(cubed) and the effective EO coefficient of OEO material after a one-time electric field poling process [101], respectively.

All else being equal, a reduction in w_{slot} (d) results in a decrease in the half-wave voltage as the voltage is dropped over a shorter length ($E_{\text{RF}} = V_{\text{RF}} w_{\text{slot}}$). The shorter slot width also results in an increase in the overlap between the electric field of the guided optical mode and the driving RF waveform (see Supplementary Material in Ref. [101]), which further serves to reduce the half-wave voltage.

One expects that $n^3 r_{33}$ would be independent of slot width. This is true in the sense that after the one-time DC poling process, where the acentric ordering of dipolar chromophores are frozen in place, $n^3 r_{33}$ is fixed. However, this value depends critically on the particulars of the poling process. Ref. [101] investigated the performance of two SOH modulator variants with the only difference between them being their slot widths. The device with the larger slot width (190 nm) supported higher values of (in-device) $n^3 r_{33}$ because a smaller fraction of chromophores are immobilized due to adhesion to the silicon sidewalls in the slot. However, this improvement in $n^3 r_{33}$ was compensated for by an increase in the field overlap ($E_{\text{RF}} \cdot E_{\text{OPT}}$), as well as a reduction in slot width, in devices with a 150 nm-wide slot. *Consequently, both devices ultimately achieved the same modulation efficiency (*$V_\pi L$*).*

This certainly does not suggest that the SOH device performance is independent of slot width. Instead, 150 nm to 190 nm represents a optimal range for high-performance devices. Earlier work investigated precisely this dynamic – the effect of slot width on different figures of merit, albeit for POH modulators [116]. While the materials and length scales are different for SOH and POH devices, the fundamental tradeoffs are similar. What this work found was that if one moves from wide slot widths to narrower slot widths, $V_\pi L$ decreases up to a point and starts to pick up again. This inflection point occurs for slot widths of around 60 nm in POH devices and, from our survey of SOH literature [101], [105], [106], [117], [118], at around 150 nm in SOH devices.

This discussion of modulation efficiency obscures the fact that our design target, at least for quantum applications, is not high modulation efficiency. However, high modulation efficiency permits large phase swings with shorter device lengths, which in turn permits lower

optical loss. Consequently, a choice of slot width between 150 nm and 200 nm should ensure optimal loss performance.

One parameter not set by the foundry is the rail width (w_{rail}). **Fig. 3.13** shows data from simulations of SOH modulators with different slot widths (150 nm and 200 nm). The optical power confined to different device segments – slot, rails, and slab – are plotted together on this graph. A rail width of 215 nm (220 nm) for the 150 nm-wide (200 nm-wide) slot waveguide results in maximum confinement of the optical mode to the slot.

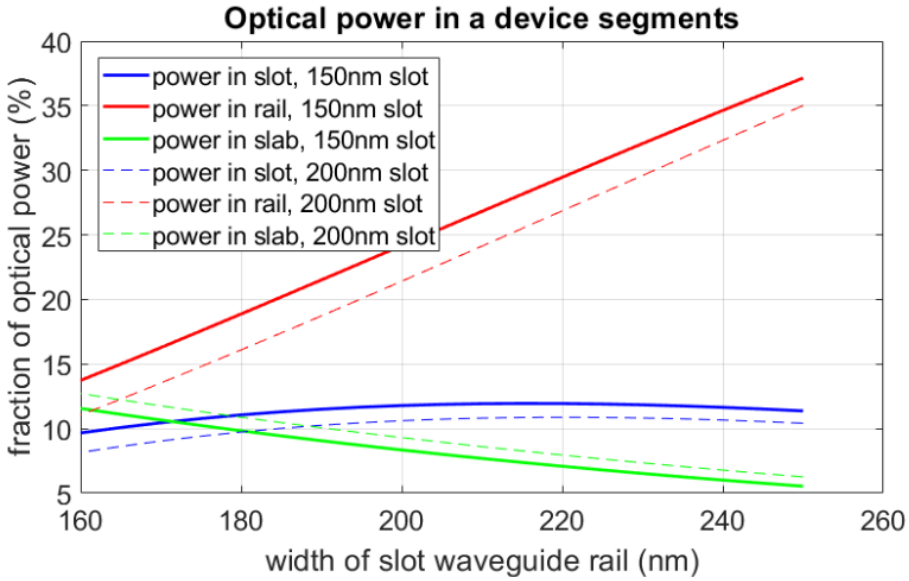

Figure 3.13. Data from simulations showing the effect of rail width on optical power confined in the slot, rail, and slab of the SOH modulator. Data for two different device geometries are included – a 150 nm-wide slot waveguide and a 200 nm-wide slot waveguide.

It is worth noting that as more power is confined to the rails and the slab, optical loss increase as these device segments consist of doped silicon. Consequently, without additional information it is not clear that maximizing the optical power confined to the slot of the waveguide will result in optimal performance, i.e., low loss per unit phase swing. However, ref. [118] isolated different contributions to device loss and found that a significant fraction of optical loss is the result of scattering at the sidewalls in the slot. Consequently, an attempt to minimize optical power confined in doped silicon will only affect a minor contributor to

device loss while also reducing an important factor that contributes to increased modulation efficiency – confinement of the optical mode in the slot.

Electrode Geometry: An advantage of slot waveguide SOH modulators, from a design point of view, is that their electrode geometry is very similar to that in depletion mode $p-n$ junction silicon modulators, which are based on free carrier dispersion and have been extensively studied [119]. The electrical drive signal is applied across metal transmission lines, which can be modeled by a series resistance (R_{TL}), a series inductance (L_{TL}), and a shunt capacitance (C_{TL}). For practical doping concentrations, the conductivity of the doped silicon slab is much smaller than the conductivity of the metal transmission line. Consequently, electrical currents in the direction of propagation are confined to the metal transmission line. The currents in the doped silicon slab flow predominantly in the transverse direction, i.e., currents flow between the metal and the slot. This understanding tracks with work reported in ref. [120]. Therefore, the effect of the slot waveguide, which comprises rails and slabs made of doped silicon, can be accounted for by adding a shunt resistance in the equivalent circuit. Finally, experiments have confirmed that negligible currents flow through OEO material in the slot, i.e., it behaves like a dielectric and can be modeled as a capacitance. In other words, the effect of the slot waveguide is to add a RC shunt to the circuit that describes the metal transmission line [**Fig. 3.14**].

The treatment in ref. [120] is directed to SOH devices and it focuses on phase-matched transmissions lines with long (mm-scale) interactions lengths. While this treatment is apt for depletion mode $p-n$ junction silicon modulators, it is less so for SOH devices based on materials available today. In particular, there has been tremendous progress in the synthesis of OEO materials with ultra-high efficiencies [115], as well as in realizing high values of in-device $n^3 r_{33}$ [101]. This progress has made it possible to reduce interaction lengths below 1 mm [105]. For this reason, Zwickel *et al.* [118] adapted the framework in ref. [120] to focus on the bandwidth- and loss-limiting effects of doped silicon waveguiding element, i.e., the RC shunt.

We now provide a qualitative description of the electrode geometry before moving on to the proposed design. When a DC electrical signal is applied to the metal transmission lines, the voltage predominantly drops across the slot, which is filled with OEO material. This

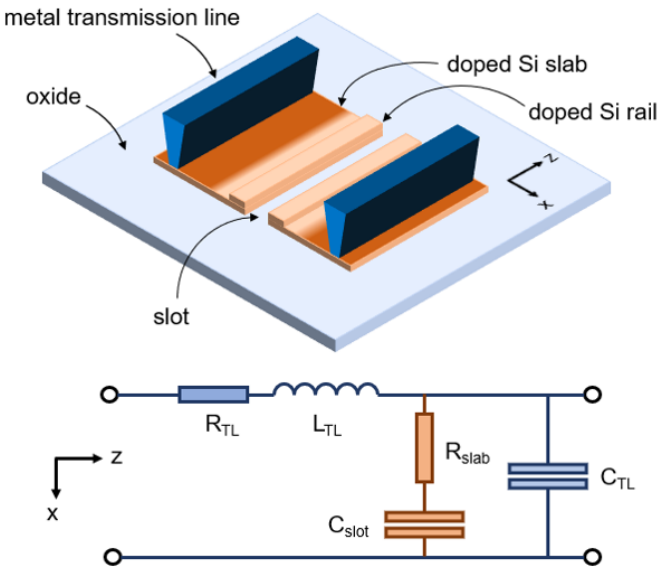

Figure 3.14. Illustration of SOH modulator electrode geometry (top) and the equivalent distributed element circuit model (below). Since the resistivity of the metal electrodes (R_{TL}) is far lower than that of the slab (R_{slab}), longitudinal (z-direction) currents flow only in the metal and currents in the doped silicon slab are predominantly transverse (x-direction). As a result, the slot waveguide can be modeled as a RC shunt.

is true even when the slab conductivity (resistivity) is low (high). If the slab conductivity is pinned at a "low" value while the frequency of the applied signal is increased, the slot capacitance will not be fully charged and discharged during each cycle. However, as there is negligible current flowing through the doped silicon elements, RF propagation loss will be low. In this limit, modulator bandwidth is limited by the time constant of RC shunt. Consequently, low conductivity in doped silicon limits the bandwidth of the SOH modulator even though RF propagation losses are low. When the conductivity of doped silicon is increased, the bandwidth over which the slot capacitance is fully charged and discharged during each cycle increases. At the same time, one picks up RF propagation loss since more current flows through the slab and rails. This RF propagation loss is frequency dependent and steadily increases for frequencies between the corner frequencies of the metal transmission line and the RC shunt. Now the modulator bandwidth is limited by RF propagation loss. These are the two dominant bandwidth-limiting effect in sub-mm SOH modulators.

One limitation of recent work on SOH modulators is that in almost all cases substrate biasing (to induce an electron accumulation layer in the doped silicon slab) was required to achieve operating bandwidths in the 10s of GHz. In addition to requiring very high voltages (100 V – 300 V), this approach suffers from the additional drawback that the electron accumulation layer is induced throughout the slot waveguide, including regions close to the optical mode. Consequently, free carrier-induced optical losses can be quite high. Our choice of foundry enables a workaround to this limitation – two-step or three-step doping profiles. In particular, AIM Photonics offers mutliple doping concentrations for each type of dopant, which makes it possible to have a weakly doped slab (and rail) in the vicinity of the guided optical mode and much higher doping concentrations closer to the metal transmission line. This optimization of the slab doping profile will make it possible to operate SOH modulators without substrate biasing and without incurring unnecessarily high optical losses.

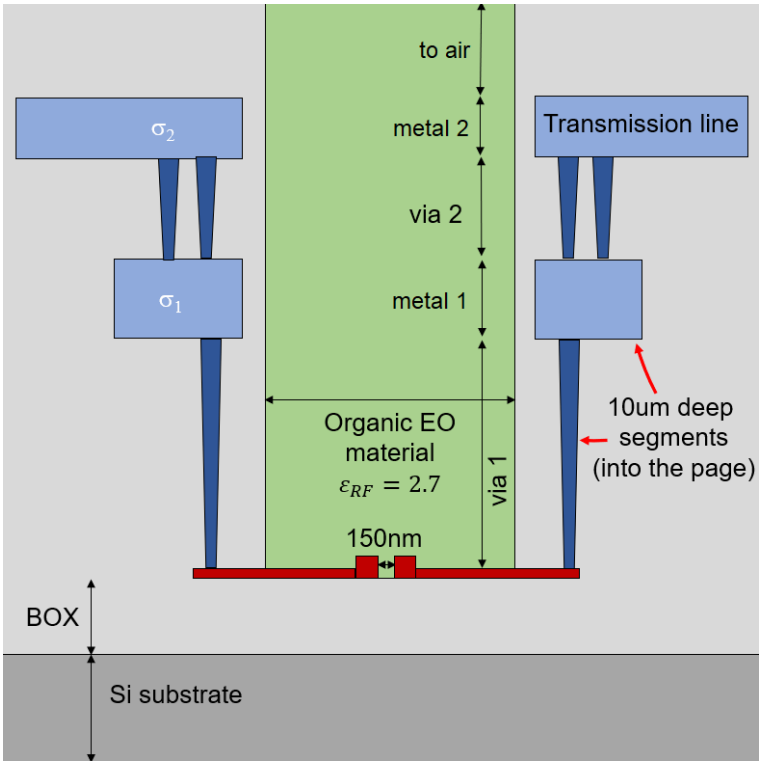

Figure 3.15. Cross section of slot waveguide modulator showing metal routing layers (light blue), metal vias (dark blue), OEO material (green), oxide cladding (gray), doped silicon (maroon), and undoped silicon (dark gray)

A cross section of the slot waveguide modulator with all dimensions relevant to electrode modeling are presented in **Fig. 3.15**. In line with previous work [120]–[122], we model the RF response of the modulator by treating the SOH modulator as a lumped element (RC shunt). As noted earlier, this is because the conductivity of the silicon slab is much lower than that of the metal routing layers, with the net effect that longitudinal currents (into the page in **Fig. 3.15**) flow only in the metal. In addition, the bottom metal layer is segmented (10μm-deep segments each and going into the page) so that it, together with the metal vias, behaves merely as a contacting element rather than as a coupled transmission line. Consequently, we first model the behavior of the upper metal layer, which behaves as a transmission line, with a finite element solver and then incorporate the effect of the slot waveguide (doped silicon slab and slot capacitance) by adding a RC shunt to the equivalent distributed element circuit model (illustration at the bottom of **Fig. 3.14**).

Owing to process constraints set by the foundry, the only parameters one can are the width of the slot waveguide (already determined from consideration of optical performance), the doping profile in the silicon slab (determines the resistance of the RC shunt), and the width of the upper metal trace that forms the transmission line. Results of our modeling are presented in **Fig. 3.16** for a slot width of 150 nm, a slab conductance of 100 S/m, an upper metal trace separation of 30μm, and an upper metal trace width of 30μm.

From the data in **Fig. 3.16** it is clear there will be some reflection of RF power from a 50 Ω driver, as well as a need to terminate the transmission line with a resistance higher than 50 Ω. As the SOH modulators in our initial fabrication run are 350μm long, well below the wavelength of the quasi-TEM mode in the transmissions line, velocity mismiatch is unlikely to limit RF performance in the $10 - 20$ GHz range. Nonetheless, we find a good match between the effective index of the fundamental mode supported by the transmission line (~ 3.0 from **Fig. 3.16**(a)) and the group index of the optical mode ($\sim 3.05 - 3.15$ from simulations). Furthermore, for this device length transmission losses along the electrode are expected to be less than 5%.

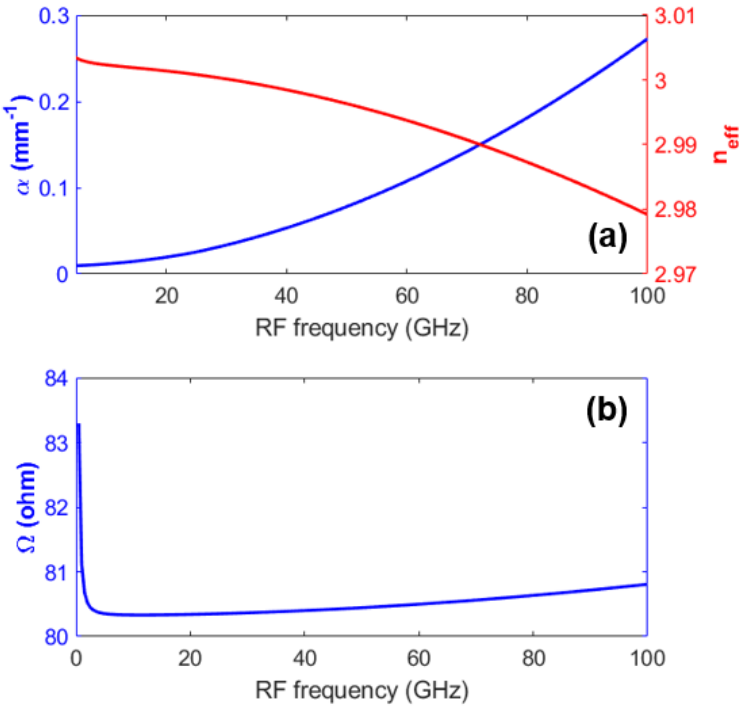

Figure 3.16. Response of SOH modulator electrode geometry based on finite-element simulations of the metal transmission line with the effect of slab resistance and slot capacitance incorporated through a distributed element circuit model. The electrode widths and the separation are each 30μm and the slot width is 150 nm. (a) Attenuation and effective index of the supported quasi-TEM mode as a function of frequency. (b) Real part of the device impedance in ohms.

3.2.4 Projected Performance of the Integrated Quantum Frequency Processor

The approach outlined in this section presents low risk across a range of on-chip elements (narrow linewidth filters, thermo-optic phase shifters) and subsystems (pulse shaper) as these have all been demonstrated by our research group in the past [96], [97], or by customers of AIM Photonics [95], or are available as foundry-qualified elements [123]. The biggest risk concerns the development of SOH modulators. However, the primary criticism of this platform – limited optical power handling – is not at all a concern for quantum light levels. Instead the primary performance risk, at least for the QFP, comes from properly reconciling differences between the design constraints of our foundry (AIM Photonics) with that of the foundry used in many recent SOH modulator demonstrations (A*STAR) [101], [105], [118].

Quantum Frequency Processor	Min. Target	Stretch
Number of elements	3	3
Dimensionality (DFT gate)	> 4	> 12
Gate Fidelity	> 0.999	> 0.999
Success Probability	> 0.95	> 0.95

Electro-Optic Modulator	Min. Target	Stretch
Platform	Silicon-organic hybrid	
Mode	Pockels effect	
Voltage swing	± 3.3V	± 3.3V
Total phase swing	5.0 rad	8.5 rad
3dB EO bandwidth	25+ GHz	50+ GHz
Device length	0.35 mm	0.50mm
Optical loss	1.0 dB	< 1.0 dB

Pulse shaper	Min. Target	Stretch
Platform	Silicon-on-insulator	
Mode	Add-drop filtering	
Number of channels	24	24
Channel separation	8 GHz	2 GHz
Filter linewidth	2 GHz	800 MHz
Optical loss	3.0 dB	< 1.1 dB

Figure 3.17. Minimum and stretch design targets for the proposed three-element QFP

We compile all the relevant high-level and device-level performance targets and present them together in **Fig. 3.17**. Such a QFP can support network- and interconnect-related information processing tasks [Chapter 4] while also opening up new avenues for the study of high-dimensional quantum states. It should be emphasized that the minimum performance targets are based on conservative estimates of component performance as even with the best accounting unknown risks will arise over the course of development. Further, the integrated QFP will be developed over the course of three fabrication runs, with incremental improvements targeted in each round. The listed design targets represent performance at the end of development.

4. ENTANGLEMENT DISTRIBUTION AND NETWORKING

Within the overall landscape of quantum science and technology, the development of quantum networks is critical for applications such as blind quantum computing, connected quantum sensors, and distributed quantum computing [124]. At the most general level, such networks will ultimately be tasked with entangling physically separated quantum nodes and facilitating secure communication between distant parties. Accordingly, to the greatest extent possible, photonic quantum networks should integrate seamlessly into existing fiber-optic infrastructure, while also leveraging advanced techniques in modern classical lightwave communications. The specific application of QKD has has made the leap from lab to field, with many deployed QKD networks already demonstrated [82]–[87]. Nevertheless, the practical implementation of more general functionalities – extending beyond QKD to, e.g., the distribution and verification of high-fidelity quantum entanglement for in principle arbitrary protocols – represents an important need for quantum network development, particularly in the context of approaches that are agile, resource-efficient, and extendable to many users.

To this end, we leverage wavelength multiplexing – a common tool in classical lightwave communications – to support and enhance the performance of quantum networks. One approach to quantum networking that has been gaining traction in recent years is based on entanglement distribution by a central provider [125]–[131]. We build on work in this area by leveraging flex grid technology to demonstrate *reconfigurable* distribution of quantum entanglement in a four-user tabletop network. By adaptively partitioning bandwidth with a single wavelength-selective switch, we successfully equalize two-party coincidence rates that initially differ by over two orders of magnitude. To facilitate network functionality at higher protocol levels [14], [15], we synthesized the first Bell state analyzer (**BSA**) that operates on frequency mismatch directly using electro-optic frequency mixing techniques. Through the use of interleaved frequency beam splitters [30], we realize unambiguous measurement of two frequency-bin–encoded Bell states with discrimination accuracy exceeding 98%. This makes it possible to break the tradeoff between spectral distinguishability and remote entanglement fidelity and represents an important step toward the long-term vision of a quantum internet that is compatible with both heterogeneous nodes and dense spectral multiplexing.

4.1 Adaptive Bandwidth Management for Entanglement Distribution

Over the last decade there has been a great deal of work on entanglement distribution by a central provider [125]–[130]. In this paradigm, broadband, polarization-entangled photons are carved into in a series of spectral slices, which are then distributed to different users in the network. Since these photons are also entangled in the time-frequency degree of freedom, nonclassical correlations in polarization state are shared only between users who receive energy-matched ($\omega_{\text{signal}} + \omega_{\text{idler}} = \omega_{\text{pump}}$) spectral slices, or channels. Early work on this architecture examined the feasibility of the approach in terms of entanglement quality across the biphoton bandwidth [125], as well as in terms of advanced functionality such as users simultaneously maintaining multiple two-party links [126]. Subsequent work introduced new functionality like active switching [127], [128], for example. More recently, Wengerwosky *et al.* [129] demonstrated a fully and simultaneously connected QKD network by multiplexing multiple spectral slices to each user and doing so in a way that enabled a fully connected graph, i.e., a network where nonclassical correlations in polarization state are shared by every possible two-party link [**Fig. 4.1**]. This elegant demonstration relies only on passive components for entanglement distribution, a hierarchical tree of dense wavelength-division multiplexing (**DWDM**) filters, thereby permitting low-loss distribution of polarization entanglement across the network.

One limitation to the use of nested DWDM filters for entanglement distribution is that the approach is not scalable to networks larger than four or five users. For example, a network of only eight users would require over one hundred DWDM filters (number of filters scales as $2N^2 - 3N$; requiring 104 filters when $N = 8$, where N is the number of users). While no one spectral slice passes through every filter, at least a few would have to pass through over ten DWDM filters –- effectively eliminating any loss advantage from the passive approach. Recognizing this limitation, follow-on work [131] made use of 50 : 50 fiber-based beam splitters to improve the scaling of this architecture by having two users share each spectral slice. However, this improvement in resource scaling comes at the expense of higher noise as one can no longer recover the two-party coincidence-to-accidental (**CAR**) ratio

↑The results of this section have been published in [132]

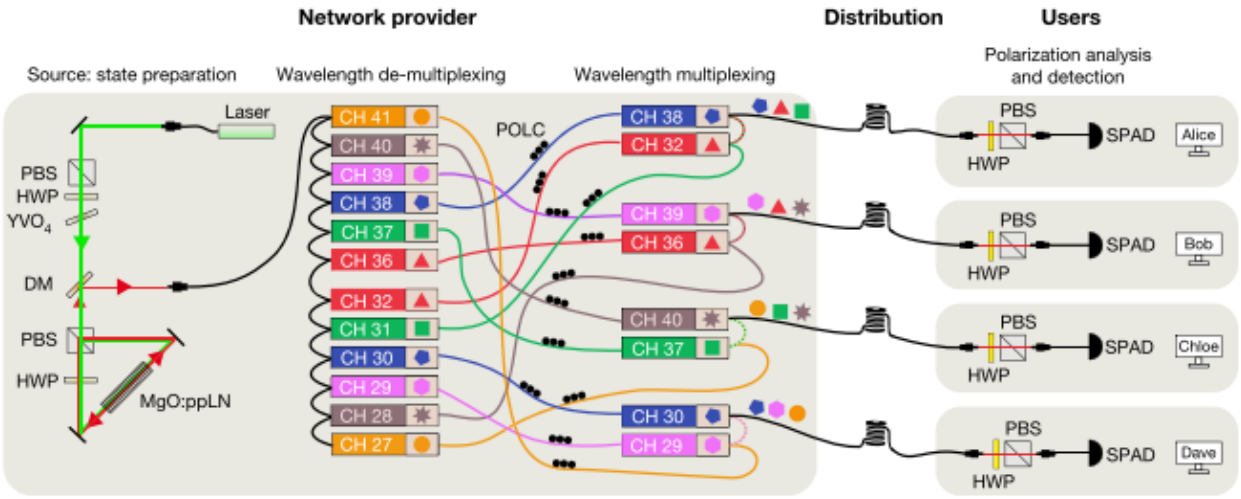

Figure 4.1. Network architecture in Ref. [129]. At the network provider, a laser with a wavelength of 775 nm (green beam) is used to pump a temperature-stabilized MgO-doped PPLN crystal (MgO:ppLN) in a Sagnac-type configuration to create a polarization-entangled state ("state preparation"). The spectrum is then split into 12 International Telecommunication Union (ITU) channels (identified by different colored symbols) by a cascade of band-pass filters ("wavelength de-multiplexing"). The resulting 12 frequency channels were combined into four single-mode fibres such that each user (Alice, Bob, Chloe and Dave) receives three frequency channels (indicated by the coloured symbols) and therefore shares a polarization-entangled pair with each of the other users ("wavelength multiplexing"). Each of the four users receives only one single-mode fibre from the network provider ("Distribution"), and analyses the polarization with a half-wave plate (HWP) and a polarizing beam splitter (PBS). The photons are then detected using one single-photon avalanche diode detector (SPAD) per user ("Polarization analysis and detection"). CH, ITU channel; DM, dichroic mirror; POLC, manual polarization controllers; YVO4, yttrium orthovanadate plate.

owing to the intrinsic loss of 3 dB splitting. Moreover, this improvement only halves what is a quadratic scaling in resources with the number of users. A further drawback of the nested DWDM approach is that the network is not dynamic in any meaningful sense. Adding and dropping users or altering how the spectrum is allocated requires physical rewiring of DWDM filters and beam splitters by the central provider. While the realization of a fully and simultaneously connected network architecture is appealing, it is an open question as to

whether the advantage of using of only passive elements trumps concerns related to scalability and dynamic reconfigurability –- features prized in classical lightwave communications.

4.1.1 Network testbed

Using off-the-shelf telecommunications equipment, we demonstrate a significantly improved approach to entanglement distribution. In lieu of passive optical elements, we use a wavelength-selective switch (**WSS**) to apportion the biphoton bandwidth between users on a network. This approach provides a clear advantage in terms of network scalability as the loss incurred during entanglement distribution is independent of the number of users (insertion loss ~ 5 dB). Furthermore, bandwidth allocation can be reconfigured dynamically with simple electronic control. Consequently, the central provider of entanglement can not only enable a fully and simultaneously connected network, but *any arbitrary subgraph*. Lastly, the bandwidth of spectral slices routed to each user can be modified, thus making it possible to boost or throttle the key rate for a particular two-party link without any modification to the pair source or the pump laser and without affecting other links on the network.

Our testbed is illustrated in **Fig. 4.2**. Similar to the experiments in section 3.1.2 (see text for details), spectrally degenerate time-energy entangled photons are generated by type-II SPDC in PPLN. Therefore, any two energy-matched spectral slices ($\omega_{\text{signal}} + \omega_{\text{idler}} = \omega_{\text{pump}}$) are entangled in polarization state. The output of the PPLN is sent to a WSS to multiplex arbitrary spectral slices across the C- and L-bands to any one of four output ports. The only limitation on this programmability is the resolution of the WSS (~ 20 GHz), which sets a lower bound on the bandwidth of individual spectral slices. Photons are then carried from the output ports to four users by standard (single mode) optical fiber.

The users, identified as Alice, Bob, Carol, and Dave, are each equipped with a polarization analysis module that includes a fiber-based polarization controller (**FPC**), a quarter-wave plate (**QWP**), a half-wave plate (**HWP**), a polarizer, and a single-photon detector. The FPC compensates for rotation of the polarization state that occurs during transmission between the source and the polarization analysis module. While the FPC can map the state of polarization from the HV axes of the source to the HV axes of the polarization analysis

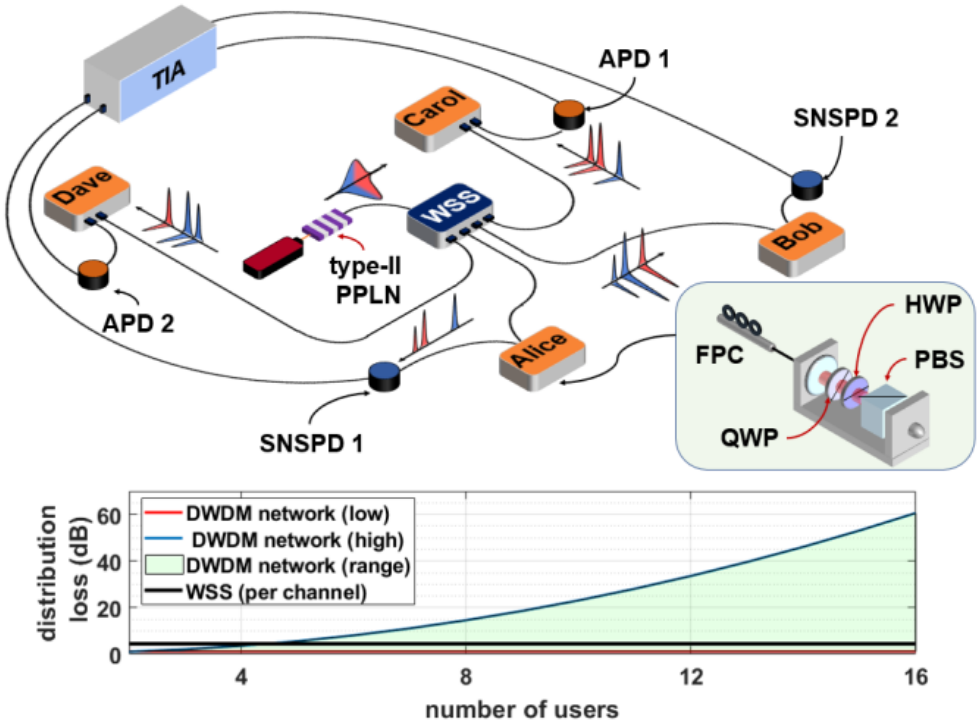

Figure 4.2. Network testbed for adaptive entanglement distribution. CW laser, continuous-wave pump laser; type-II PPLN, periodically-poled lithium niobate waveguide engineered for type-II phase matching; WSS, wavelength selective switch; FPC, fiber polarization controller; QWP, quarter-wave plate; HWP, half-wave plate; PBS, polarizing beam splitter; SNSPD, superconducting nanowire single-photon detector; APD, single-photon avalanche diode.

module, there is no obvious way to compensate for the phase difference accrued between two-photon basis states $|HV\rangle_{SI}$ and $|VH\rangle_{SI}$. In other words, the biphoton state at a pair of polarization analysis modules is described by $|\Psi\rangle \propto |HV\rangle_{SI} + e^{i\phi}|VH\rangle_{SI}$, where ϕ is this unknown phase. Although polarization correlation measurements in the HV basis are unaffected, one can only obtain high visibility in the DA basis for values $\phi \in \{0, \pi\}$. We compensate for the unknown phase ϕ by orienting all QWPs at 45°, followed by additional rotation of the HWP settings, for polarization correlation measurements in the DA basis [133]. The HWP angle at which maximum contrast is obtained corresponds to compensation of ϕ and thus the "effective" DA basis; concretely, we set the angle such that the ideal quantum state is $|\Psi\rangle \propto |HV\rangle_{SI} - |VH\rangle_{SI}$. An event timer (TIA, **Fig.** 4.2) tabulates single-photon

events from all users, which we use to generate a histogram of two-photon delays for all two-party links.

We note that of the four detectors used in this testbed, two are SNSPDs while the remaining are InGaAs avalanche photodiodes (**APDs**). The SNSPDs are used by Alice and Bob and are each free running with a quantum efficiency ~ 0.85 and a deadtime of 30 ns. The InGaAs APDs, which are allocated to Charlie and Dave, are gated with a 20 MHz clock (10% duty cycle) and have quantum efficiencies of ~ 0.1 and 0.2, respectively, with deadtimes of 1000 ns. **Fig. 4.3(b)** shows the singles rate at each detector when the WSS is programmed to operate as a multiport $(1:4)$ beam splitter over the full biphoton bandwidth. It is clear that the singles rate is influenced not just by differences in detector efficiencies, but also by the use of gated detection with a CW pump in the case of APDs.

Prior to apportioning the biphoton bandwidth for entanglement distribution over the network, we first characterize the quality of polarization entanglement after the WSS using

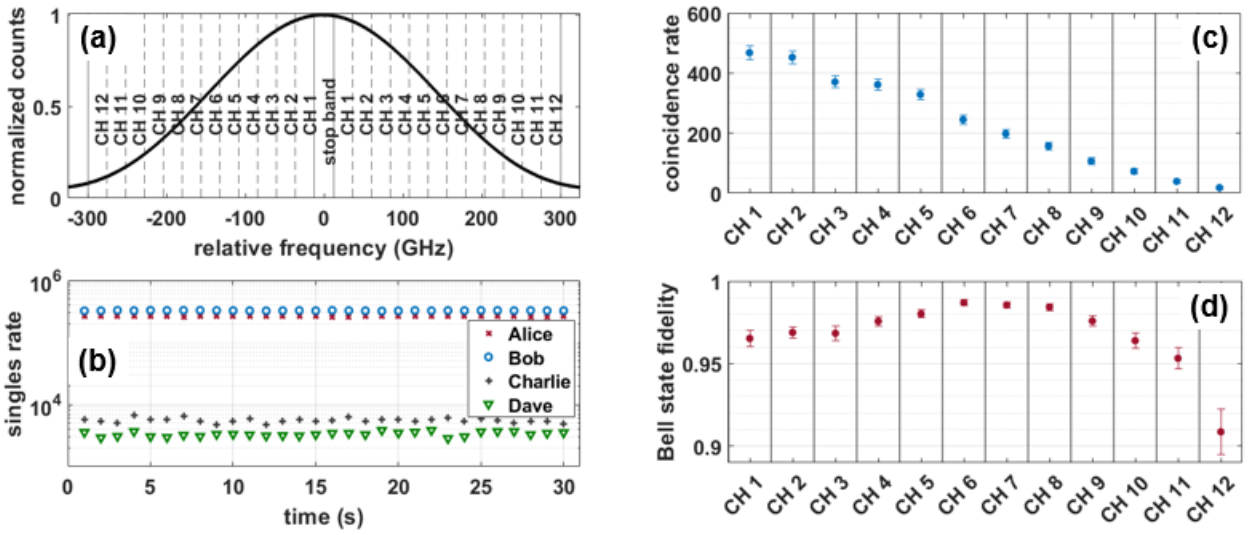

Figure 4.3. **(a)** Sinc-squared fit to the normalized singles rate as a function of detuning from the center of the biphoton spectrum. The locations of 12 pairs of energy-matched spectral slices are overlaid on the spectrum. **(b)** Singles rate at each user when the wavelength-selective switch is programmed to operate as a $1:4$ power/beam splitter. **(c)** Coincidence rate between Alice and Bob (SNSPD–SNSPD link) for all 12 channels. **(d)** Bell state fidelity for all 12 polarization-entangled channels computed using Bayesian mean estimation.

Alice's and Bob's polarization analysis modules (SNSPD-SNSPD link). In particular, the ∼310 GHz-wide sinc-squared spectrum is carved into 24 spectral slices, each of which is 24 GHz wide and includes a central stopband [**Fig. 4.3(a)**]. The filter response of the WSS is centered with respect to the degeneracy point of the pump laser ($\frac{\omega_{\text{pump}}}{2}$). In other words, spectral slices that are symmetric with respect to the center of the biphoton spectrum are entangled in polarization state. We define a channel as a *pair* of such energy-matched spectral slices and there are such 12 channels across the the biphoton bandwidth. Bell state fidelity, relative to the $|\Psi^-\rangle$ Bell state, is determined on the basis of four polarization correlation measurements in each of two mutually unbiased bases (HV and DA). Despite the tomographic incompleteness of this two-basis-pair set, our use of Bayesian mean estimation [134], [135] nevertheless enables us to obtain meaningful state estimates, which additionally – due to the high correlations obtained – contain low uncertainty. Our measurement results using the Bayesian tomography workflow of Ref. [74] are presented in **Fig. 4.3(d)**. For channels 1–11, which span most of the biphoton bandwidth, we are able to measure fidelities higher than 0.95, which illustrates not only the high quality of compensation for polarization rotation, but also the stability of the polarization diversity scheme of the WSS. As has been noted in prior work [125], [127], there is a wavelength dependence to the unknown phase ϕ accrued between two-photon basis states, which ultimately limits the fidelity of polarization correlation measurements when using a single setting $\{\theta_{\text{QWP}}, \theta_{\text{HWP}}\}$ across the entire biphoton bandwidth to compensate for this phase.

4.1.2 Bandwidth provisioning and entanglement distribution

The four-user network illustrated in **Fig. 4.2** comprises six possible user-to-user connections. Henceforth, a link is taken to mean a user-to-user connection between whom nonclassical correlations in polarization state are shared. The uppermost illustration in each of **Figs. 4.4(a), (b), and (c)** is a representation of the quantum correlation layer showing all six links of the network. Each link is assigned a unique color, which carries over to the plots below, as well as their insets.

The type-II PPLN is pumped with ∼24 mW of light at 779.65 nm and the down-converted photons, after compensation for temporal walk off (see section 3.1.2 for details), pass to the WSS for wavelength-multiplexed distribution to Alice, Bob, Carol, and Dave. Single-photon events at each detector are tabulated by the event timer to generate a histogram of the delay between single-photon events for every pair of users. A suitable electronic offset is added to electrical pulses from each detector in order to position the coincidence windows of all six link approximately 10 ns away from one another [**Fig** 4.4]. We used a relatively large

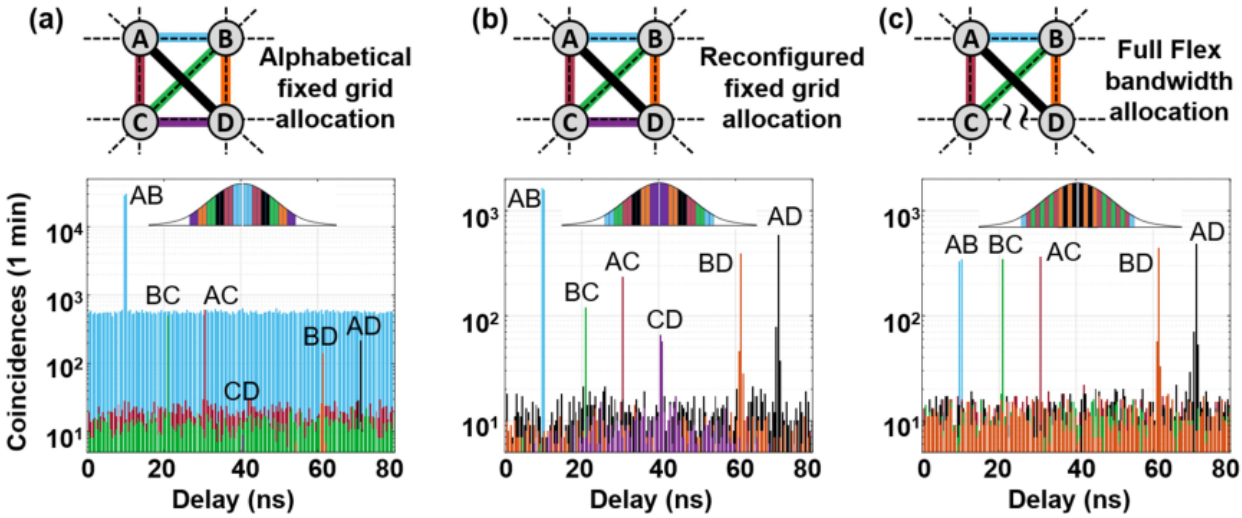

Figure 4.4. *(top graphic, all figures)* Abstracted illustration of the four–user network with dashed lines denoting the possible ways in which nonclassical correlations in polarization state may be shared. There are six unique user-to-user connections, or links, which have each been assigned a unique color. (a) Coincidence rates for each two-party connection based on allocation of the biphoton bandwidth on a fixed 48 GHz grid and following an alphabetical ordering of links. The inset illustrates how the biphoton bandwidth is apportioned between all six links. (b) Coincidence rates for a fixed 48 GHz grid, but with the allocation of spectral channels reconfigured to harmonize (as best possible) the coincidence rate among all links. (c) Histogram highlighting the use of increased flexibility in provisioning of the biphoton bandwidth. In particular, twenty four 24 GHz-wide spectral slices are allocated between four users in a way that harmonizes the coincidence rates across a subgraph of the network. Link CD, which corresponds to the connection between Carol and Dave (APD-APD link), is dropped by the central provider as this link would draw a disproportionate fraction of the biphoton bandwidth when equalizing the coincidence rates across all six two-party links.

coincidence window of 1024 ps because the timing uncertainty (jitter) was not uniform across all detectors. The respective values for Alice's, Bob's, Charlie's, and Dave's detectors were approximately 80 ps, 80 ps, 250 ps, and 450 ps, respectively.

The bandwidth allocation scenarios described below are all based on the same unit – an energy-matched pair of 24 GHz-wide spectral slices, i.e., the channels described in **Fig. 4.3(a)**. In the two fixed-grid scenarios, each link utilizes two consecutive 24 GHz-wide spectral slices for entanglement distribution based on a 48 GHz grid. In the final scenario, which we dub "Full Flex," the 24 GHz-wide channels are allocated to different users without limitation.

Alphabetical fixed grid allocation

We first consider the case of wavelength-multiplexed entanglement distribution based on a fixed 48 GHz-wide grid, chosen to yield a total of 6 equal-width pairs (as needed for full connectivity) from the total of 12 channels defined in **Fig. 4.3(a)**. The biphoton bandwidth, starting from the center and moving to tails, is allocated to the different two-party links based on alphabetical ordering, i.e., links Alice–Bob (AB), Alice–Carol (AC), Alice–Dave (AD), Bob–Carol (BC), Bob-Dave (BD), and Carol–Dave (CD). **Fig. 4.4(a)** shows a histogram of two-photon delays recorded between all six links. Coincidence windows are located at delays of approximately 10 ns, 20 ns, 30 ns, 40 ns, 60 ns, and 70 ns. We call attention to link CD, which is not visible in the histogram. This is due to the fact that link CD represents the two least efficient channels and, under this distribution scenario, also receives the weakest (lowest photon flux) pair of 48 GHz-wide spectral slices.

If one starts out with the goal of minimizing differences in the coincidence rate across links, this allocation represents a far-from-optimal outcome for entanglement distribution based on a fixed spectral grid. However, this might also be interpreted as boosting service for premium links, Alice-Bob in this case. Our point in noting possible criteria for entanglement distribution is to highlight the value of flexible bandwidth allocation in configuring the network for different needs, such as diverse quality-of-service targets.

Reconfigured fixed grid allocation

With the intent of reducing the difference in coincidence rates across all six links, we reallocated the biphoton bandwidth on the same fixed 48 GHz spectral grid. Now, brighter slices of the spectrum are routed to the lossier or less efficient links. **Fig. 4.4(b)** shows histograms for the delay between two-photon events for all user-to-user connections. While the previous scenario saw differences of close to three orders of magnitude in the coincidence rate, that difference is now much lower.

To be sure, this ability to manage coincidence rates derives not just from flexible allocation, but also from the fact that we are using close to the full biphoton spectrum. As **Fig. 4.3(c)** clearly shows, coincidence rates can differ by as much as a factor of 20 depending on which channels one is using. This use of the full down-conversion spectrum marks a departure from previous works, which limited consideration to spectral slices close enough to the center of the biphoton spectrum that there were minimal differences in the pair flux between different spectral slices (prior to distribution). Our results show that in the case of links with disparate efficiencies there is utility in using all parts of the down-converted spectrum and not just those in the flatband region.

Full Flex bandwidth provisioning

We now move from fixed gird distribution to a more flexible provisioning of the bandwidth. In particular, we utilize the 12 channels defined in **Fig. 4.3(a)**, but do not place any limitations on how they are allocated between the different links. Proceeding with the goal of minimizing the difference in coincidence rates across the network, we provision the spectrum as shown in the inset of **Fig. 4.4(c)**. One change from the scenarios shown in the insets of **Figs. 4.4(a) and (b)** is that we no longer enable a fully connected network. This because link CD, i.e., the link between Carol and Dave (APD–APD), would not, even in the most optimistic scenario (sending 7 channels with the highest pair flux to this link), be able to establish a positive secure key rate as the CAR is worse than $9:1$. Therefore, we programmed the WSS to enable a subgraph of the network – links AB, AC, AD, BC, BD – and proceed to harmonize the coincidence rate among the remaining links. From **Fig. 4.4(c)**

we see that all coincidence rates are within a factor of 2 of one another, in stark contrast to the fixed grid cases.

By replacing nested DWDMs with a single WSS we have been able to not only realize a fully and simultaneously connected network for entanglement distribution, but also demonstrated dynamic reconfigurability of the network by (i) enabling subgraphs of the full network, (ii) accommodating quantum channels with disparate loss, and (iii) providing differentiated service. In addition, programmable flex-friendly systems, like WSSs and Fourier-transform pulse shapers, can potentially enable dispersion compensation by a central node, support quantum information processing and communication in different degrees of freedom [32], as well as enable efficient spectrum allocation in complex network environments that need to support not only communication but also mediate entanglement between end nodes.

4.2 Bell State Analyzer for Spectrally Distinguishable Photons

The previous section considered how one might harness spectral multiplexing of quantum channels to distribute entanglement over a multi-user network. While this demonstration involves quantum state transport, that transport only enables the exchange of classical information through, for example, the generation of secure keys for encryption [3] or the direct transmission of secure messages [13]. True quantum communication requires transport of *quantum* information from one node to another.

4.2.1 Quantum Repeaters and Remote Entanglement

The quantum repeater protocol [23] offers a framework to overcome two sources of error that occur during transport of a quantum state over a communications channel – loss and decoherence. The basic insight is that one can partition an arbitrarily long link of length L into a series of smaller links of length $\frac{L}{2^N}$ and efficiently generate entanglement across the full link, i.e., from one end to the other, through a sequence of entanglement swapping [136] between the smaller links. Provided entanglement swapping proceeds after photons have traversed the extent of each smaller link, the associated entanglement generation, coupled

↑The results of this section have been published in [75], [76]

with entanglement purification [137] to correct for the effects of decoherence, offers a path to quantum communication that scales better than direct transmission over long distances. This scaling can be further improved by multiplexing quantum channels in the temporal [24], spatial [25], and spectral domains [26].

The generation of entanglement between parties that share no prior entanglement or history with one another is critical not just to the high-level framework enumerated above, but also to more advanced repeater concepts [138]–[140]. This is accomplished through the teleportation-based quantum gate [24], which can be based on single- or two-photon interference. Prior to a discussion of methods based on two-photon interference, we consider an example of the former – the DLCZ protocol [138].

DLCZ Protocol

The DLCZ protocol is named after inventors Duan, Lukin, Cirac, and Zoller. A concept illustration from the original work is presented in **Fig. 4.5** and shows two physically separated atomic ensembles (L and R) that are pumped simultaneously such that a single (Stokes) photon is emitted with some low probability p in the forward direction. The process for the collective system can be described by:

$$\left(1+\sqrt{p}(s_L^\dagger a_L^\dagger \mathrm{e}^{\mathrm{i}\phi_L}+s_R^\dagger a_R^\dagger \mathrm{e}^{\mathrm{i}\phi_R}+\mathcal{O}(p)\right)|0\rangle \tag{4.1}$$

ϕ_L (ϕ_R) is the phase of the pump field that excites ensemble L (R) and $s_L^\dagger$ ($s_R^\dagger$) and $a_L^\dagger$ ($a_R^\dagger$) are the bosonic operators for the Stokes photon and the atomic excitation, respectively. $|0\rangle$ corresponds to the vacuum state and $\mathcal{O}(p)$ represents the contribution of multiphoton events.

An optical filter ("Filter", **Fig. 4.5**) rejects residual pump light while the Stokes photon, which may be emitted from either ensemble, is directed to a 50 : 50 (spatial) beam splitter. The mode that populates the path toward detector D_1 is $\frac{1}{\sqrt{2}}(a_L\mathrm{e}^{-\mathrm{i}\theta_L}+a_R\mathrm{e}^{-\mathrm{i}\theta_R})$ while $\frac{1}{\sqrt{2}}(a_L\mathrm{e}^{-\mathrm{i}\theta_L}-a_R\mathrm{e}^{-\mathrm{i}\theta_R})$ is the mode that populates the path to detector D_2. The term θ_L (θ_R) corresponds to the phase accumulated by the photon as it propagates from ensemble L (R)

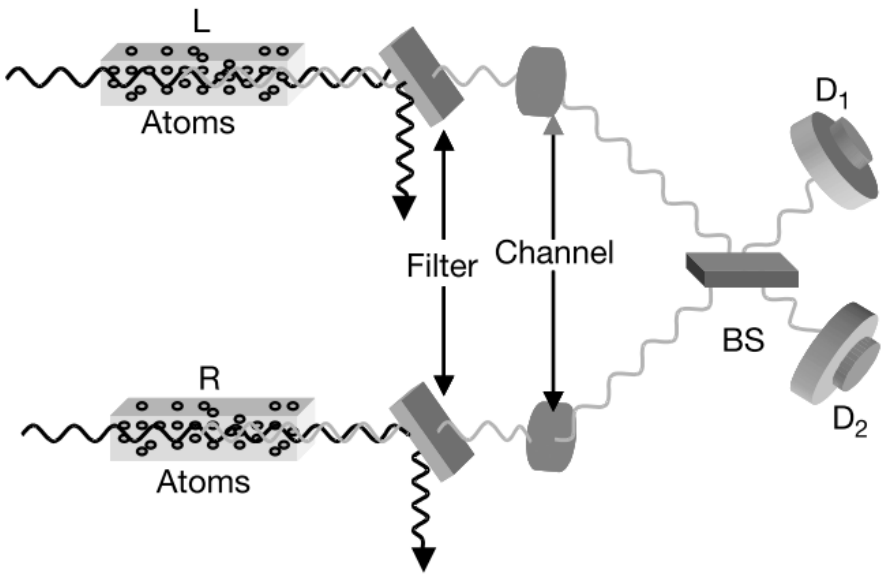

Figure 4.5. Atomic ensembles L and R are excited with synchronized pump pulses (waves in solid dark). A single Stokes photon (waves in light grey) is emitted in the forward direction from one of the ensembles and travels over a communications channel to 50 : 50 beam splitter BS. Single-photon interference is captured by a single click from one of detectors D_1, D_2, which entangles the atomic ensemble L and R through a delocalized atomic excitation. Source: Ref [138]

to the beam splitter BS. The detection of a photon at D_1 projects atomic ensembles L and R onto the entangled state:

$$|\psi\rangle_{LR} = \frac{1}{\sqrt{2}}\left(s_L^\dagger e^{i(\phi_L+\theta_L)} + s_R^\dagger e^{i(\phi_R+\theta_R)}\right)|0\rangle \tag{4.2}$$

This can be recast as:

$$|\psi_{LR}\rangle = \frac{1}{\sqrt{2}}\left(|1\rangle_L|0\rangle_R + e^{i(\Delta\phi+\Delta\theta)}|0\rangle_L|1\rangle_R\right) \tag{4.3}$$

where $\Delta\phi = \phi_R - \phi_L$ and $\Delta\theta = \theta_R - \theta_L$ and represent the relative phase between the respective pump fields and optical paths, respectively. $|0\rangle$ and $|1\rangle$ denote the ground and excited states of the ensemble.

In this method of entanglement generation, the system starts out with entanglement between an atomic excitation in the ensemble and the respective (Stokes) photon. Detection

of a single photon after the beam splitter projects the photon onto one of two *single-photon* (path) entangled states, thereby generating entanglement between the ensembles through a delocalized atomic excitation after photon detection. However, as equation 4.3 illustrates, there is a clear drawback to this approach. It requires phase stability over the the length of the links, which is a challenging requirement for long distance communication, leading to fluctuations in $\Delta\theta$ and, therefore, in the phase of the state describing the entangled atomic ensembles.

Heralded Entanglement Generation with Bell State Measurements

Entanglement swapping based on two-photon interference, or so-called Bell state measurements, overcomes the issue of link stability that limits the robustness of single-photon-based entanglement generation protocols. The term Bell states refers to the four maximally entangled states possible for a pairs of qubits [11]. For the specific case of photonic polarization qubits A and B, the four Bell states are:

$$|\phi^{\pm}\rangle_{AB} = \frac{1}{\sqrt{2}}\left(|H\rangle_A|H\rangle_B \pm |V\rangle_A|V\rangle_B\right) \tag{4.4}$$

$$|\psi^{\pm}\rangle_{AB} = \frac{1}{\sqrt{2}}\left(|H\rangle_A|V\rangle_B \pm |V\rangle_A|H\rangle_B\right) \tag{4.5}$$

A measurement of the polarization state of A or that of B alone would yield a random outcome. However, the two-photon state is well-defined and if the polarization state of A and B are measured using the same settings (bases) their individual outcomes, while completely random, are perfectly correlated with one another.

Consider two indepdent sources of entangled photons that each generate a Bell state like $|\psi^-\rangle$, for example. This situation is illustrated in **Fig. 4.6** and here EPR-source I sends photon 1 to the left and photon 2 to the right. Likewise, EPR-source II sends photon 3 to the left and photon 4 to the right. While photons 1 and 2 are entangled, as are photons 3 and 4, no photon generated by EPR-source I is entangled with any photon generated by

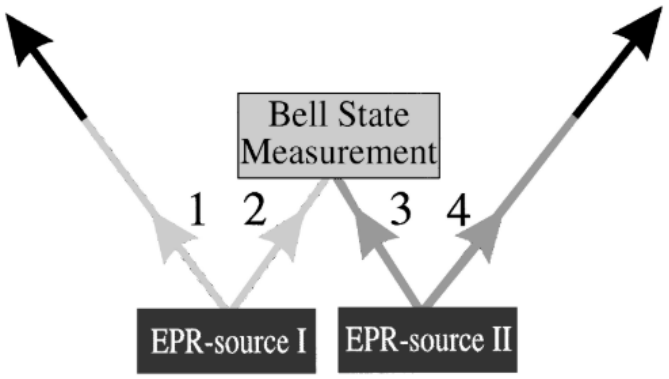

Figure 4.6. High-level illustration of the principle of entanglement swapping. Two Einstein-Podolsky-Rosen (EPR) sources each generate a pair of entangled photons – source I generates entangled photons $1-2$ and source II generates entangled photons $3-4$. Photons 2 and 3, which are themselves not entangled are measured in the Bell basis through a joint measurement (Bell State Measurement), which projects photons 1 and 4 onto an entangled state. Source: Ref [141]

EPR-source II. Nonetheless, one can describe the four-particle system in terms of Bell states of photon pairs $1-4$ and $2-3$.

$$|\Psi\rangle_{1234} = \frac{1}{2}\left(|\psi^+\rangle_{14}|\psi^+\rangle_{23} - |\psi^-\rangle_{14}|\psi^-\rangle_{23} - |\phi^+\rangle_{14}|\phi^+\rangle_{23} + |\phi^-\rangle_{14}|\phi^-\rangle_{23} \right) \tag{4.6}$$

Note that a sum of Bell states is not an entangled state. To entangle photons 1 and 4, photons 2 and 3 are directed to an apparatus capable of performing a Bell state measurement. While photons 2 and 3 are not entangled, the effect of the joint measurement is that it projects photons 2 and 3 onto the basis of Bell states, which in turn projects photons 1 and 4 onto an entangled state. For example, if the outcome the Bell state measurement on photons 2 and 3 is a detection event corresponding to state $|\psi^+\rangle_{23}$, then the four-photon state described by equation 4.6 collapses to the first term, thereby entangling photons 1 and 4, which are in the $|\psi^+\rangle_{14}$ Bell state.

A module or system capable of projecting two photons onto the Bell basis through a joint measurement is called Bell state analyzer, or BSA for short. One limitation of Bell

state analyzers based on linear optics is that they can only distinguish two of four Bell state unambiguously [142]. While the measurement requires interference between two-photon outcomes, that interference between outcomes is independent of any phase accrued by photons along their optical paths [24]. In other words, so long as their is sufficient temporal overlap between the photons participating in joint measurement any instabilities in the communications channel are not imprinted on the newly entangled state. Consequently, entanglement swapping based on two-photon interference is more robust than single-photon techniques like the DLCZ protocol.

4.2.2 The Bell State Analyzer

The discussion of Bell state measurements has thus far not focused on any particular implementation or arrangement nor any particular degree of freedom in photons. We introduce the linear optics Bell state analyzer through a presentation of the first work on this topic [143], [144], which like many early experiments is based on polarization qubits. These experiments did not address entanglement swapping *per se* but instead focused on validating the concept of a two-state or partial Bell state analyzer. A Bell state of choice was prepared deterministically and sent to the apparatus for Bell state measurement. In other words, if the input to a Bell state analyzer is the entangled state $|\psi^-\rangle$, then the outcome of *any* joint measurement by the Bell state analyzer should correspond only to those detection outcomes particular to $|\psi^-\rangle$.

The Bell state analyzer in Mattle *et al.* [144] is shown in **Fig. 4.7**. A polarization-entangled state is generated by spontaneous parameteric down-conversion in a nonlinear crystal (BBO, **Fig. 4.7**). The combination of half- and quarter-wave plates at Bob's location operates on only one of two photons in an entangled pair, which permits deterministic preparation of any desired Bell state. The prepared state is then sent to a $50:50$ (spatial) beam splitter (BS, **Fig. 4.7**) where the respective polarization components mix and populate outcomes along each of two output paths. Each output path further includes a polarizing beam splitter (POL, POL' in **Fig. 4.7**), thereby allowing one to demultiplex all possible

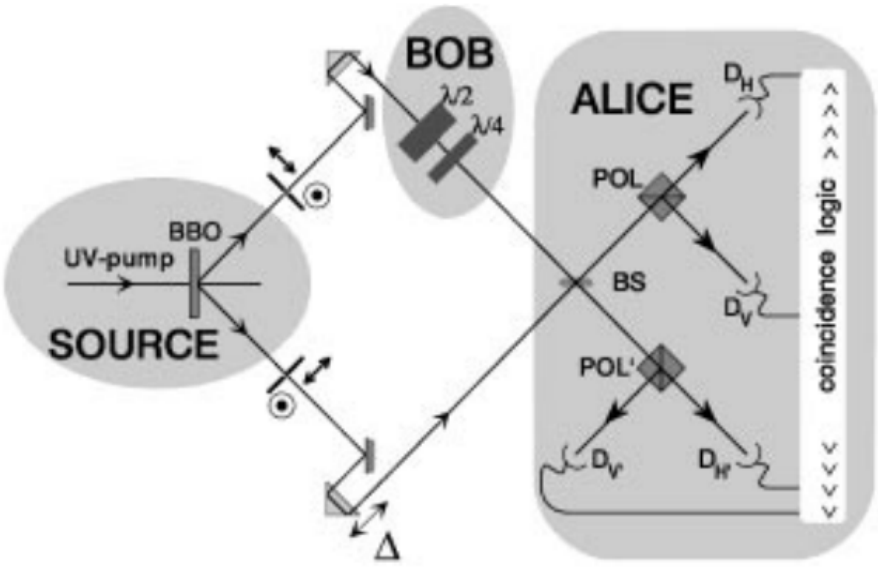

Figure 4.7. Experiment for quantum dense coding with a source of entangled photons (*SOURCE*), a means for "BOB" to prepare arbitrary Bell states, and a partial Bell state analyzer for "ALICE" to recover the the message, i.e., discern the Bell state prepared by "BOB". Source: Ref [144].

outcomes that can be populated – two polarization states in each of two output paths for a total of four possible single-photon events at detectors D_V, D_H, D'_V, D'_H.

The particular combination of two-detector clicks depends on the input state. For Bell state $|\psi^-\rangle$ state, which has an antisymmetric spatial component, photons antibunch at the beam splitter. This results in one click in the top pair of detectors (D_V, D_H) and another in the bottom pair of detectors ($D_{V'}$, $D_{H'}$), each of the clicks corresponding to orthogonal polarization states. In the case of $|\psi^+\rangle$, two clicks either both occur in the bottom pair of detectors or in the top pair of detectors. When the input to the system is $|\phi^\pm\rangle$, photons bunch at a detector. While this allows one to identify the presence of $|\phi^\pm\rangle$, $|\phi^+\rangle$ and $|\phi^-\rangle$ cannot be distinguished from one another, thereby limiting *any* linear optics Bell state analyzer to maximum efficiency of 50% [142].

Spectral Indistinguishability

Successful operation of the partial Bell state analyzer described above is premised on photons participating the joint measurement being spectrally indistinguishable. This is be-

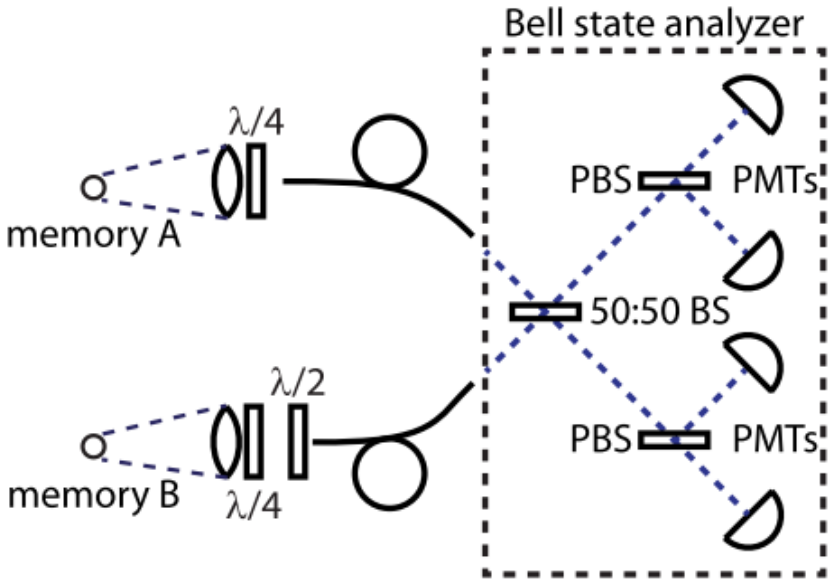

Figure 4.8. Experimental setup showing two ion-based quantum memories A and B, as well as the respective optics for photon collection and conversion of the polarization state to the rectilinear basis (HV). Photons are coupled into fiber and carried to a partial Bell state analyzer, which includes a spatial beam splitter (50 : 50 BS), two polarizing beam splitters (PBSs), and photomultiplier tubes (PMTs). Source: Ref [145]

cause quantum interference is predicated on interference between possible outcomes. For spectrally distinguishable photons, the outcomes (under many circumstances) can be distinguished from one another and, consequently, do not interfere as they would have if the photons had been spectrally indistinguishable.

To understand the effect of spectral distinguishability, consider the generation of remote entanglement between two ion-based ($^{171}Yb^{+}$) quantum memories as shown in **Fig.** 4.8, excerpted from work by Vittorini *et al.* [145]. Memories A and B are excited such that they each emit a photon whose state of polarization is entangled with the excitation of the ion. However, the photons emitted by the memories are spectrally distinguishable from one another and this can be represented by the separation in their center frequencies, i.e, $\Delta\omega = \omega_A - \omega_B$. As described earlier in this subsection, two photons undergo a Bell state measurement in a partial Bell state analyzer. For coincident detector clicks, the memories are projected onto the entangled state:

$$|\psi\rangle_{AB} = \frac{1}{\sqrt{2}}\left(|\uparrow\rangle_A |\downarrow\rangle_B \pm e^{i(\Delta\omega\Delta t + 2\Delta\omega t)} |\downarrow\rangle_A |\uparrow\rangle_B\right) \tag{4.7}$$

While the memories are indeed entangled, one can clearly see the effect of spectral distinguishability. The first and less deleterious effect is that the memories are not projected onto a Bell state. In the Bell basis, the entangled memories have a time dependent phase $2\Delta\omega t$, where t is the time elapsed since detection of the second photon. In the term $\Delta\omega\Delta t$, Δt corresponds to the time interval between detection of the first and the second photon. While this term is fixed for a particular measurement, it fluctuates from one measurement to the next. Consequently, memories are not projected onto one of two possible Bell states, but instead take on any arbitrary entangled state between $|\psi^+\rangle_{AB}$ and $|\psi^-\rangle_{AB}$, *which varies with each measurement*. To project the memory onto a preferred entangled state after each measurement, one has two options – postselect for events with a particular value of Δt [146] or apply a suitable correction to rotate the memory qubits to a the desired state after each joint measurement [145], [147]. Both approaches require time-resolved coincidence detection and come with additional drawbacks. In case of the former, temporal postselection leads to a significant drop in the entanglement generation rate and in case of the latter one needs to implement feedforward qubit rotations, which require fast and sophisticated control.

Despite what these seemingly acceptable workarounds might suggest, their efficacy is limited by a more fundamental issue – the timing uncetainty associated with single-photon detection. In other words, Δt cannot be determined with absolute certainty. This timing resolution (Δt_r), or jitter, leads to an ambiguity in the phase of the entangled memory state. This ambiguity is on the order of $\Delta\omega\Delta t_r$, which is linear with the frequency separation between photons. For single-photon detectors with (two-photon) timing resolution on the order of 20 ps, an ambitious number for commercially available systems, a frequency separation of just 2.5 GHz leads to a $0.1\boldsymbol{\pi}$ ambiguity in the phase associated with the entangled memory state [**Fig. 4.9**].

While spectral distinguishability might present a minor issue for entangling similar matter-based qubit species, owing to only small differences in local environments, it presents a much

larger challenge for networks that support heterogeneous nodes or that leverage the tremendous bandwidth of optical fiber for the spectral multiplexing of quantum channels, or both.

4.2.3 Frequency Domain Bell State Analyzer

To resolve this tension between spectrally-multiplexed quantum state transport and high-fidelity entanglement generation, we synthesize a partial Bell state analyzer where two frequency-bin-entangled photons are mixed not with a spatial beam splitter, but rather with frequency beam splitters [35] that intentionally leverage frequency mismatch.

Concept of Frequency Mixing-Based Bell State Analyzers

Our conception of a partial Bell state analyzer can, in principle, operate on photons carrying quantum information in any degree of freedom. However, for this demonstration we focus on discrete variable frequency encoding, where quantum information is carried by clearly delineated frequency modes rather than by orthogonal polarization modes.

Figure 4.10(a) is a high-level illustration of such a Bell state analyzer and its operation can be understood in analogy to the partial Bell state analyzer for polarization qubits

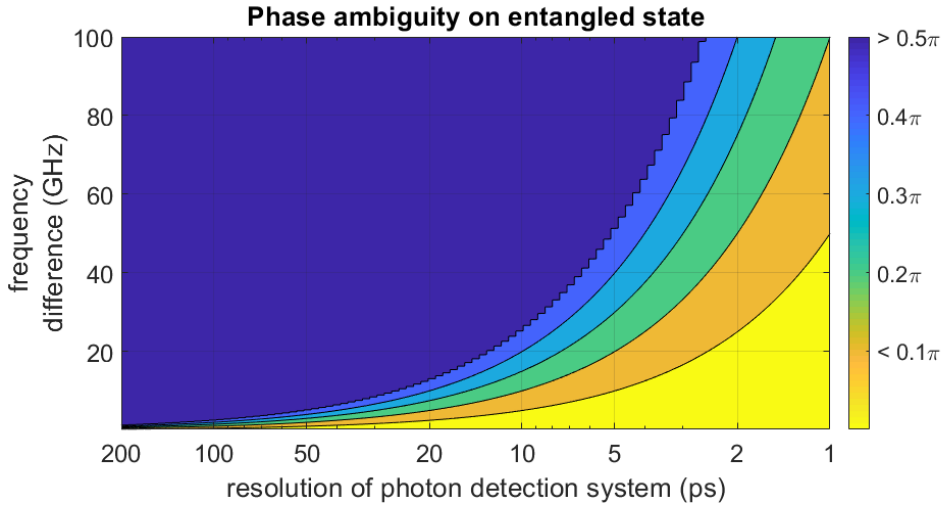

Figure 4.9. Phase ambiguity on generated remote entanglement as a function of spectral distinguishability (in GHz) and timing resolution of the two-photon detection system (ps).

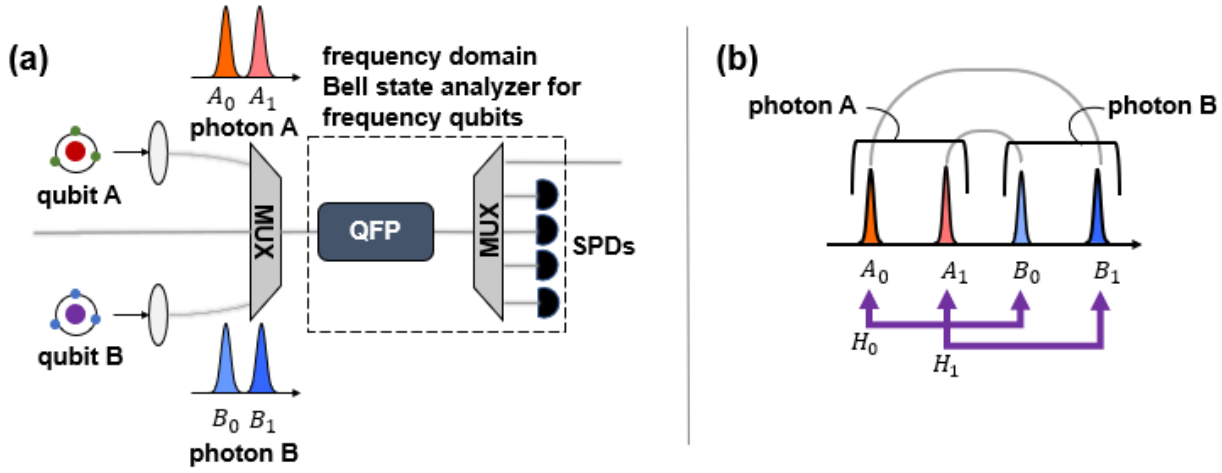

Figure 4.10. (a) A frequency mixing-based Bell state analyzer for photonic frequency qubits. Matter-based qubits A and B are entangled with the frequency degree of freedom in photons A and B, respectively. The action of the $50:50$ spatial beam splitter used in conventional partial Bell state analyzers is replaced by a frequency beam splitter implemented using the quantum frequency processor (QFP) paradigm. Demultiplexing of the different spectral modes performs the role that a pair of polarizing beam splitters plays in partial Bell state analyzers for polarization qubits. The additional channels entering both multiplexing blocks (gray lines) serve to highlight that peripheral network traffic is not hindered. (b) High-level concept illustration showing the action of frequency beam splitters (Hadamard transformations H_0, H_1) on different spectral modes. Here gray lines highlight the presence of frequency correlations between frequency bins.

presented earlier [144] [**Fig. 4.7**]. Just as the $50:50$ (spatial) beam splitter performs a pairwise mixing of polarization modes (H_A with H_B and V_A with V_B), likewise frequency beam splitters (Hadamard transformations H_0 and H_1 in **Fig. 4.10(b)**) implemented using a quantum frequency processor (QFP) perform a pairwise mixing of frequency modes – A_0 with B_0 and A_1 with B_1. This mode mixing is followed by demultiplexing all the distinct modes that can be populated – two possible polarization states in each of two possible paths in the case of a partial Bell state analyzer for polarization qubits. The equivalent operation in the frequency domain (for photonic frequency qubits) is spectral filtering. As with the spatial analog, only the $|\psi^+\rangle$ and $|\psi^-\rangle$ Bell states can be identified without ambiguity.

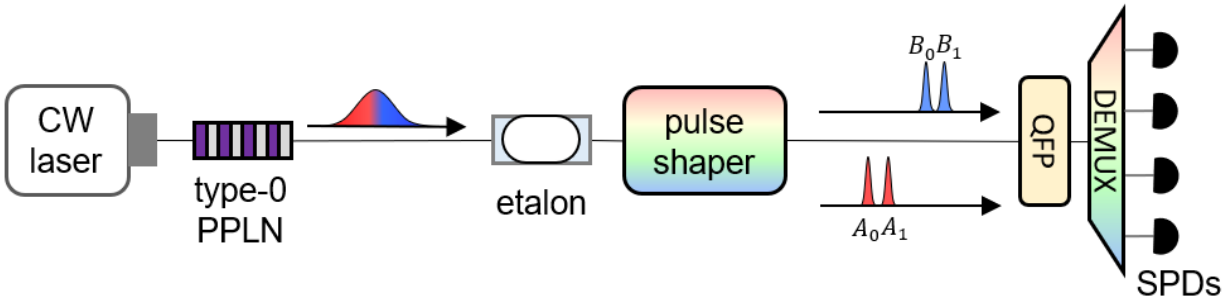

Figure 4.11. Experimental setup for validating the frequency domain Bell state analyzer. A continuous-wave (CW) laser pumps a periodically-poled lithium niobate waveguide engineered for type-0 phase matching. The broadband biphoton is passed to an etalon and pulse shaper to prepare the $|\psi^+\rangle$ and $|\psi^-\rangle$ frequency-bin Bell states. A three-element QFP (electro-optic modulator – pulse shaper – electro-optic modulator) implements frequency beam splitters that carry out pairwise mixing of frequency modes (A_0 with B_0 and A_1 with B_1), which are subsequently demultiplexed for spectrally-resolved coincidence measurements.

We validate the operation of our frequency mixing-based BSA in a manner to akin to that in Mattle *et al.* [144] by demonstrating that the outcome of a joint measurement on a known Bell state always belongs to a set of two-photon events unique that Bell state. **Figure 4.11** shows our experimental setup. Broadband time-frequency entangled photons are generated by pumping a periodically-poled lithium niobate ridge waveguide (PPLN) engineered for type-0 down-conversion with a continuous-wave laser at ~ 780 nm. An etalon with a 20 GHz free spectral range, coupled with a pulse shaper, carves four energy-correlated frequency modes (A_0, A_1, B_0, B_1) to project the biphoton onto state $|\psi^{\pm}\rangle \propto |1\rangle_{A0}|1\rangle_{B1} \pm |1\rangle_{A1}|1\rangle_{B0}$. The choice of the $|\psi^+\rangle$ or $|\psi^-\rangle$ state is determined by the joint phase applied to $|1\rangle_{A1}|1\rangle_{B0}$ by the pulse shaper. The center-to-center separation between signal and idler is 40 GHz while the two modes in each computational space are 20 GHz apart with an intensity full width at half-maximum of 0.8 GHz.

Parallel and interleaved Hadamard transformations are implemented with a quantum frequency processor (QFP) [30]. **Figure 4.12(a)** shows mode transformation spectra from experiments with classical light. The output of the QFP is frequency demultiplexed (DE-

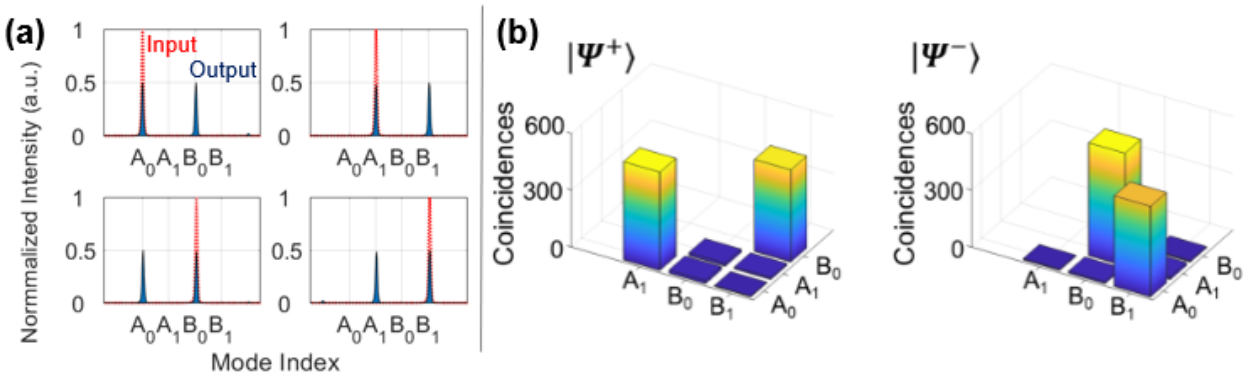

Figure 4.12. (a) Mode transformation spectra from experiments with classical light. The left two spectra correspond to Hadamard transformation H_0, which splits an input light field between modes A_0 and B_0. The right two spectra correspond to Hadamard transformation H_1, which splits an input light field between modes $A1$ and $B1$. (b) Coincidences patterns for the the $|\psi^+\rangle$ and $|\psi^-\rangle$ showing discrimination accuracies of 98.1% and 98.6%, respectively.

MUX, **Fig.** 4.11) by another pulse shaper so that different frequency modes are routed to two superconducting nanowire single-photon detectors (SPDs, **Fig.** 4.11). Coincidence counts for all 6 unique detector combinations (excluding A_0A_0, A_1A_1, B_0B_0 and B_1B_1) are integrated over a 1.5 ns window for a total of 120 seconds.

Experimental results are presented in **Figure 4.12(b)**. For the $|\psi^+\rangle$ state coincidences register between frequencies corresponding to the original idler modes (A_0 and A_1) or the two original signal modes (B_0 and B_1), as expected from theory [144]. On the other hand, the $|\psi^-\rangle$ state results in coincidences between one of the original idler modes with one of the original signal modes (events A_0B_1 or A_1B_0), thereby allowing one to unambiguously distinguish $|\psi^+\rangle$ from $|\psi^-\rangle$. We calculate the discrimination accuracy N_c/N_T, where N_c and N_T correspond to the sum of correct measurement results and the sum of all events identifiable as $|\psi^+\rangle$ or $|\psi^-\rangle$. We achieve accuracies of 98.1% and 98.6% for $|\psi^+\rangle$ and $|\psi^-\rangle$, respectively, which are reported without accidental subtraction. We did not examine the $|\phi^\pm\rangle$ Bell states experimentally, which would correspond to positive frequency correlations in our logical encoding. While this class of Bell states can be identified by observation of photon bunching, the $|\phi^+\rangle$ and the $|\phi^-\rangle$ states cannot be unambiguously distinguished from

one another, which ultimately limits the optimal efficiency of standard, vacuum-assisted linear optics BSAs to 50% [142].

4.2.4 Implications for Network Architecture and Design

From the standpoint of performance, previous work has shown that a three-element QFP can implement near-deterministic frequency beam splitters with gate fidelities exceeding 0.999999 [148]. Furthermore, this paradigm permits massive parallelization of quantum operations in a single device without any crosstalk and, most importantly, within a single fiber-optic spatial mode, thereby enabling natural phase stability. One limitation of this approach is that its versatility is limited by the performance of discrete components. In particular, the resolution of commercial pulse shapers limits the separation between frequency modes to 20 GHz. Conversely, the bandwidth of available radiofrequency electronics limits how far apart photons can be in frequency – about 40-50 GHz. A critical step to working with spectrally multiplexed quantum channels is migration of the QFP paradigm to an integrated optical platform, which has the potential to not only lower optical loss, but also boost the complexity of quantum operations without any increase to the analog bandwidth required by the system.

Our demonstration represents an important step toward the long-term vision of a quantum internet compatible with both heterogeneous nodes and dense spectral multiplexing. While the specific BSA realized here operated on frequency-bin-entangled photons, i.e., frequency qubits, the concept is easily extended to spectrally distinguishable photons encoded in other degrees of freedom. For spectrally distinguishable polarization qubits, one would need to implement two frequency beam splitters within a polarization diversity scheme [79] and for time-bin qubits a single frequency beam splitter would suffice. Moreover, the QFP paradigm is not the only way to synthesize BSAs based on frequency mixing. In addition to probabilistic frequency interference with a single modulator – used in previous implementations of single-photon entanglement swapping protocols [149] – one can also realize these operations in integrated optical components like coupled-cavity electro-optic modulators [91] or rely on techniques like Bragg scattering four-wave mixing [31] to bridge large

frequency differences. Irrespective of the particular physical implementation, BSAs based on frequency mixing have the potential to support heterogeneous nodes and/or spectral multiplexing on quantum networks without imposing additional limits on entanglement fidelity or the entanglement generation rate.

5. SUMMARY

5.1 Outlook

Quantum information processing in the frequency domain is a relatively new field with much of the progress occurring over the last $3-4$ years. Nonetheless, these developments have garnered the attention of the broader community as evidenced by recent review articles on quantum frequency combs [51] and high-dimensional entanglement [21]. What makes frequency-encoded or frequency-entangled states particularly attractive, as a matter of fundamental interest, is that they can support many temporal and frequency modes; high dimensionality and hyperentanglement can potentially offer a large quantum resource over just a few photons. Recent accomplishments include characterization of high-dimensional frequency-bin entanglement [48], [49], demonstration of a universal gate set [35], [36], single-photon two qudit gates [43], [55], generation of four-party 32-dimensional Greenberger-Horne-Zeilinger states [43], and nonlocal delay metrology featuring picosecond-scale resolution with potential relevance to network synchronization [150].

We complement this body of work by making use of frequency multiplexing and frequency transformations to support functionality needed for quantum networks. In particular, we leveraged flex grid technology to demonstrate reconfigurable distribution of quantum entanglement in a four-user tabletop network [132]. Our scalable approach introduces loss that is fixed with the number of users, offering a practical path for the establishment and management of quality-of-service guarantees in large quantum networks. We subsequently examined a potential obstacle to scaling up networking protocols – their reliance on Bell state measurements, which fundamentally limits network performance when joint measurements are between spectrally distinguishable channels. To overcome the tension between wavelength-multiplexed quantum state transport and high-fidelity entanglement generation, we synthesized the first Bell state analyzer that operates directly on frequency mismatch through the use of interleaved frequency beamsplitters [75], [76]. These results offer a path to Bell state measurements with spectrally distinguishable photons without the need for time-resolved detection or active feedfoward. Finally, we found favorable scaling for high-dimensional discrete Fourier transform gates with the number of RF harmonics when im-

plemented on a three-element QFP [Fig. 3.9]. Collectively, this recent progress is perhaps most relevant to the development of quantum interconnects [94], which would benefit from the ability to implement high-dimensional gates, work with spectrally multiplexed quantum channels, and carry out in-band quantum frequency conversion.

5.2 Future Directions

We are still many years away from the long-term vision of fault-tolerant quantum networks. However, the areas of quantum computing and quantum key distribution are perhaps showing some signs of market pull and strong government or industry investment. The tools we have developed to manipulate photon frequency can directly impact both areas.

5.2.1 Spectrally Multiplexed Quantum Repeaters

Based on the work presented in the previous section, one can imagine a framework for quantum repeaters based on spectral multiplexing [**Fig. 5.1**]. In this concept illustration, a nonlinear crystal generates broadband entangled photons, which are passed to a wavelength-selective switch (WSS) that carves the spectrum into a series of energy-matched spectral slices. One half of the biphoton spectrum is directed to an array of spatial beam splitters (parallel BSA array) for conventional Bell state measurements and the other half of the spectrum is directed to broadband quantum memories. Detection results, or lack thereof, are fed to the quantum memory and frequency mixing-based BSA (f-BSA) so that joint measurements, after release of photons from memories, result in high-efficiency entanglement swapping across the desired link. A logical pivot in this direction might be to explore the possibility of programmably entangling arbitrary pairs of matter-based qubits over a multi-user network. In addition, the use of highly nondegenrate photon pair sources may enable translation to telecom wavelengths via entanglement swapping operations that, in practical scenarios, may be more efficient than is possible with current methods of quantum frequency conversion.

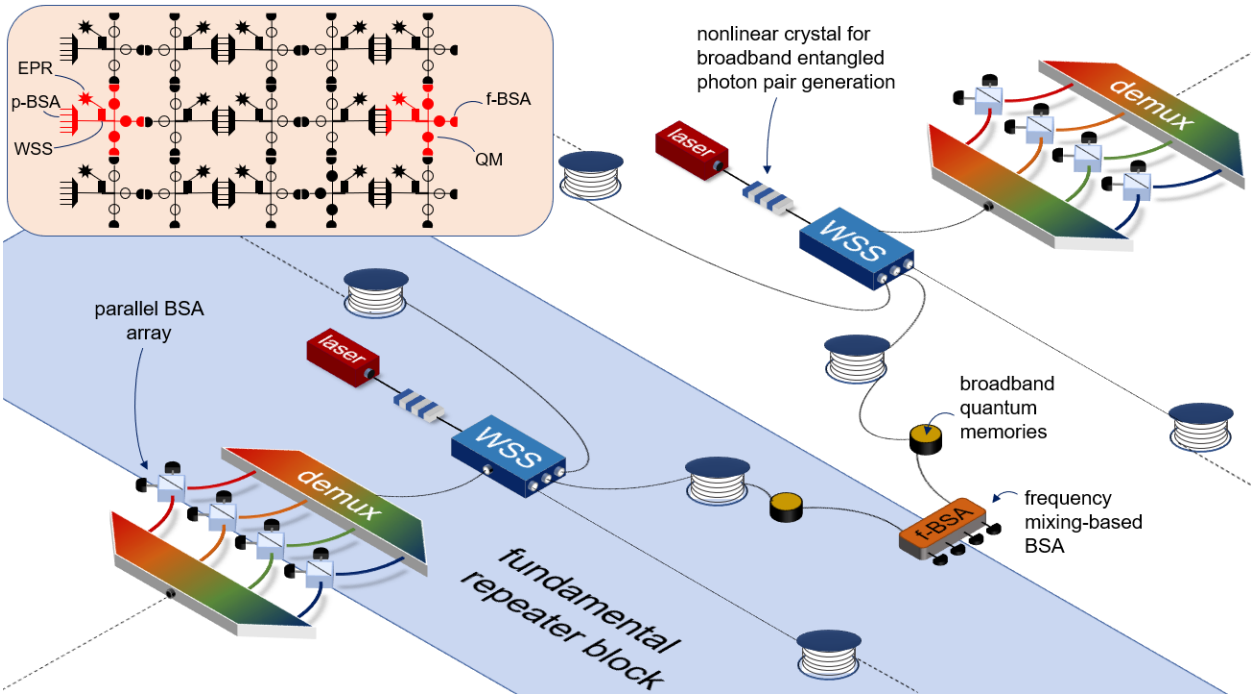

Figure 5.1. Concept illustration of a spectrally-multiplexed quantum repeater block. Inset: Network architecture based on fundamental repeater block.

5.2.2 In-band Quantum Frequency Conversion

Spectral transformations implemented on a quantum processor offer a potential solution to the challenge of in-band quantum frequency conversion. By performing all operations optically, the quantum state is preserved throughout; yet the specific manipulations are electrically controlled, making them extremely reliable and adding no optical noise. In this context, the quantum frequency processor can provide well-controlled operations within a specific band, allowing channels to swap wavelengths simultaneously up to high dimensions, thereby facilitating agile wavelength routing in quantum networks with nanosecond update speeds.

5.2.3 Photonic Micorosystems Development

The applicability of electro-optic frequency mixing techniques to quantum technology will rise of fall with progress in integrated photonics. In particular, the reliance on mod-

ulators to perform fundamental operations means that dramatic reductions in optical loss, and possibly modulation bandwidth, are required in practical use scenarios. Fortunately, frequency bin quantum photonics has synergies with fields that are the subject of significant research and development interest – Kerr microcombs, radiofrequency photonics, and high-performance computing. Quantum frequency combs, like their classical counterparts, can be generated in nonlinear microresonators with low anomalous group velocity dispersion. Scalable production of these sources would make this platform readily accessible to the wider research community. Similarly, progress in high-performance computing and wideband communications hinges on the development of high-speed, low-loss optical switches, which differ from low-loss phase modulators only by a scaling of the device length. With continued progress it should be possible to translate research output into widely-available components with performance acceptable for quantum applications.

REFERENCES

[1] F. Arute, K. Arya, R. Babbush, D. Bacon, J. C. Bardin, R. Barends, R. Biswas, S. Boixo, F. G. Brandao, D. A. Buell, B. Burkett, Y. Chen, Z. Chen, B. Chiaro, R. Collins, W. Courtney, A. Dunsworth, E. Farhi, B. Foxen, A. Fowler, C. Gidney, M. Giustina, R. Graff, K. Guerin, S. Habegger, M. P. Harrigan, M. J. Hartmann, A. Ho, M. Hoffmann, T. Huang, T. S. Humble, S. V. Isakov, E. Jeffrey, Z. Jiang, D. Kafri, K. Kechedzhi, J. Kelly, P. V. Klimov, S. Knysh, A. Korotkov, F. Kostritsa, D. Landhuis, M. Lindmark, E. Lucero, D. Lyakh, S. Mandrà, J. R. McClean, M. McEwen, A. Megrant, X. Mi, K. Michielsen, M. Mohseni, J. Mutus, O. Naaman, M. Neeley, C. Neill, M. Y. Niu, E. Ostby, A. Petukhov, J. C. Platt, C. Quintana, E. G. Rieffel, P. Roushan, N. C. Rubin, D. Sank, K. J. Satzinger, V. Smelyanskiy, K. J. Sung, M. D. Trevithick, A. Vainsencher, B. Villalonga, T. White, Z. J. Yao, P. Yeh, A. Zalcman, H. Neven, and J. M. Martinis, "Quantum supremacy using a programmable superconducting processor," *Nature*, vol. 574, no. 7779, pp. 505–510, 2019, ISSN: 14764687. DOI: 10.1038/s41586-019-1666-5.

[2] H. S. Zhong, H. Wang, Y. H. Deng, M. C. Chen, L. C. Peng, Y. H. Luo, J. Qin, D. Wu, X. Ding, Y. Hu, P. Hu, X. Y. Yang, W. J. Zhang, H. Li, Y. Li, X. Jiang, L. Gan, G. Yang, L. You, Z. Wang, L. Li, N. L. Liu, C. Y. Lu, and J. W. Pan, "Quantum computational advantage using photons," *Science*, vol. 370, no. 6523, pp. 1460–1463, 2021, ISSN: 10959203. DOI: 10.1126/science.abe8770. arXiv: 2012.01625.

[3] N. Gisin, G. Ribordy, W. Tittel, and H. Zbinden, "Quantum cryptography," *Reviews of Modern Physics*, vol. 74, pp. 145–195, 2002. DOI: 10.1103/RevModPhys.74.145.

[4] D. Gottesman, T. Jennewein, and S. Croke, "Longer-baseline telescopes using quantum repeaters," *Phys. Rev. Lett.*, vol. 109, p. 070 503, 7 2012. DOI: 10.1103/PhysRevLett.109.070503.

[5] P. Kómár, E. M. Kessler, M. Bishof, L. Jiang, A. S. Sørensen, J. Ye, and M. D. Lukin, "A quantum network of clocks," *Nature Physics*, vol. 10, no. 8, pp. 582–587, 2014, ISSN: 17452481. DOI: 10.1038/nphys3000.

[6] E. O. Ilo-Okeke, L. Tessler, J. P. Dowling, and T. Byrnes, "Remote quantum clock synchronization without synchronized clocks," *npj Quantum Information*, vol. 4, p. 40, 2018, ISSN: 20566387. DOI: 10.1038/s41534-018-0090-2.

[7] T. D. Ladd, F. Jelezko, R. Laflamme, Y. Nakamura, C. Monroe, and J. L. O'Brien, "Quantum computers," *Nature*, vol. 464, pp. 45–53, 2010, ISSN: 00280836. DOI: 10.1038/nature08812.

[8] F. Lecocq, F. Quinlan, K. Cicak, J. Aumentado, S. A. Diddams, and J. D. Teufel, "Control and readout of a superconducting qubit using a photonic link," *Nature*, vol. 591, no. 7851, pp. 575–579, 2021, ISSN: 0028-0836. DOI: 10.1038/s41586-021-03268-x.

[9] C. Monroe, R. Raussendorf, A. Ruthven, K. R. Brown, P. Maunz, L. M. Duan, and J. Kim, "Large-scale modular quantum-computer architecture with atomic memory and photonic interconnects," *Physical Review A - Atomic, Molecular, and Optical Physics*, vol. 89, no. 2, p. 022 317, 2014, ISSN: 10502947. DOI: 10.1103/PhysRevA.89.022317.

[10] S. Pirandola and S. L. Braunstein, "Comment: Unite to build a quantum Internet," vol. 532, no. 7598, pp. 169–171, Apr. 2016, ISSN: 14764687. DOI: 10.1038/532169a.

[11] J.-W. Pan, Z.-B. Chen, C.-Y. Lu, H. Weinfurter, A. Zeilinger, and M. Żukowski, "Multiphoton entanglement and interferometry," *Reviews of Modern Physics*, vol. 84, pp. 777–838, 2012. DOI: 10.1103/RevModPhys.84.777.

[12] A. Treiber, A. Poppe, M. Hentschel, D. Ferrini, T. Lorünser, E. Querasser, T. Matyus, H. Hübel, and A. Zeilinger, "A fully automated entanglement-based quantum cryptography system for telecom fiber networks," *New J. Phys.*, vol. 11, no. 4, p. 045 013, Apr. 2009.

[13] J. T. Barreiro, T.-C. Wei, and P. G. Kwiat, "Beating the channel capacity limit for linear photonic superdense coding," *Nature Physics*, vol. 4, pp. 282–286, 2008. DOI: 10.1038/nphys919.

[14] D. Bouwmeester, J. W. Pan, K. Mattle, M. Eibl, H. Weinfurter, and A. Zeilinger, "Experimental quantum teleportation," *Nature*, vol. 390, no. 6660, pp. 575–579, 1997, ISSN: 00280836. DOI: 10.1038/37539.

[15] J.-W. Pan, D. Bouwmeester, H. Weinfurter, and A. Zeilinger, "Experimental entanglement swapping: Entangling photons that never interacted," *Phys. Rev. Lett.*, vol. 80, pp. 3891–3894, 18 1998. DOI: 10.1103/PhysRevLett.80.3891.

[16] F. Steinlechner, S. Ecker, M. Fink, B. Liu, J. Bavaresco, M. Huber, T. Scheidl, and R. Ursin, "Distribution of high-dimensional entanglement via an intra-city free-space link," *Nature Communications*, vol. 8, p. 15 971, 2017, ISSN: 20411723. DOI: 10.1038/ncomms15971.

[17] S. K. Liao, W. Q. Cai, W. Y. Liu, L. Zhang, Y. Li, J. G. Ren, J. Yin, Q. Shen, Y. Cao, Z. P. Li, F. Z. Li, X. W. Chen, L. H. Sun, J. J. Jia, J. C. Wu, X. J. Jiang, J. F. Wang, Y. M. Huang, Q. Wang, Y. L. Zhou, L. Deng, T. Xi, L. Ma, T. Hu, Q. Zhang, Y. A. Chen, N. L. Liu, X. B. Wang, Z. C. Zhu, C. Y. Lu, R. Shu, C. Z. Peng, J. Y. Wang, and J. W. Pan, "Satellite-to-ground quantum key distribution," *Nature*, vol. 549, pp. 43–47, 2017, ISSN: 14764687. DOI: 10.1038/nature23655.

[18] F. Flamini, N. Spagnolo, and F. Sciarrino, "Photonic quantum information processing: a review," *Reports on Progress in Physics*, vol. 82, p. 016 001, 2019, ISSN: 0034-4885. DOI: 10.1088/1361-6633/AAD5B2.

[19] G. P. Agrawal, *Fiber-Optic Communication Systems*, 4th. John Wiley Sons, Inc., Oct. 2010, ISBN: 9780470505113. DOI: 10.1002/9780470918524.

[20] P. Marin-Palomo, J. N. Kemal, M. Karpov, A. Kordts, J. Pfeifle, M. H. P. Pfeiffer, P. Trocha, S. Wolf, V. Brasch, M. H. Anderson, R. Rosenberger, K. Vijayan, W. Freude, T. J. Kippenberg, and C. Koos, "Microresonator-based solitons for massively parallel coherent optical communications," *Nature*, vol. 546, no. 7657, pp. 274–279, 2017, ISSN: 0028-0836. DOI: 10.1038/nature22387.

[21] M. Erhard, M. Krenn, and A. Zeilinger, "Advances in high-dimensional quantum entanglement," *Nature Reviews Physics*, vol. 2, pp. 365–381, 2020, ISSN: 25225820. DOI: 10.1038/s42254-020-0193-5.

[22] W. K. Wootters and W. H. Zurek, "A single quantum cannot be cloned," *Nature*, vol. 299, no. 5886, pp. 802–803, 1982, ISSN: 00280836. DOI: 10.1038/299802a0.

[23] H. J. Briegel, W. Dür, J. I. Cirac, and P. Zoller, "Quantum repeaters: The role of imperfect local operations in quantum communication," *Physical Review Letters*, vol. 81, no. 26, pp. 5932–5935, 1998, ISSN: 10797114. DOI: 10.1103/PhysRevLett.81.5932.

[24] N. Sangouard, C. Simon, H. De Riedmatten, and N. Gisin, "Quantum repeaters based on atomic ensembles and linear optics," *Reviews of Modern Physics*, vol. 83, no. 1, pp. 33–80, 2011, ISSN: 00346861. DOI: 10.1103/RevModPhys.83.33.

[25] O. A. Collins, S. D. Jenkins, A. Kuzmich, and T. A. Kennedy, "Multiplexed memory-insensitive quantum repeaters," *Physical Review Letters*, vol. 98, p. 060 502, 2007, ISSN: 00319007. DOI: 10.1103/PhysRevLett.98.060502.

[26] N. Sinclair, E. Saglamyurek, H. Mallahzadeh, J. A. Slater, M. George, R. Ricken, M. P. Hedges, D. Oblak, C. Simon, W. Sohler, and W. Tittel, "Spectral multiplexing for scalable quantum photonics using an atomic frequency comb quantum memory and feed-forward control," *Physical Review Letters*, vol. 113, no. 5, p. 053 603, 2014, ISSN: 10797114. DOI: 10.1103/PhysRevLett.113.053603.

[27] D. E. Jones, B. T. Kirby, and M. Brodsky, "Tuning quantum channels to maximize polarization entanglement for telecom photon pairs," *npj Quantum Information*, vol. 4, p. 58, 2018. DOI: 10.1038/s41534-018-0107-x.

[28] M. Erhard, R. Fickler, M. Krenn, and A. Zeilinger, "Twisted photons: New quantum perspectives in high dimensions," *Light: Science and Applications*, vol. 7, p. 17 146, 2018, ISSN: 20477538. DOI: 10.1038/lsa.2017.146.

[29] L.-M. Duan and C. Monroe, "Colloquium : Quantum networks with trapped ions," *Reviews of Modern Physics*, vol. 82, no. 2, pp. 1209–1224, 2010. DOI: 10.1103/RevModPhys.82.1209.

[30] H.-H. Lu, J. M. Lukens, N. A. Peters, O. D. Odele, D. E. Leaird, A. M. Weiner, and P. Lougovski, "Electro-Optic Frequency Beam Splitters and Tritters for High-Fidelity Photonic Quantum Information Processing," *Physical Review Letters*, vol. 120, no. 3, p. 030 502, 2018. DOI: 10.1103/PhysRevLett.120.030502.

[31] C. Joshi, A. Farsi, A. Dutt, B. Y. Kim, X. Ji, Y. Zhao, A. M. Bishop, M. Lipson, and A. L. Gaeta, "Frequency-Domain Quantum Interference with Correlated Photons from an Integrated Microresonator," *Physical Review Letters*, vol. 124, p. 143 601, 2020, ISSN: 10797114. DOI: 10.1103/PhysRevLett.124.143601.

[32] J. M. Lukens and P. Lougovski, "Frequency-encoded photonic qubits for scalable quantum information processing," *Optica*, vol. 4, no. 1, pp. 8–16, 2017. DOI: 10.1364/OPTICA.4.000008.

[33] A. M. Weiner, "Femtosecond pulse shaping using spatial light modulators," *Review of Scientific Instruments*, vol. 71, p. 1929, 2000. DOI: 10.1063/1.1150614.

[34] A. M. Weiner, "Ultrafast optical pulse shaping: A tutorial review," *Opt. Commun.*, vol. 284, no. 15, pp. 3669–3692, 2011, ISSN: 0030-4018. DOI: 10.1016/j.optcom.2011.03.084.

[35] H.-H. Lu, J. M. Lukens, N. A. Peters, B. P. Williams, A. M. Weiner, and P. Lougovski, "Quantum interference and correlation control of frequency-bin qubits," *Optica*, vol. 5, no. 11, pp. 1455–1460, 2018. DOI: 10.1364/OPTICA.5.001455.

[36] H.-H. Lu, J. M. Lukens, B. P. Williams, P. Imany, N. A. Peters, A. M. Weiner, and P. Lougovski, "A controlled-NOT gate for frequency-bin qubits," *npj Quantum Information*, vol. 5, p. 24, 2019.

[37] J. Wang, S. Paesani, Y. Ding, R. Santagati, P. Skrzypczyk, A. Salavrakos, J. Tura, R. Augusiak, L. Mančinska, D. Bacco, D. Bonneau, J. W. Silverstone, Q. Gong, A. Acín, K. Rottwitt, L. K. Oxenløwe, J. L. O'Brien, A. Laing, and M. G. Thompson, "Multidimensional quantum entanglement with large-scale integrated optics," *Science*, vol. 360, no. 6386, pp. 285–291, 2018, ISSN: 10959203. DOI: 10.1126/science.aar7053.

[38] X. Qiang, X. Zhou, J. Wang, C. M. Wilkes, T. Loke, S. O'Gara, L. Kling, G. D. Marshall, R. Santagati, T. C. Ralph, J. B. Wang, J. L. O'Brien, M. G. Thompson, and J. C. Matthews, "Large-scale silicon quantum photonics implementing arbitrary two-qubit processing," *Nature Photonics*, vol. 12, no. 9, pp. 534–539, 2018, ISSN: 17494893. DOI: 10.1038/s41566-018-0236-y.

[39] H. J. Lee, S. K. Choi, and H. S. Park, "Experimental Demonstration of Four-Dimensional Photonic Spatial Entanglement between Multi-core Optical Fibres," *Scientific Reports*, vol. 7, no. 1, pp. 1–8, 2017, ISSN: 20452322. DOI: 10.1038/s41598-017-04444-8.

[40] M. Krenn, M. Huber, R. Fickler, R. Lapkiewicz, S. Ramelow, and A. Zeilinger, "Generation and confirmation of a (100×100)-dimensional entangled quantum system," *Proceedings of the National Academy of Sciences of the United States of America*, vol. 111, no. 17, pp. 6243–6247, 2014, ISSN: 10916490. DOI: 10.1073/pnas.1402365111.

[41] F. Brandt, M. Hiekkamäki, F. Bouchard, M. Huber, and R. Fickler, "High-dimensional quantum gates using full-field spatial modes of photons," *Optica*, vol. 7, no. 2, p. 98, 2020, ISSN: 2334-2536. DOI: 10.1364/optica.375875.

[42] H. Cao, S.-C. Gao, C. Zhang, J. Wang, D.-Y. He, B.-H. Liu, Z.-W. Zhou, Y.-J. Chen, Z.-H. Li, S.-Y. Yu, J. Romero, Y.-F. Huang, C.-F. Li, and G.-C. Guo, "Distribution of high-dimensional orbital angular momentum entanglement over a 1 km few-mode fiber," *Optica*, vol. 7, no. 3, p. 232, 2020, ISSN: 2334-2536. DOI: 10.1364/optica.381403.

[43] P. Imany, J. A. Jaramillo-Villegas, M. S. Alshaykh, J. M. Lukens, O. D. Odele, A. J. Moore, D. E. Leaird, M. Qi, and A. M. Weiner, "High-dimensional optical quantum logic in large operational spaces," *npj Quantum Information*, vol. 5, no. 1, Article number: 59, 2019. DOI: 10.1038/s41534-019-0173-8.

[44] A. Martin, T. Guerreiro, A. Tiranov, S. Designolle, F. Fröwis, N. Brunner, M. Huber, and N. Gisin, "Quantifying Photonic High-Dimensional Entanglement," *Physical Review Letters*, vol. 118, no. 11, p. 110 501, 2017, ISSN: 10797114. DOI: 10.1103/PhysRevLett.118.110501.

[45] T. Ikuta and H. Takesue, "Implementation of quantum state tomography for time-bin qudits," *New Journal of Physics*, vol. 19, no. 1, p. 013 039, 2017, ISSN: 13672630. DOI: 10.1088/1367-2630/aa5571.

[46] T. Ikuta and H. Takesue, "Four-dimensional entanglement distribution over 100 km," *Scientific Reports*, vol. 8, no. 1, pp. 1–7, 2018, ISSN: 20452322. DOI: 10.1038/s41598-017-19078-z.

[47] "Frequency-Multiplexed Photon Pairs over 1000 Modes from a Quadratic Nonlinear Optical Waveguide Resonator with a Singly Resonant Configuration," *Physical Review Letters*, vol. 123, no. 19, p. 193 603, 2019, ISSN: 10797114. DOI: 10.1103/PhysRevLett.123.193603.

[48] P. Imany, J. A. Jaramillo-Villegas, O. D. Odele, K. Han, D. E. Leaird, J. M. Lukens, P. Lougovski, M. Qi, and A. M. Weiner, "50-GHz-spaced comb of high-dimensional frequency-bin entangled photons from an on-chip silicon nitride microresonator," *Optics Express*, vol. 26, no. 2, pp. 1825–1840, 2018. DOI: 10.1364/OE.26.001825.

[49] M. Kues, C. Reimer, P. Roztocki, L. R. Cortés, S. Sciara, B. Wetzel, Y. Zhang, A. Cino, S. T. Chu, B. E. Little, D. J. Moss, L. Caspani, J. Azaña, and R. Morandotti, "On-chip generation of high-dimensional entangled quantum states and their coherent control," *Nature*, vol. 546, pp. 622–626, 2017. DOI: 10.1038/nature22986.

[50] H.-H. Lu, B. Qi, B. P. Williams, P. Lougovski, A. M. Weiner, and J. M. Lukens, "Agile frequency transformations for dense wavelength-multiplexed communications," *Optics Express*, vol. 28, no. 14, p. 20 390, 2020, ISSN: 1094-4087. DOI: 10.1364/oe.396142.

[51] M. Kues, C. Reimer, J. M. Lukens, W. J. Munro, A. M. Weiner, D. J. Moss, and R. Morandotti, "Quantum optical microcombs," *Nature Photonics*, vol. 13, pp. 170–179, 2019. DOI: 10.1038/s41566-019-0363-0.

[52] P. Imany, O. D. Odele, J. A. Jaramillo-Villegas, D. E. Leaird, and A. M. Weiner, "Characterization of coherent quantum frequency combs using electro-optic phase modulation," *Physical Review A*, vol. 97, p. 013 813, 2018. DOI: 10.1103/PhysRevA.97.013813.

[53] L. Olislager, J. Cussey, A. T. Nguyen, P. Emplit, S. Massar, J. M. Merolla, and K. P. Huy, "Frequency-bin entangled photons," *Physical Review A - Atomic, Molecular, and Optical Physics*, vol. 82, no. 1, p. 013 804, 2010, ISSN: 10502947. DOI: 10.1103/PhysRevA.82.013804.

[54] N. R. Newbury, "Searching for applications with a fine-tooth comb," *Nature photonics*, vol. 5, pp. 186–188, 2011. DOI: 10.1038/nphoton.2011.38.

[55] C. Reimer, S. Sciara, P. Roztocki, M. Islam, L. Romero Cortés, Y. Zhang, B. Fischer, S. Loranger, R. Kashyap, A. Cino, S. T. Chu, B. E. Little, D. J. Moss, L. Caspani, W. J. Munro, J. Azaña, M. Kues, and R. Morandotti, "High-dimensional one-way quantum processing implemented on d-level cluster states," *Nature Physics*, vol. 15, no. 2, pp. 148–153, 2019. DOI: 10.1038/s41567-018-0347-x.

[56] A. Pe'er, B. Dayan, A. A. Friesem, and Y. Silberberg, "Temporal shaping of entangled photons," *Physical Review Letters*, vol. 94, no. 7, p. 073 601, 2005, ISSN: 00319007. DOI: 10.1103/PhysRevLett.94.073601.

[57] X. Guo, Y. Mei, and S. Du, "Testing the Bell inequality on frequency-bin entangled photon pairs using time-resolved detection," *Optica*, vol. 4, no. 4, pp. 388–392, 2017, ISSN: 2334-2536. DOI: 10.1364/optica.4.000388.

[58] R. T. Thew, A. Acín, H. Zbinden, and N. Gisin, "Bell-type test of energy-time entangled qutrits," *Physical Review Letters*, vol. 93, no. 1, p. 010 503, 2004, ISSN: 00319007. DOI: 10.1103/PhysRevLett.93.010503.

[59] D. Collins, S. Popescu, D. Collins, S. Popescu, N. Gisin, N. Linden, and S. Massar, "Bell Inequalities for Arbitrarily High-Dimensional Systems," *Physical Review Letters*, vol. 88, no. 4, p. 040 404, 2002, ISSN: 10797114. DOI: 10.1103/PhysRevLett.88.040404.

[60] Z. Xie, T. Zhong, S. Shrestha, X. Xu, J. Liang, Y.-X. Gong, J. C. Bienfang, A. Restelli, J. H. Shapiro, F. N. C. Wong, and C. Wei Wong, "Harnessing high-dimensional hyperentanglement through a biphoton frequency comb," *Nature Photonics*, vol. 9, pp. 536–542, 2015. DOI: 10.1038/nphoton.2015.110.

[61] Y. J. Lu, R. L. Campbell, and Z. Y. Ou, "Mode-Locked Two-Photon States," *Physical Review Letters*, vol. 91, no. 16, p. 163 602, 2003. DOI: 10.1103/PhysRevLett.91.163602.

[62] N. B. Lingaraju, H. H. Lu, S. Seshadri, P. Imany, D. E. Leaird, J. M. Lukens, and A. M. Weiner, "Quantum frequency combs and Hong–Ou–Mandel interferometry: the role of spectral phase coherence," *Optics Express*, vol. 27, no. 26, pp. 38 683–38 697, 2019, ISSN: 23318422. DOI: 10.1364/oe.379749.

[63] A. M. Brańczyk, "Hong-Ou-Mandel Interference," Tech. Rep., Oct. 2017. arXiv: 1711.00080. [Online]. Available: http://arxiv.org/abs/1711.00080.

[64] P. Imany, N. B. Lingaraju, M. S. Alshaykh, D. E. Leaird, and A. M. Weiner, "Probing quantum walks through coherent control of high-dimensionally entangled photons," *Science Advances*, vol. 6, no. 29, eaba8066, 2020, ISSN: 23752548. DOI: 10.1126/sciadv.aba8066.

[65] A. Peruzzo, M. Lobino, J. C. Matthews, N. Matsuda, A. Politi, K. Poulios, X. Q. Zhou, Y. Lahini, N. Ismail, K. Wörhoff, Y. Bromberg, Y. Silberberg, M. G. Thompson, and J. L. OBrien, "Quantum walks of correlated photons," *Science*, vol. 329, no. 5998, pp. 1500–1503, 2010, ISSN: 00368075. DOI: 10.1126/science.1193515.

[66] A. Schreiber, A. Gábris, P. P. Rohde, K. Laiho, M. Štefaňák, V. Potoček, C. Hamilton, I. Jex, and C. Silberhorn, "A 2D quantum walk simulation of two-particle dynamics," *Science*, vol. 335, no. 6077, pp. 55–58, 2012, ISSN: 10959203. DOI: 10.1126/science.1218448.

[67] G. Di Giuseppe, L. Martin, A. Perez-Leija, R. Keil, F. Dreisow, S. Nolte, A. Szameit, A. F. Abouraddy, D. N. Christodoulides, and B. E. Saleh, "Einstein-podolsky-rosen spatial entanglement in ordered and anderson photonic lattices," *Physical Review Letters*, vol. 110, no. 15, p. 150 503, 2013, ISSN: 00319007. DOI: 10.1103/PhysRevLett.110.150503.

[68] J. Carolan, J. D. Meinecke, P. J. Shadbolt, N. J. Russell, N. Ismail, K. Wörhoff, T. Rudolph, M. G. Thompson, J. L. O'Brien, J. C. Matthews, and A. Laing, "On the experimental verification of quantum complexity in linear optics," *Nature Photonics*, vol. 8, pp. 621–626, 2014, ISSN: 17494893. DOI: 10.1038/nphoton.2014.152.

[69] T. Eichelkraut, C. Vetter, A. Perez-Leija, H. Moya-Cessa, D. N. Christodoulides, and A. Szameit, "Coherent random walks in free space," *Optica*, vol. 1, no. 4, p. 271, 2014, ISSN: 2334-2536. DOI: 10.1364/optica.1.000268.

[70] P. Imany, O. D. Odele, M. S. Alshaykh, H.-H. Lu, D. E. Leaird, and A. M. Weiner, "Frequency-domain Hong–Ou–Mandel interference with linear optics," *Optics Letters*, vol. 43, no. 12, pp. 2760–2763, 2018. DOI: 10.1364/OL.43.002760.

[71] H. Lu, N. B. Lingaraju, D. E. Leaird, A. M. Weiner, and J. M. Lukens, "Scaling the discrete fourier transform gate in the quantum frequency processor," in *Conference on Lasers and Electro-Optics*, Optical Society of America, 2020, FTu1N.8. DOI: 10.1364/CLEO_QELS.2021.FTu1N.8.

[72] J. Bavaresco, N. Herrera Valencia, C. Klöckl, M. Pivoluska, P. Erker, N. Friis, M. Malik, and M. Huber, "Measurements in two bases are sufficient for certifying high-dimensional entanglement," *Nature Physics*, vol. 14, no. 10, pp. 1032–1037, 2018, ISSN: 17452481. DOI: 10.1038/s41567-018-0203-z. arXiv: 1709.07344.

[73] C. Spengler, M. Huber, S. Brierley, T. Adaktylos, and B. C. Hiesmayr, "Entanglement detection via mutually unbiased bases," *Physical Review A*, vol. 86, no. 2, p. 022 311, 2012, ISSN: 10502947. DOI: 10.1103/PhysRevA.86.022311.

[74] J. M. Lukens, K. J. H. Law, A. Jasra, and P. Lougovski, "A practical and efficient approach for bayesian quantum state estimation," *New Journal of Physics*, vol. 22, no. 6, p. 063 038, Jul. 2020. DOI: 10.1088/1367-2630/ab8efa.

[75] N. B. Lingaraju, H. Lu, D. E. Leaird, S. B. Estrella, J. M. Lukens, and A. M. Weiner, "A Bell-state analyzer for photonic frequency," in *2020 IEEE Photonics Conference (IPC)*, 2020, paper PD5.

[76] N. B. Lingaraju, H. Lu, D. E. Leaird, S. B. Estrella, J. M. Lukens, and A. M. Weiner, "A programmable electro-optic bell-state analyzer for spectrally distinguishable photons," in *Conference on Lasers and Electro-Optics*, Optical Society of America, 2020, FTu1N.5. DOI: 10.1364/CLEO_QELS.2021.FTu1N.5.

[77] S. P. Walborn, S. Pádua, and C. H. Monken, "Hyperentanglement-assisted Bell-state analysis," *Physical Review A*, vol. 68, no. 4, p. 042 313, 2003. DOI: 10.1103/PhysRevA.68.042313.

[78] O. E. Sandoval, N. B. Lingaraju, P. Imany, D. E. Leaird, M. Brodsky, and A. M. Weiner, "Polarization diversity phase modulator for measuring frequency-bin entanglement of a biphoton frequency comb in a depolarized channel," *Opt. Lett.*, vol. 44, no. 7, pp. 1674–1677, Apr. 2019. DOI: 10.1364/OL.44.001674.

[79] N. B. Lingaraju, N. O'Malley, D. E. Jones, O. E. Sandoval, H. N. Azzouz, D. E. Leaird, J. M. Lukens, M. Brodsky, and A. M. Weiner, "Polarization diversity phase modulator for frequency-bin operations with hyperentangled biphoton frequency combs," in *Conference on Lasers and Electro-Optics*, Optical Society of America, 2020, FF1D.5. DOI: 10.1364/CLEO_QELS.2020.FF1D.5.

[80] F.-G. Deng, B.-C. Ren, and X.-H. Li, "Quantum hyperentanglement and its applications in quantum information processing," *Science Bulletin*, vol. 62, no. 1, pp. 46–68, 2017, ISSN: 2095-9273. DOI: https://doi.org/10.1016/j.scib.2016.11.007.

[81] D. S. Simon and A. V. Sergienko, "High-capacity quantum key distribution via hyperentangled degrees of freedom," *New Journal of Physics*, vol. 16, no. 6, p. 063 052, 2014. DOI: 10.1088/1367-2630/16/6/063052.

[82] C. Elliott, A. Colvin, D. Pearson, O. Pikalo, J. Schlafer, and H. Yeh, "Current status of the DARPA quantum network," in *Quantum Information and Computation III*, vol. 5815, SPIE, May 2005, pp. 138–150. DOI: 10.1117/12.606489.

[83] M. Peev, C. Pacher, R. Alléaume, C. Barreiro, J. Bouda, W. Boxleitner, T. Debuisschert, E. Diamanti, M. Dianati, J. F. Dynes, S. Fasel, S. Fossier, M. Fürst, J.-D. Gautier, O. Gay, N. Gisin, P. Grangier, A. Happe, Y. Hasani, M. Hentschel, H. Hübel, G. Humer, T. Länger, M. Legré, R. Lieger, J. Lodewyck, T. Lorünser, N. Lütkenhaus, A. Marhold, T. Matyus, O. Maurhart, L. Monat, S. Nauerth, J.-B. Page, A. Poppe, E. Querasser, G. Ribordy, S. Robyr, L. Salvail, A. W. Sharpe, A. J. Shields, D. Stucki, M. Suda, C. Tamas, T. Themel, R. T. Thew, Y. Thoma, A. Treiber, P. Trinkler, R. Tualle-Brouri, F. Vannel, N. Walenta, H. Weier, H. Weinfurter, I. Wimberger, Z. L. Yuan, H. Zbinden, and A. Zeilinger, "The SECOQC quantum key distribution network in Vienna," *New Journal of Physics*, vol. 11, p. 075 001, 2009. DOI: 10.1088/1367-2630/11/7/075001.

[84] T.-Y. Chen, J. Wang, H. Liang, W.-Y. Liu, Y. Liu, X. Jiang, Y. Wang, X. Wan, W.-Q. Cai, L. Ju, L.-K. Chen, L.-J. Wang, Y. Gao, K. Chen, C.-Z. Peng, Z.-B. Chen, and J.-W. Pan, "Metropolitan all-pass and inter-city quantum communication network," *Optics Express*, vol. 18, no. 26, pp. 27 217–27 225, 2010, ISSN: 1094-4087. DOI: 10.1364/oe.18.027217.

[85] M. Sasaki, M. Fujiwara, H. Ishizuka, W. Klaus, K. Wakui, M. Takeoka, S. Miki, T. Yamashita, Z. Wang, A. Tanaka, K. Yoshino, Y. Nambu, S. Takahashi, A. Tajima, A. Tomita, T. Domeki, T. Hasegawa, Y. Sakai, H. Kobayashi, T. Asai, K. Shimizu, T. Tokura, T. Tsurumaru, M. Matsui, T. Honjo, K. Tamaki, H. Takesue, Y. Tokura, J. F. Dynes, A. R. Dixon, A. W. Sharpe, Z. L. Yuan, A. J. Shields, S. Uchikoga, M. Legré, S. Robyr, P. Trinkler, L. Monat, J.-B. Page, G. Ribordy, A. Poppe, A. Allacher, O. Maurhart, T. Länger, M. Peev, and A. Zeilinger, "Field test of quantum key distribution in the Tokyo QKD Network," *Optics Express*, vol. 19, no. 11, pp. 10 387–10 409, 2011, ISSN: 1094-4087. DOI: 10.1364/oe.19.010387.

[86] S. Wang, W. Chen, Z.-Q. Yin, H.-W. Li, D.-Y. He, Y.-H. Li, Z. Zhou, X.-T. Song, F.-Y. Li, D. Wang, H. Chen, Y.-G. Han, J.-Z. Huang, J.-F. Guo, P.-L. Hao, M. Li, C.-M. Zhang, D. Liu, W.-Y. Liang, C.-H. Miao, P. Wu, G.-C. Guo, and Z.-F. Han, "Field and long-term demonstration of a wide area quantum key distribution network," *Optics Express*, vol. 22, no. 18, pp. 21 739–21 756, 2014, ISSN: 1094-4087. DOI: 10.1364/oe.22.021739.

[87] Q. Zhang, F. Xu, Y.-A. Chen, C.-Z. Peng, and J.-W. Pan, "Large scale quantum key distribution: challenges and solutions [Invited]," *Optics Express*, vol. 26, no. 18, pp. 24 260–24 273, 2018, ISSN: 1094-4087. DOI: 10.1364/oe.26.024260.

[88] P. G. Kwiat, E. Waks, A. G. White, I. Appelbaum, and P. H. Eberhard, "Ultrabright source of polarization-entangled photons," *Phys. Rev. A*, vol. 60, no. 2, R773–R776, 1999, ISSN: 1050-2947. DOI: 10.1103/physreva.60.r773.

[89] X. Li, P. L. Voss, J. E. Sharping, and P. Kumar, "Optical-fiber source of polarization-entangled photons in the 1550 nm telecom band," *Phys. Rev. Lett.*, vol. 94, p. 053 601, 5 2005. DOI: 10.1103/PhysRevLett.94.053601.

[90] E. Wooten, K. Kissa, A. Yi-Yan, E. Murphy, D. Lafaw, P. Hallemeier, D. Maack, D. Attanasio, D. Fritz, G. McBrien, and D. Bossi, "A review of lithium niobate modulators for fiber-optic communications systems," *IEEE Journal of Selected Topics in Quantum Electronics*, vol. 6, no. 1, pp. 69–82, 2000. DOI: 10.1109/2944.826874.

[91] Y. Hu, M. Yu, D. Zhu, N. Sinclair, A. Shams-Ansari, L. Shao, J. Holzgrafe, E. Puma, M. Zhang, and M. Loncar, "Reconfigurable electro-optic frequency shifter," *arXiv:2005.09621*, May 2020. arXiv: 2005.09621. [Online]. Available: http://arxiv.org/abs/2005.09621.

[92] E. Y. Zhu, Z. Tang, L. Qian, L. G. Helt, M. Liscidini, J. E. Sipe, C. Corbari, A. Canagasabey, M. Ibsen, and P. G. Kazansky, "Poled-fiber source of broadband polarization-entangled photon pairs," *Optics Letters*, vol. 38, no. 21, pp. 4397–4400, 2013, ISSN: 0146-9592. DOI: 10.1364/ol.38.004397.

[93] N. C. Harris, J. Carolan, D. Bunandar, M. Prabhu, M. Hochberg, T. Baehr-Jones, M. L. Fanto, A. M. Smith, C. C. Tison, P. M. Alsing, and D. Englund, "Linear programmable nanophotonic processors," *Optica*, vol. 5, no. 12, pp. 1623–1631, 2018. DOI: 10.1364/OPTICA.5.001623.

[94] D. Awschalom, K. K. Berggren, H. Bernien, S. Bhave, L. D. Carr, P. Davids, S. E. Economou, D. Englund, A. Faraon, M. Fejer, S. Guha, M. V. Gustafsson, E. Hu, L. Jiang, J. Kim, B. Korzh, P. Kumar, P. G. Kwiat, M. Lončar, M. D. Lukin, D. A. Miller, C. Monroe, S. W. Nam, P. Narang, J. S. Orcutt, M. G. Raymer, A. H. Safavi-Naeini, M. Spiropulu, K. Srinivasan, S. Sun, J. Vučković, E. Waks, R. Walsworth, A. M. Weiner, and Z. Zhang, "Development of Quantum Interconnects (QuICs) for Next-Generation Information Technologies," *PRX Quantum*, vol. 2, p. 017 002, 2021, ISSN: 2691-3399. DOI: 10.1103/PRXQuantum.2.017002.

[95] D. Onural, H. Gevorgyan, B. Zhang, A. Khilo, and M. A. Popović, "Ultra-high Q Resonators and Sub-GHz Bandwidth Second Order Filters in an SOI Foundry Platform," in *Optical Fiber Communication Conference (OFC) 2020, OSA Technical Digest (Optical Society of America, 2020)*, OSA, 2020, paper W1A.4, ISBN: 978-1-943580-71-2. DOI: 10.1364/OFC.2020.W1A.4.

[96] M. H. Khan, H. Shen, Y. Xuan, L. Zhao, S. Xiao, D. E. Leaird, A. M. Weiner, and M. Qi, "Ultrabroad-bandwidth arbitrary radiofrequency waveform generation with a silicon photonic chip-based spectral shaper," *Nature Photonics*, vol. 4, pp. 117–122, 2010. DOI: 10.1038/NPHOTON.2009.266.

[97] J. Wang, H. Shen, L. Fan, R. Wu, B. Niu, L. T. Varghese, Y. Xuan, D. E. Leaird, X. Wang, F. Gan, A. M. Weiner, and M. Qi, "Reconfigurable radio-frequency arbitrary waveforms synthesized in a silicon photonic chip," *Nature Communications*, vol. 6, p. 5957, 2015, ISSN: 2041-1723. DOI: 10.1038/ncomms6957.

[98] D. Dai, J. Bauters, and J. E. Bowers, "Passive technologies for future large-scale photonic integrated circuits on silicon: polarization handling, light non-reciprocity and loss reduction," *Light: Science Applications*, vol. 1, e1, 2012. DOI: 10.1038/lsa.2012.1.

[99] M. Zhang, C. Wang, R. Cheng, A. Shams-Ansari, and M. Lončar, "Monolithic ultra-high-Q lithium niobate microring resonator," *Optica*, vol. 4, no. 12, pp. 1536–1537, 2017. DOI: 10.1364/OPTICA.4.001536.

[100] Z. Yong, W. D. Sacher, Y. Huang, J. C. Mikkelsen, Y. Yang, X. Luo, P. Dumais, D. Goodwill, H. Bahrami, P. G.-Q. Lo, E. Bernier, and J. K. S. Poon, "Efficient Single-Drive Push-Pull Silicon Mach-Zehnder Modulators with U-Shaped PN Junctions for the O-Band," OSA, 2017, Tu2H.2, ISBN: 978-1-943580-23-1. DOI: 10.1364/OFC.2017.Tu2H.2.

[101] C. Kieninger, Y. Kutuvantavida, D. L. Elder, S. Wolf, H. Zwickel, M. Blaicher, J. N. Kemal, M. Lauermann, S. Randel, W. Freude, L. R. Dalton, and C. Koos, "Ultra-high electro-optic activity demonstrated in a silicon-organic hybrid modulator," *Optica*, vol. 5, no. 6, p. 739, 2018. DOI: 10.1364/OPTICA.5.000739.

[102] V. Sorianello, M. Midrio, G. Contestabile, I. Asselberghs, J. Van Campenhout, C. Huyghebaert, I. Goykhman, A. K. Ott, A. C. Ferrari, and M. Romagnoli, "Graphene-silicon phase modulators with gigahertz bandwidth," *Nature Photonics*, vol. 12, pp. 40–44, 2018, ISSN: 17494893. DOI: 10.1038/s41566-017-0071-6.

[103] P. O. Weigel, J. Zhao, K. Fang, H. Al-Rubaye, D. Trotter, D. Hood, J. Mudrick, C. Dallo, A. T. Pomerene, A. L. Starbuck, C. T. DeRose, A. L. Lentine, G. Rebeiz, and S. Mookherjea, "Bonded thin film lithium niobate modulator on a silicon photonics platform exceeding 100 GHz 3-dB electrical modulation bandwidth," *Optics Express*, vol. 26, no. 18, pp. 23 728–23 739, 2018. DOI: 10.1364/OE.26.023728.

[104] J. J. Van Der Tol, Y. Jiao, J. P. Van Engelen, V. Pogoretskiy, A. A. Kashi, and K. Williams, "InP Membrane on Silicon (IMOS) Photonics," *IEEE Journal of Quantum Electronics*, vol. 56, no. 1, p. 6 300 107, 2020, ISSN: 15581713. DOI: 10.1109/JQE.2019.2953296.

[105] C. Kieninger, C. Füllner, H. Zwickel, Y. Kutuvantavida, J. N. Kemal, C. Eschenbaum, D. L. Elder, L. R. Dalton, W. Freude, S. Randel, and C. Koos, "Silicon-organic hybrid (SOH) Mach-Zehnder modulators for 100 GBd PAM4 signaling with sub-1 dB phase-shifter loss," *Optics Express*, vol. 28, no. 17, pp. 24 693–24 707, 2020, ISSN: 1094-4087. DOI: 10.1364/OE.390315.

[106] P. Steglich, C. Mai, C. Villringer, B. Dietzel, S. Bondarenko, V. Ksianzou, F. Villasmunta, C. Zesch, S. Pulwer, M. Burger, J. Bauer, F. Heinrich, S. Schrader, F. Vitale, F. De Matteis, P. Prosposito, M. Casalboni, and A. Mai, "Silicon-organic hybrid photonics: Overview of recent advances, electro-optical effects and CMOS-integration concepts," *Journal of Physics: Photonics*, 2021. DOI: 10.1088/2515-7647/abd7cf.

[107] C. Wang, M. Zhang, X. Chen, M. Bertrand, A. Shams-Ansari, S. Chandrasekhar, P. Winzer, and M. Lončar, "Integrated lithium niobate electro-optic modulators operating at CMOS-compatible voltages," *Nature*, vol. 562, no. 7725, pp. 101–104, 2018. DOI: 10.1038/s41586-018-0551-y.

[108] A. Agarwal, P. Toliver, R. Menendez, S. Etemad, J. Jackel, S. Member, J. Young, T. Banwell, B. E. Little, S. T. Chu, W. Chen, W. Chen, J. Hryniewicz, F. Johnson, D. Gill, O. King, R. Davidson, K. Donovan, P. J. Delfyett, A. Agarwal, P. Toliver, R. Menendez, S. Etemad, J. Jackel, J. Young, T. Banwell, and W. Chen, "Fully Programmable Ring-Resonator-Based Integrated Photonic Circuit for Phase Coherent Applications," *Journal of Lightwave Technology*, vol. 24, no. 1, pp. 77–87, 2006. DOI: 10.1109/JLT.2005.861145.

[109] W. Bogaerts, P. De Heyn, T. V. Vaerenbergh, K. De Vos, S. K. Selvaraja, T. Claes, P. Dumon, P. Bienstman, V. Thourhout, and R. Baets, "Silicon microring resonators," *Laser Photonics Reviews*, vol. 6, no. 1, pp. 47–73, 2012. DOI: 10.1002/lpor.201100017.

[110] S. Feng, T. Lei, H. Chen, H. Cai, X. Luo, and A. Poon, "Silicon photonics: from a microresonator perspective," *Laser Photonics Reviews*, vol. 6, no. 2, pp. 145–177, 2012. DOI: 10.1002/lpor.201100020.

[111] P. Kok, W. J. Munro, K. Nemoto, T. C. Ralph, J. P. Dowling, and G. J. Milburn, "Linear optical quantum computing with photonic qubits," *Reviews of Modern Physics*, vol. 79, no. 1, pp. 135–174, 2007. DOI: 10.1103/RevModPhys.79.135.

[112] "Low-loss plasmon-assisted electro-optic modulator," *Nature*, vol. 556, pp. 483–486, 2018. DOI: 10.1038/s41586-018-0031-4.

[113] "A monolithic bipolar CMOS electronic–plasmonic high-speed transmitter," *Nature Electronics*, vol. 3, no. 6, pp. 338–345, 2020, ISSN: 25201131. DOI: 10.1038/s41928-020-0417-9.

[114] W. Heni, Y. Kutuvantavida, C. Haffner, H. Zwickel, C. Kieninger, S. Wolf, M. Lauermann, Y. Fedoryshyn, A. F. Tillack, L. E. Johnson, D. L. Elder, B. H. Robinson, W. Freude, C. Koos, J. Leuthold, and L. R. Dalton, "Silicon–Organic and Plasmonic–Organic Hybrid Photonics," *ACS Photonics*, vol. 4, no. 7, pp. 1576–1590, 2017. DOI: 10.1021/ACSPHOTONICS.7B00224.

[115] A. Josten, A. A. Kocherzhenko, B. Baeuerle, B. H. Robinson, C. Haffner, C. Hoessbacher, C. M. Isborn, D. L. Elder, J. Leuthold, L. E. Johnson, L. R. Dalton, M. Ayata, U. Koch, W. Heni, Y. Fedoryshyn, and Y. Salamin, "Optimization of Plasmonic-Organic Hybrid Electro-Optics," *Journal of Lightwave Technology, Vol. 36, Issue 21, pp. 5036-5047*, vol. 36, no. 21, pp. 5036–5047, 2018.

[116] W. Heni, C. Haffner, D. L. Elder, A. F. Tillack, Y. Fedoryshyn, R. Cottier, Y. Salamin, C. Hoessbacher, U. Koch, B. Cheng, B. Robinson, L. R. Dalton, and J. Leuthold, "Nonlinearities of organic electro-optic materials in nanoscale slots and implications for the optimum modulator design," *Optics Express*, vol. 25, no. 3, pp. 2627–2653, 2017. DOI: 10.1364/OE.25.002627.

[117] L. Alloatti, R. Palmer, S. Diebold, K. P. Pahl, B. Chen, R. Dinu, M. Fournier, J.-M. Fedeli, T. Zwick, W. Freude, C. Koos, and J. Leuthold, "100 GHz silicon–organic hybrid modulator," *Light: Science Applications*, vol. 3, e173, 2014. DOI: 10.1038/lsa.2014.54.

[118] H. Zwickel, S. Singer, C. Kieninger, Y. Kutuvantavida, N. Muradyan, T. Wahlbrink, S. Yokoyama, S. Randel, W. Freude, and C. Koos, "Verified equivalent-circuit model for slot-waveguide modulators," *Optics Express*, vol. 28, no. 9, p. 1 295 112 976, 2020. DOI: 10.1364/oe.383120.

[119] F. Merget, S. S. Azadeh, J. Mueller, B. Shen, M. P. Nezhad, J. Hauck, and J. Witzens, "Silicon photonics plasma-modulators with advanced transmission line design," *Optics Express*, vol. 21, no. 17, p. 19 593, 2013, ISSN: 1094-4087. DOI: 10.1364/oe.21.019593.

[120] J. Witzens, T. Baehr-Jones, and M. Hochberg, "Design of transmission line driven slot waveguide Mach-Zehnder interferometers and application to analog optical links," *Optics Express*, vol. 18, no. 16, p. 16 902, 2010, ISSN: 1094-4087. DOI: 10.1364/oe.18.016902.

[121] R. Ding, Y. Liu, Y. Ma, Y. Yang, Q. Li, A. Eu, J. Lim, G.-Q. Lo, K. Bergman, T. Baehr-Jones, and M. Hochberg, "High-Speed Silicon Modulator With Slow-Wave Electrodes and Fully Independent Differential Drive," *Journal of Lightwave Technology*, vol. 32, no. 12, pp. 2240–2247, 2014. DOI: 10.1109/JLT.2014.2323954.

[122] R. Ding, Y. Liu, Q. Li, Y. Yang, Y. Ma, K. Padmaraju, A. E. J. Lim, G. Q. Lo, K. Bergman, T. Baehr-Jones, and M. Hochberg, "Design and characterization of a 30-GHz bandwidth low-power silicon traveling-wave modulator," *Optics Communications*, vol. 321, pp. 124–133, 2014, ISSN: 00304018. DOI: 10.1016/j.optcom.2014.01.071.

[123] *APSUNY PDK v4.5*, 2021. [Online]. Available: https://www.aimphotonics.com/process-design-kit.

[124] S. Wehner, D. Elkouss, and R. Hanson, "Quantum internet: A vision for the road ahead," *Science*, vol. 362, no. 6412, eaam9288, 2018, ISSN: 0036-8075. DOI: 10.1126/science.aam9288.

[125] H. C. Lim, A. Yoshizawa, H. Tsuchida, and K. Kikuchi, "Wavelength-multiplexed distribution of highly entangled photon-pairs over optical fiber," *Optics Express*, vol. 16, no. 26, pp. 22 099–22 104, 2008, ISSN: 1094-4087.

[126] M. Brodsky and M. D. Feuer, *Architecture for reconfigurable quantum key distribution networks based on entangled photons directed by a wavelength selective switch*, 2009.

[127] I. Herbauts, B. Blauensteiner, A. Poppe, T. Jennewein, and H. Hübel, "Demonstration of active routing of entanglement in a multi-user network," *Optics Express*, vol. 21, no. 23, pp. 29 013–29 024, 2013, ISSN: 1094-4087. DOI: 10.1364/oe.21.029013. arXiv: 1307.5462.

[128] A. Ciurana, V. Martin, J. Martinez-Mateo, B. Schrenk, M. Peev, and A. Poppe, "Entanglement distribution in optical networks," *IEEE Journal on Selected Topics in Quantum Electronics*, vol. 21, no. 3, p. 6 400 212, 2015, ISSN: 1077260X. DOI: 10.1109/JSTQE.2014.2367241. arXiv: 1409.5965.

[129] S. Wengerowsky, S. K. Joshi, F. Steinlechner, H. Hübel, and R. Ursin, "An entanglement-based wavelength-multiplexed quantum communication network," *Nature*, vol. 564, no. 7735, pp. 225–228, 2018. DOI: 10.1038/s41586-018-0766-y.

[130] E. Y. Zhu, C. Corbari, A. Gladyshev, P. G. Kazansky, H.-K. Lo, and L. Qian, "Toward a reconfigurable quantum network enabled by a broadband entangled source," *Journal of the Optical Society of America B*, vol. 36, no. 3, B1–B6, 2019, ISSN: 0740-3224. DOI: 10.1364/josab.36.0000b1.

[131] S. K. Joshi, D. Aktas, S. Wengerowsky, M. Loncaric, S. P. Neumann, B. Liu, T. Scheidl, G. C. Lorenzo, Ž. Samec, L. Kling, A. Qiu, M. Razavi, M. Stipcevic, J. G. Rarity, and R. Ursin, "A trusted node-free eight-user metropolitan quantum communication network," *Science Advances*, vol. 6, no. 36, eaba0959, 2020, ISSN: 23752548. DOI: 10.1126/sciadv.aba0959. arXiv: 1907.08229.

[132] N. B. Lingaraju, H.-H. Lu, S. Seshadri, D. E. Leaird, A. M. Weiner, and J. M. Lukens, "Adaptive bandwidth management for entanglement distribution in quantum networks," *Optica*, vol. 8, no. 3, p. 329, 2021, ISSN: 2334-2536. DOI: 10.1364/optica.413657.

[133] N. Peters, J. Altepeter, E. Jeffrey, D. Branning, and P. Kwiat, "Precise creation, characterization, and manipulation of single optical qubits," *Quantum Inf. Comput.*, vol. 3, no. 7, pp. 503–517, 2003.

[134] R. Blume-Kohout, "Optimal, reliable estimation of quantum states," *New J. Phys.*, vol. 12, no. 4, p. 043 034, 2010.

[135] B. P. Williams and P. Lougovski, "Quantum state estimation when qubits are lost: A no-data-left-behind approach," *New J. Phys.*, vol. 19, no. 4, p. 043 003, 2017.

[136] M. Zukowski, A. Zeilinger, M. A. Horne, and A. K. Ekert, ""Event-ready-detectors" Bell experiment via entanglement swapping," *Physical Review Letters*, vol. 71, no. 26, pp. 4287–4290, 1993, ISSN: 00319007. DOI: 10.1103/PhysRevLett.71.4287.

[137] C. H. Bennett, G. Brassard, S. Popescu, B. Schumacher, J. A. Smolin, and W. K. Wootters, "Purification of noisy entanglement and faithful teleportation via noisy channels," *Physical Review Letters*, vol. 76, no. 5, pp. 722–725, 1996, ISSN: 10797114. DOI: 10.1103/PhysRevLett.76.722.

[138] L. M. Duan, M. D. Lukin, J. I. Cirac, and P. Zoller, "Long-distance quantum communication with atomic ensembles and linear optics," *Nature*, vol. 414, no. 6862, pp. 413–418, 2001, ISSN: 00280836. DOI: 10.1038/35106500.

[139] L. Jiang, J. M. Taylor, K. Nemoto, W. J. Munro, R. Van Meter, and M. D. Lukin, "Quantum repeater with encoding," *Physical Review A*, vol. 79, no. 3, p. 032 325, 2009, ISSN: 1050-2947. DOI: 10.1103/physreva.79.032325.

[140] S. Muralidharan, J. Kim, N. Lütkenhaus, M. D. Lukin, and L. Jiang, "Ultrafast and fault-tolerant quantum communication across long distances," *Physical Review Letters*, vol. 112, no. 25, p. 250 501, 2014, ISSN: 10797114. DOI: 10.1103/PhysRevLett.112.250501.

[141] J. W. Pan, D. Bouwmeester, H. Weinfurter, and A. Zeilinger, "Experimental entanglement swapping: Entangling photons that never interacted," *Physical Review Letters*, vol. 80, no. 18, pp. 3891–3894, 1998, ISSN: 10797114. DOI: 10.1103/PhysRevLett.80.3891.

[142] J. Calsamiglia and N. Lütkenhaus, "Maximum efficiency of a linear-optical bell-state analyzer," *Applied Physics B*, vol. 72, no. 1, pp. 67–71, 2001. DOI: 10.1007/s003400000484.

[143] M. Michler, K. Mattle, H. Weinfurter, and A. Zeilinger, "Interferometric Bell-state analysis," *Phys. Rev. A*, vol. 53, no. 3, R1209–R1212, 1996, ISSN: 10941622. DOI: 10.1103/PhysRevA.53.R1209.

[144] K. Mattle, H. Weinfurter, P. G. Kwiat, and A. Zeilinger, "Dense coding in experimental quantum communication," *Physical Review Letters*, vol. 76, pp. 4656–4659, 1996, ISSN: 10797114. DOI: 10.1103/PhysRevLett.76.4656.

[145] G. Vittorini, D. Hucul, I. V. Inlek, C. Crocker, and C. Monroe, "Entanglement of distinguishable quantum memories," *Physical Review A - Atomic, Molecular, and Optical Physics*, vol. 90, no. 4, 040302(R), 2014, ISSN: 10941622. DOI: 10.1103/PhysRevA.90.040302.

[146] A. M. Dyckovsky and S. Olmschenk, "Analysis of photon-mediated entanglement between distinguishable matter qubits," *Physical Review A - Atomic, Molecular, and Optical Physics*, vol. 85, no. 5, p. 052 322, 2012, ISSN: 10502947. DOI: 10.1103/PhysRevA.85.052322.

[147] "Entangling different-color photons via time-resolved measurement and active feed forward," *Physical Review Letters*, vol. 112, no. 10, p. 103 602, 2014, ISSN: 10797114. DOI: 10.1103/PhysRevLett.112.103602.

[148] H.-H. Lu, N. Klco, J. M. Lukens, T. D. Morris, A. Bansal, A. Ekström, G. Hagen, T. Papenbrock, A. M. Weiner, M. J. Savage, and P. Lougovski, "Simulations of subatomic many-body physics on a quantum frequency processor," *Phys. Rev. A*, vol. 100, no. 1, p. 012 320, 2019.

[149] S.-Y. Lan, S. D. Jenkins, T. Chanelière, D. N. Matsukevich, C. J. Campbell, R. Zhao, T. A. B. Kennedy, and A. Kuzmich, "Dual-species matter qubit entangled with light," *Phys. Rev. Lett.*, vol. 98, p. 123 602, 12 2007. DOI: 10.1103/PhysRevLett.98.123602.

[150] S. Seshadri, P. Imany, N. Lingaraju, D. E. Leaird, and A. M. Weiner, "Harnessing spectral phase in broadband time-energy entangled photons for precision delay sensing," in *Frontiers in Optics / Laser Science*, Optical Society of America, 2020, FW7C.1. DOI: 10.1364/FIO.2020.FW7C.1.

VITA

Navin B. Lingaraju graduated with a B.S. in electrical engineering from Case Western Reserve University in 2003. Following a career in intellectual property law, which spanned both the public and private sectors, he returned to a career in science as a graduate student researcher at the National Institute of Standards and Technology in 2015. He subsequently graduated from the University of Maryland in 2017 with a M.S. in electrical engineering. He is currently pursuing a Ph.D. in electrical engineering at Purdue University, where he conducts research a member of the Ultrafast Optics and Optical Fiber Communications Laboratory. His work is focused on leveraging classical lightwave communications and advanced nanofabrication to develop photonic systems for quantum communication and networking. His work has resulted in four journal publications, a contribution to a collaborative roadmap for quantum photonics, and numerous conference presentations, including a post-deadline presentation at IPC 2020 and an invited talk at Next Generation Quantum Networking 2021. During his time at Purdue he has been supported by a Frederick N. Andrews Fellowship, as well as by a Quantum Information Science and Engineering Network (QISE-NET) Triplet award. Lingaraju is member of the Optical Society (OSA), the Institute of Electrical and Electronics Engineers (IEEE) Photonics Society, and an active reviewer for IEEE.

PUBLICATIONS

* - *corresponding author*

† - *authors contributed equally*

Preprints and Manuscripts (not refereed)

[1] Navin B. Lingaraju,†* Hsuan-Hao Lu,† Daniel E. Leaird, Steven Estrella, Jospeh M. Lukens, and Andrew M. Weiner, *Bell state analyzer for spectrally distinguishable photons*, Manuscript under review.

Journal version of [8]

[2] Muneer Alshowkan, Brian Williams, Philip Evans, Nageswara Rao, Emma Simmerman, Navin B. Lingaraju, Hsuan-Hao, Andrew Weiner, Nicholas Peters, Joseph Lukens, *Adaptive Bandwidth Management for Entanglement Distribution in a Fully-connected Fiber-optic Network*, arXiv:2102.13596 [quant-ph], 2021.

Journal version of [11]

[3] Galan Moody,* Volker J. Sorger,* Paul W. Juodawlkis, William Loh, Cheryl Sorace-Agaskar, Marcelo Davanco, Lin Chang, John E. Bowers, Niels Quack, Christophe Galland, Igor Aharonovich, M. A. Wolff, C Schuck, Neil Sinclair, Marko Lončar, Tin Komljenovic, David Weld, Shayan Mookherjea, Sonia Buckley, Marina Radulaski, Stephan Reitzenstein, Benjamin Pingault, Bartholomeus Machielse, Debsuvra Mukhopadhyay, Alexey Akimov, Aleksei Zheltikov, Girish S. Agarwal, Kartik Srinivasan, Juanjuan Lu, Hong X. Tang, Wentao Jiang, Timothy P. McKenna, Amir H. Safavi-Naeini, Stephan Steinhauer, Ali W. Elshaari, Val Zwiller, Paul S. Davids, Nicholas Martinez, Michael Gehl, John Chiaverini, Karan K. Mehta, Jacquiline Romero, Navin B. Lingaraju, Andrew M. Weiner, Daniel Peace, Robert Cernansky, Mirko Lobino, Eleni Diamanti, Luis Trigo Vidarte, Ryan M Camacho, *Roadmap on Integrated Quantum Photonics*, arXiv:2102.03323 [quant-ph], 2021.

Journals (refereed)

[4] Navin B. Lingaraju,* Hsuan-Hao Lu, Daniel E. Leaird, Andrew M. Weiner, and Jospeh M. Lukens, *Adaptive bandwidth management for entanglement distribution in quantum networks*, Optica 8 (3), 329-332, 2021.

Journal version of [13]

[5] Poolad Imany,* Navin B. Lingaraju, Mohammed S. Alshaykh, Daniel E. Leaird, and Andrew M. Weiner, *Probing quantum walks through coherent control of high-dimensionally entangled photons*, Sci. Adv. eaba8066, 2020.

Journal version of [15]

[6] Navin B. Lingaraju,* Hsuan-Hao Lu, Suparna Seshadri, Poolad Imany, Daniel E. Leaird, Joseph M. Lukens, and Andrew M. Weiner, *Quantum frequency combs and Hong–Ou–Mandel interferometry: the role of spectral phase coherence*, Opt. Express 27, 38683-38697, 2019.

Journal version of [18]

[7] Oscar E. Sandoval,† Navin B. Lingaraju,†* Poolad Imany, Daniel E. Leaird, Michael Brodsky, and Andrew M. Weiner, *Polarization diversity phase modulator for measuring frequency-bin entanglement of a biphoton frequency comb in a depolarized channel*, Opt. Lett. 44, 1674-1677, 2019.

Journal version of [20]

Conference proceedings (refereed)

[8] Navin B. Lingaraju,†* Hsuan-Hao Lu,† Daniel E. Leaird, Steven Estrella, Jospeh M. Lukens, and Andrew M. Weiner, *A programmable electro-optic Bell-state analyzer for spectrally distinguishable photons*, in Conference on Lasers and Electro-Optics, OSA Technical Digest, paper FTu1N.5, 2021.

[9] Hsuan-Hao Lu,* Navin B. Lingaraju, Daniel E. Leaird, Andrew M. Weiner, and Jospeh M. Lukens, *Scaling the discrete Fourier transform gate in the quantum frequency processor*, in Conference on Lasers and Electro-Optics, OSA Technical Digest, paper FTu1N.8, 2021.

[10] Suparna Seshadri,* Hsuan-Hao Lu, Navin B. Lingaraju, Poolad Imany, Daniel E. Leaird, and Andrew M. Weiner, *Nonlocal sensing of temporal delay in dispersive links using time-energy entangled photons*, in Conference on Lasers and Electro-Optics, OSA Technical Digest, paper FTh2O.2, 2021.

[11] Muneer Alshowkan, Brian Williams, Philip Evans, Nageswara Rao, Emma Simmerman, Navin B. Lingaraju, Hsuan-Hao, Andrew Weiner, Nicholas Peters, Joseph Lukens, *Adaptive Bandwidth Management for Entanglement Distribution in a Fully-connected Fiber-optic Network*, in Conference on Lasers and Electro-Optics, OSA Technical Digest, paper FF2J.4, 2021.

[12] Navin B. Lingaraju,†* Hsuan-Hao Lu,† Daniel E. Leaird, Steven Estrella, Jospeh M. Lukens, and Andrew M. Weiner, *A Bell-state analyzer for photonic frequency*, 2020 IEEE Photonics Conference (IPC), **Post-Deadline Session**, paper PD5.

[13] Navin B. Lingaraju,* Hsuan-Hao Lu, Suparna Seshadri, Daniel E. Leaird, Andrew M. Weiner, and Jospeh M. Lukens, *Adaptive Bandwidth Management for Entanglement Distribution in a Fully-connected Fiber-optic Network*, in Conference on Lasers and Electro-Optics, OSA Technical Digest, paper FTh1D.2, 2020.

[14] Navin B. Lingaraju,* Nathan O'Malley, Daniel E. Jones, Oscar E. Sandoval, Hana N. Azzouz, Daniel E. Leaird, Joseph M. Lukens, Michael Brodsky, and Andrew M. Weiner, *Polarization diversity phase modulator for frequency-bin operations with hyperentangled biphoton frequency combs*, in Conference on Lasers and Electro-Optics, OSA Technical Digest, paper FF1D.5, 2020.

[15] Poolad Imany,* Navin B. Lingaraju, Mohammed S. Alshaykh, Daniel E. Leaird, and Andrew M. Weiner, *Quantum many-body simulations through quantum walks of high-dimensionally entangled photons*, in Conference on Lasers and Electro-Optics, OSA Technical Digest, paper JM3G.5, 2020.

[16] Suparna Seshadri,* Poolad Imany, Navin B. Lingaraju, Daniel E. Leaird, and Andrew M. Weiner, *Precision measurement of optical fiber delays with a quantum frequency comb*, in Conference on Lasers and Electro-Optics, OSA Technical Digest, paper FM1C.5, 2020.

[17] Navin B. Lingaraju,* Oscar E. Sandoval, Daniel E. Leaird, Michael Brodsky, and Andrew M. Weiner, *Effect of Pump Bandwidth on Measurements of Frequency-Bin Entanglement*, 2019 IEEE Photonics Conference (IPC), San Antonio, TX, USA, 2019, pp. 1-2, doi: 10.1109/IPCon.2019.8908341.

[18] Navin B. Lingaraju,* Hsuan-Hao Lu, Suparna Seshadri, Poolad Imany, Daniel E. Leaird, Jospeh M. Lukens, and Andrew M. Weiner, *Spectral phase coherence in HOM interferometry*, in Conference on Lasers and Electro-Optics, OSA Technical Digest, paper JTu3A.5, 2019.

[19] Oscar E. Sandoval,† Navin B. Lingaraju,†* Poolad Imany, Daniel E. Leaird, Michael Brodsky, and Andrew M. Weiner, *Measuring frequency-bin entanglement in depolarized biphoton frequency combs*, in Conference on Lasers and Electro-Optics, OSA Technical Digest, paper FTh1A.2, 2019.

[20] Oscar E. Sandoval,†* Navin B. Lingaraju,† Poolad Imany, Daniel E. Leaird, Michael Brodsky, and Andrew M. Weiner, *Polarization diversity phase modulator for measuring frequency-bin entanglement of biphoton frequency combs in a depolarized channel*, in Frontiers in Optics / Laser Science, OSA Technical Digest, paper JTu3A.69, 2018.